Generalization of GNSS-A seafloor precise positioning and geodetic applications to the subduction seismic processes

（GNSS-A 海底精密測位の一般化と沈み込み帯における
地震プロセスへの測地学的応用）

A dissertation submitted to

Graduate School of Environmental Studies, Nagoya University

for the degree of

Doctor of Philosophy in Science

（名古屋大学大学院環境学研究科学位論文　博士（理学））

Shun-ichi Watanabe

（渡邉 俊一）

2021

Abstract

In the last several decades of the last century, technologies for space geodesy based on electromagnetic waves have been substantially developed. This enabled the absolute positioning with more than centimeter precision on the Earth. Under the seawater, where the electromagnetic waves cannot propagate, geodesy with acoustic waves was proposed. The idea of Global Navigation Satellite System – Acoustic ranging combination (GNSS-A) was first implemented by the scientists in the Scripps Institution of Oceanography (SIO) in the United States, and followed by Japan.

Since 2000, the Japan Coast Guard (JCG) has been constructing the GNSS-A observation array to cover the large parts of the source regions of megathrust earthquakes around Japanese archipelago, which is now the largest GNSS-A observation array in the world. Simultaneously with the maintenance and expansion of the array, the GNSS-A technique has been improved in the both sides of hardware and software. The efforts for sustainable GNSS-A observation resulted in the detection of seafloor crustal deformation due to the plate subduction with a precision of centimeters.

Along with the regular GNSS-A observations, multiple research groups have continuously improved the analysis techniques, though almost independently. That is because each group have applied different observation configuration and has developed analytical procedures independently; for example, the GNSS-A configuration designed in JCG is different from the original SIO's configuration. Especially since the latter half of 2010s, discussions and implementations for the modeling of inclined sound speed structure have been made by several different GNSS-A observation groups. In spite of the discrepancy in observation configurations, the previous studies showed that the implementation of such sound speed structure model is surely able to improve the GNSS-A accuracy.

In this study, the author derived more generalized GNSS-A observation equation by introducing the sound speed perturbation field model, where the perturbation term was expressed as a function of time and positions of surface and seafloor units. Using this formulation, the previously proposed simpler sound speed structure model with a layer of one-dimensionally inclined sound speed can be fully expressed, with avoiding the singularity in the Jacobian matrix. Based on the proposed observation model, estimation procedure is formulated based on the empirical Bayes approach to take the assumption of gentle change of

sound speed field. By considering the correlation terms of neighboring observation data, this succeeded in deriving the precise seafloor positions along with likely sound speed field.

The author implemented the proposed analytical procedure into a Python code from scratch, because the existing JCG's analysis software gradually had difficulty in efficiency, extensibility and readability due to the various ad hoc retrofit codes added by many staffs. The newly developed software named "GARPOS" was distributed publicly as an open source software along with its orderly formatted GNSS-A data.

For the application to the geophysical research, the author analyzed the JCG's GNSS-A dataset. With the conventional method, the author verified the tectonic block model in the Philippine Sea plate and estimated the coupling ratio on the block boundary fault. Furthermore, with the estimated slip deficit rate from the seafloor geodesy along the Nankai Trough, tsunami excitation and propagation were simulated under the conditions for the different plate boundary geometry. This showed that the fault geometry significantly contributes to the tsunami height distribution on the coast, even for the same input of seafloor geodetic data.

Applying GARPOS to the GNSS-A data along the Japan Trench for 10 years after the 2011 Tohoku-oki earthquake, temporal evolution and spatial characteristics of postseismic crustal deformation was captured. For the first several years, the seafloor above the main rupture had moved toward the land with a higher rate than the plate subduction. The rapid landward motion revealed the dominance in the postseismic processes of viscoelastic relaxation beneath the subducting Pacific plate. A decade of GNSS-A observations in the northern and southern sides of the main rupture also provided the evidence for the occurrence of the afterslip beneath the seafloor, which had almost decayed in the first 2–3 years. The differences in the decay times of seafloor movements obtained at the off-Fukushima site for the horizontal and vertical components suggested that the shallower portion of the interplate fault had been ruptured in the coseismic phase. Although this feature was not resolved by the coseismic GNSS-A data, it is consistent with the tsunami wave data.

The open source software GARPOS and its organized I/O formats provide a practical example for the GNSS-A standardization. Based on the proposed configuration, the author expects to have world-wide discussions on the GNSS-A community. This will certainly be a key for the cooperation among the institutes, such as for the urgent GNSS-A operation in the cases of earthquakes, for the technology transfer to other subduction zones, and for the "global" geodesy on the remaining 70% of the Earth.

Table of Contents


GARPOS
Positioning for 70% of our planet

Chapter 1

Introduction

Precise measurements of seafloor position in the global reference frame opens the door to the "global" geodesy in the true sense of the word. It extended the global geodetic network into the ocean and has revealed the tectonic processes in the subduction zone including the pre-, co-, and post-seismic crustal deformation for megathrust earthquakes (e.g., Bürgmann and Chadwell, 2014; Fujimoto, 2014; Watanabe, 2021, for review). Many findings have been reported especially in the northwestern Pacific along the Nankai Trough (e.g., Yokota et al., 2016; Yasuda et al., 2017; Yokota and Ishikawa, 2020), and the Japan Trench (e.g., Sato et al., 2011; Kido et al., 2011; Watanabe et al., 2014; Tomita et al., 2015; Tomita et al., 2017). These achievements owe to the development of GNSS-A (Global Navigation Satellite System – Acoustic ranging combined) seafloor positioning technique, proposed by Spiess (1980).

GNSS-A generally consists of two subcomponents, i.e., global positioning of the surface platform and local positioning between the surface and seafloor instruments. The global positioning of the surface platform is measured using the GNSS (Global Navigation Satellite System). The local positioning in the water is determined by the trilateration using the acoustic ranging technique. To cancel the doppler effect due to the advection, round-trip travel time should be measured. Therefore, a set of surface transducer and seafloor transponder is used in the GNSS-A observation.

Observers can take various ways to design the underwater trilateration. When the multiple (at least three) acoustic transponders are installed on the seafloor as benchmarks and the distances are measured in advance, the relative position of the surface instrument with respect to the seafloor benchmarks can be determined. For the round-trip acoustic ranging, the major error source is sound speed variation in the water. Because the most of sound speed variation is concentrated in the shallowest part (e.g., Watanabe and Uchida, 2016), it influences almost equally to each acoustic ray from the single surface transducer. Therefore, when the surface transducer is placed above the centroid of seafloor transponder array, horizontal position of

array can be determined almost independently of sound speed variation. With this "stationary" GNSS-A configuration, Spiess et al. (1998) succeeded in deriving horizontal motion of the Juan de Fuca plate. Under the assumption that the sound speed structure is horizontally stratified, Osada et al. (2003) estimated the temporal variation of sound speed from the acoustic data by comparing the residuals of acoustic travel time from multiple transponders. Kido et al. (2008) modified the expression to validate the stationary configuration for a loosely tied buoy even in the case where the sound speed has spatial variations. The stationary GNSS-A configuration is applied mainly by the groups in the Scripps Institution of Oceanography (e.g., Gagnon et al., 2005; Chadwell and Spiess, 2008) and in the Tohoku University (e.g., Fujimoto, 2014; Tomita et al., 2015; Tomita et al., 2017).

To determine the 3-dimensional position of single transponder, acoustic ranging from the broader area on the surface should be conducted. This "move-around" GNSS-A approach is taken by Obana et al. (2000) and Asada and Yabuki (2001) (Figure 1-1). The move-around GNSS-A configuration is developed and practicalized mainly by the collaborative group of the Japan Coast Guard and the University of Tokyo (e.g., Fujita, 2006; Sato and Fujita, 2012; Watanabe, 2021, for review), and the Nagoya University. Unlike the stationary configuration, the horizontal positions of transponders are vulnerable to bias errors of sound speed field. Fujita et al. (2006) and Ikuta et al. (2008) then developed the methods estimating both the positions and the temporal variations of sound speed.

Similar to the idea of dilution of precision (DOP) in the GNSS positioning, well-distributed acoustic data is expected to decrease the bias errors of the estimated transponders' positions. By implementing the sailing observations where the sea-surface unit sails over the transponder array to collect geometrically symmetric data, positioning accuracy and observation efficiency have improved (Sato et al., 2013b; Ishikawa et al., 2020).

To enhance the stability of positioning, an assumption that the geometry of transponder array is constant over whole observation period is usually adopted (e.g., Matsumoto et al., 2008; Watanabe et al., 2014; Chen et al., 2018; Yokota et al., 2018). Misestimates of sound speed cause the positional biases parallel to the averaged acoustic-ray direction, which results in the distortion of the estimated array geometry. Constraining the array geometry contributes to reducing the bias error in the sound speed estimates and the transponders' centroid position.

For the purpose of improving the positioning accuracy in the move-around configuration, the technique to estimate the sound speed variation is required. In the earlier stage of the

move-around GNSS-A development, only the temporal variation of sound speed was estimated (e.g., Fujita et al., 2006; Ikuta et al., 2008). The spatial variations of sound speed were projected to the temporal variations, because most of the sound speed change are confined in the shallowest portion along the acoustic ray paths (e.g., Watanabe and Uchida, 2016). Therefore, the spatial gradient of the sound speed in the shallow layer can be extracted from the estimated temporal sound speed variation (e.g., Yokota et al., 2019). Meanwhile, because the sound speed also varies with the acoustic ray paths, the transponder-dependent variation should be also resolved. Under the assumption of one-directional sound speed gradient, Yokota et al. (2019) extracted the transponder-dependent correction term from the residuals of the results derived by the conventional method of Fujita et al. (2006).

Based on the analytical scheme provided by Ikuta et al. (2008), Yasuda et al. (2017) took a different approach where the sound speed structure shallower than 1000 m is assumed to be inclined in one direction due to the Kuroshio current flowing near their sites in the offshore region south of Kii Peninsula, Japan. Because their model reflects the specific oceanographic feature, the estimated parameters are easier to be interpreted than that of Yokota et al. (2019) which has higher degree of freedom to extract the oceanographic features.

On the other hand, Honsho et al. (2019) showed a more general expression for one-directional sound speed gradient. As they mentioned, the gradient terms in their formulation correspond to the extracted features in Yokota et al. (2019). Honsho et al. (2019) applied the method to the data obtained with the combination of move-around and stationary configurations (Honsho and Kido, 2017). The work by Honsho et al. (2019) showed the possibility to connect all the GNSS-A configurations into a unified GNSS-A solver. However, due to the limitation in resolving the general gradient structure, an additional constraint was taken for the practical application, which is essentially the same formulation as Yasuda et al. (2017).

In this study, we reconstruct the GNSS-A observation equation, in which the generalized sound speed perturbation model is applied. The proposed model approximately includes the previous models prepared for the move-around configuration. Introducing more realistic sound speed structure improves the GNSS-A positioning accuracy.

As Part I of this thesis, the author demonstrates the reconstructed GNSS-A methodology. In Chapter 2, the derivation of the generalized GNSS-A observation equation, which includes the practical solutions in the previous studies by Yokota et al. (2019), Yasuda et al. (2017), and Honsho et al. (2019) as special cases, and the analytical technique to estimate the gradient

sound speed structure are demonstrated. For the application, the effects of sound speed variation should be modeled in a simplified form. To handle the ill-posed problem, the empirical Bayes approach was applied to the analytical procedure. The author then derives the concrete expression in terms of the Bayesian posterior probability. In Chapter 3, the applicability of Precise Point Positioning (PPP) for the routine analysis is discussed using the actual GNSS-A data. In Chapter 4, the author illustrates the newly developed open source GNSS-A analysis software "GARPOS", where the standardized GNSS-A data format is used as an input. The application to the actual data and evaluation of the new method are also demonstrated.

Part II introduces the outcomes of GNSS-A observations contributing to the seismology and geodesy. Chapter 5 provides the results of geodetic measurement on the subducting Philippine Sea plate along the Sagami Trough. The results support that the northernmost part of the Philippine Sea plate should be interpreted in the tectonic block model. In Chapter 6, the interseismic GNSS-A data along the Nankai Trough, where the postseismic effects of the 2004 Kii-oki earthquakes are also considered, are used for some case studies of tsunami propagation scenarios. The results suggested that the uncertainty of plate interface would cause significant errors in the tsunami generation. Chapter 7 discusses the postseismic seafloor deformation following the 2011 Tohoku-oki earthquake occurred along the Japan Trench, where the seafloor GNSS-A data contributed to provide the first direct evidence for the dominance of viscoelastic relaxation around the main rupture. The spatiotemporal variation of decadal deformation data also indicated a widely spread tsunamigenic rupture followed by a downdip afterslip. These Chapters in Part II show that the geodetic applications of GNSS-A have substantially improved our understandings of seismic cycle in the subduction zone.

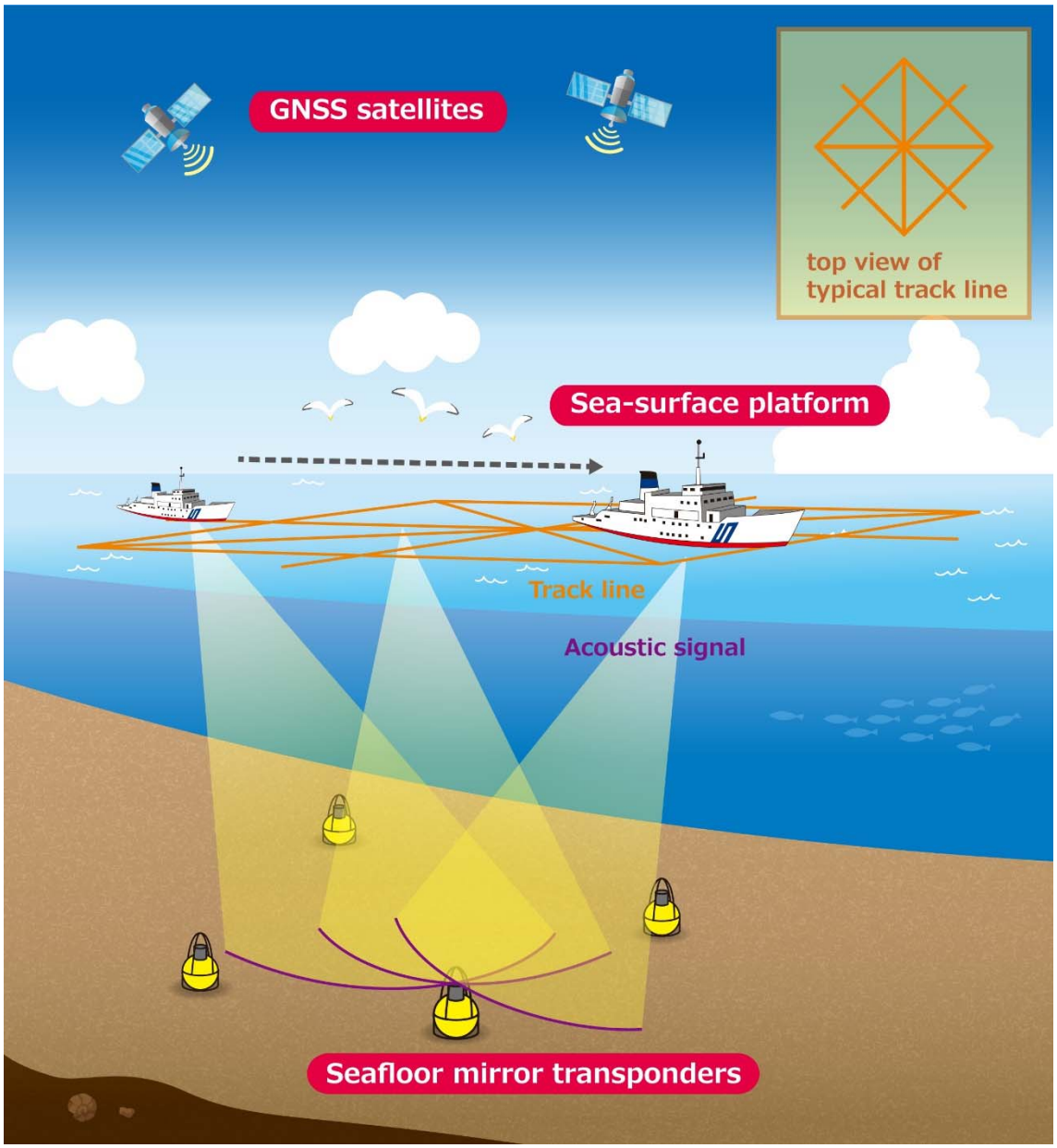

Figure 1-1. Schematic diagram of the GNSS-A system in a move-around configuration (after Watanabe et al., 2020c).

PART I

Reconstruction of GNSS-A methodology

Chapter 2

Construction of GNSS-A analysis procedure based on the empirical Bayes approach

---

This Chapter references the author's work published as Watanabe et al. (2020c).

Reference:

Watanabe, S., Ishikawa, T., Yokota, Y., and Nakamura, Y. (2020c) GARPOS: Analysis Software for the GNSS - A seafloor positioning with simultaneous estimation of sound speed structure. *Front. Earth Sci.*, **8**, 597532. doi:10.3389/feart.2020.597532

2.1 Background

Because the GNSS-A techniques were independently developed in several institutions, the methodologies and configurations are not systematically organized, though the original concept (Spiess, 1980) is the same. The GNSS-A for the precise seafloor positioning should meet the following requirements: (1) the track of sea-surface platform should be determined by dual-frequency GNSS to achieve the precision of centimeters to decimeter, (2) the round-trip acoustic travel times should be measured in a precision of less than sub-milliseconds, which is equivalent to a range of several decimeters, (3) the sound speed variations should be estimated and corrected under appropriate assumptions, rather than directly using the observed profiles. The largest difference in GNSS configurations lies in how to correct or minimize the effects of the sound speed variation in the seawater.

In this Chapter, we summarize the general expression for GNSS-A observation with explicitly expanding the effects of sound speed perturbation. We also demonstrate one of the

estimation procedures using the empirical Bayes approach. Section 2.1 illustrates the GNSS-A system configuration. In Section 2.2, generalized observation model is derived. One of the solutions of GNSS-A observation equations is introduced in Section 2.3.

2.2 GNSS-A system subcomponents

The GNSS-A observation consists of the global positioning of sea-surface transducer and the underwater acoustic ranging. This section shows each subcomponent for the construction of the GNSS-A observation equation.

2.2.1 Positioning of sea-surface transducer

One key subcomponent of the GNSS-A is the global positioning of sea-surface transducer, which is realized by GNSS observation. Whereas acoustic measurement determines the relative positions of the seafloor transponders and the sea-surface transducer, GNSS plays a role to align them to the earth-centered, earth-fixed (ECEF) coordinates such as the International Terrestrial Reference Frame (ITRF). The global position of the transducer, $\boldsymbol{P}(t)$, should be determined in the GNSS's reference frame, a realization of the ITRF.

It should be noted that the seafloor transponders' positions are generally a function of time, including the solid earth tide as well as global and local crustal deformation (e.g., IERS Conventions, 2010). For the purpose of detecting tectonic crustal deformation, it is better to determine the seafloor positions in the solid-earth-tide-free coordinates. Because the observation area is limited to several-kilometers-width, solid-earth-tide-free solutions can be obtained when the trajectory of the transducer is determined in the solid-earth-tide-free coordinates. Hereafter, the positions are expressed in solid-earth-tide-free coordinates in this thesis.

To determine $\boldsymbol{P}(t)$ in the ECEF coordinates, a set of GNSS antenna/receiver and a gyro sensor should be mounted on the sea-surface unit. The positions of GNSS antenna, $\boldsymbol{Q}(t)$, can be determined using any of appropriate kinematic GNSS solvers (see Chapter 3 for the GNSS solver). The gyro sensor provides the attitude of the sea-surface platform, $\boldsymbol{\Theta}(t) = [\theta_r \quad \theta_p \quad \theta_h]^T$, i.e., roll, pitch, and heading (Figure 2-1). Because the attitude values are aligned to the local ENU coordinates, it is convenient to transform $\boldsymbol{Q}(t)$ from ECEF to local ENU coordinates, i.e., $\boldsymbol{Q}(t) = [Q_e \quad Q_n \quad Q_u]^T$. Using the relative position of the transducer to the GNSS antenna in the gyro's rectangular coordinate (called "ATD offset" hereafter; Figure 2-1), $\boldsymbol{M} = [M_r \quad M_p \quad M_h]^T$, we obtain the transducer's position in the local ENU coordinates as,

$$\boldsymbol{P}(t) = \boldsymbol{Q}(t) + R\big(\boldsymbol{\Theta}(t)\big)\boldsymbol{M}, \tag{2.1}$$

with,

$$R(\boldsymbol{\Theta}) = \begin{bmatrix} 0 & 1 & 0 \\ 1 & 0 & 0 \\ 0 & 0 & -1 \end{bmatrix} \begin{bmatrix} \cos\theta_h & -\sin\theta_h & 0 \\ \sin\theta_h & \cos\theta_h & 0 \\ 0 & 0 & 1 \end{bmatrix} \begin{bmatrix} \cos\theta_p & 0 & \sin\theta_p \\ 0 & 1 & 0 \\ -\sin\theta_p & 0 & \cos\theta_p \end{bmatrix} \begin{bmatrix} 1 & 0 & 0 \\ 0 & \cos\theta_r & -\sin\theta_r \\ 0 & \sin\theta_r & \cos\theta_r \end{bmatrix}.$$

The ATD offset values should be measured before the GNSS-A observation.

2.2.2 Underwater acoustic ranging

Another key subcomponent is the technique to measure the acoustic travel time between the sea-surface transducer and the seafloor transponders. The techniques for the precise ranging using acoustic mirror-type transponders had been developed and practicalized in early studies (e.g., Spiess, 1980; Nagaya, 1995). Measuring round-trip travel time reduces the effect of advection of the media between the instruments.

The round-trip travel time for the ith acoustic signal to the jth transponder, T_i, is calculated as a function of the relative position of the transponder to the transducer and the 4-dimensional sound speed field, $V(e,n,u,t)$, i.e.,

$$T_i = T_i^c\left(\boldsymbol{P}(t_{i_+}), \boldsymbol{P}(t_{i_-}), \boldsymbol{X}_j, V(e,n,u,t)\right), \tag{2.2}$$

where t_{i_+}, t_{i_-}, and $\boldsymbol{X}_j$ are the transmitted and received time for the ith acoustic signal, and the position of seafloor transponder numbered j, respectively. Note that j is a function of i.

Although the concrete expression is provided as the eikonal equation (e.g., Jensen et al., 2011; Sakic et al., 2018), it requires much computational resources to numerically solve. When the sound speed structure is assumed to be horizontally stratified, we can apply a heuristic approach based on the Snell's law (e.g., Hovem, 2013), which has an advantage in computation time (e.g., Chadwell and Sweeney, 2010; Sakic et al., 2018).

Therefore, we decomposed the 4-dimensional sound speed field into a horizontally stratified stational sound speed profile and a perturbation to obtain the following travel time expression:

$$T_i^c\left(\boldsymbol{P}(t_{i_+}), \boldsymbol{P}(t_{i_-}), \boldsymbol{X}_j, V(e,n,u,t)\right) = \exp(-\gamma_i) \cdot \tau_i\left(\boldsymbol{P}(t_{i_+}), \boldsymbol{P}(t_{i_-}), \boldsymbol{X}_j, V_0(u)\right), \tag{2.3}$$

where τ_i and $V_0(u)$ denote the reference travel time and the reference sound speed profile, respectively. $V_0(u)$ is given as a piecewise linear function of height, so that the propagation length along the radial component and the propagation time can be calculated for the given incidence angle according to the Snell's law (e.g., Hovem, 2013; Sakic et al. 2018). The expression of the correction coefficient, $\exp(-\gamma_i)$, is selected for the simplification in the following expansion. It represents the discrepancy ratio of the actual travel time to the reference, which caused by the spatial and temporal perturbations of the sound speed field.

In the right-hand side of eq. (2.3), γ_i and $\boldsymbol{X}_j$ are assigned as the estimator. Eq. (2.1) gives the transducer's position $\boldsymbol{P}(t)$ as a function of the GNSS antenna's position $\boldsymbol{Q}(t)$, the attitude vector $\boldsymbol{\Theta}(t)$, and the ATD offset $\boldsymbol{M}$. The time-independent parameter $\boldsymbol{M}$ can be also assigned as the estimator when the variation of the attitude value is large enough to resolve the parameter. Hence, the reference travel time can be rewritten as $\tau_i = \tau_i\left(\boldsymbol{X}_j, \boldsymbol{M} \middle| \boldsymbol{Q}(t), \boldsymbol{\Theta}(t), V_0(u)\right)$, where the variables on the left and right sides of the vertical bar indicate the estimators and the observables, respectively.

2.3 GNSS-A model

By comparing the observed and modeled travel times, the observation equation can be derived. This section demonstrates how to expand the eq. (2.3) into a parametric model. The inclusivity of proposed GNSS-A model to the previous models are also discussed.

2.3.1 Sound speed perturbation model

In seawater, sound speed is empirically determined as a function of temperature, salinity, and pressure (e.g., Del Grosso, 1974). Because these variables strongly depend on the water depth, the vertical variation of the sound speed is much larger than the horizontal variation in the observation scale. Thus, $|\gamma_i| \ll 1$ will be satisfied in most cases where the reference sound speed appropriately represents the sound speed field. In such cases, the average sound speed along the actual ray path is expressed as $\overline{V_0} + \delta V_i \sim \overline{V_0} + \gamma_i \overline{V_0}$, where $\overline{V_0}$ denotes the average sound speed of the reference profile.

Recalling that the sound speed field is continuous and usually smooth in time and space within the observation scale, we can introduce a scalar field which is continuous with time and acoustic instruments' positions, i.e., $\Gamma(t, \boldsymbol{P}, \boldsymbol{X})$, from which the correction coefficient is extracted. Because the temporal variation of the sound speed structure is small during the travel of the acoustic signal and is usually concentrated in the shallower portion of the sea, γ_i

is approximated by the average of the transmission and the reception times, i.e., $\gamma_i \equiv \frac{1}{2}\sum_{l=i_+,i_-} \Gamma\left(t_l, \boldsymbol{P}(t_l), \boldsymbol{X}_j\right)$. The function $\Gamma(t, \boldsymbol{P}, \boldsymbol{X})$ can be called the sound speed perturbation model.

For simplification, we put the sound speed perturbation model as time-varying linear spatial function in space as follows:

$$\Gamma(t, \boldsymbol{P}, \boldsymbol{X}) \equiv \alpha_0(t) + \boldsymbol{\alpha}_1(t) \cdot \frac{\boldsymbol{P}}{L^*} + \boldsymbol{\alpha}_2(t) \cdot \frac{\boldsymbol{X}}{L^*}, \tag{2.4}$$

where L^* indicates the characteristic length of the observation site (typically in several kilometers). $\alpha_0(t)$, $\boldsymbol{\alpha}_1(t)$ and $\boldsymbol{\alpha}_2(t)$ are the time-dependent coefficients for each term. Because the vertical variation of $\boldsymbol{P}$ and $\boldsymbol{X}$ are much smaller than the horizontal variation, we can practically ignore the vertical component of $\boldsymbol{\alpha}_1(t)$ and $\boldsymbol{\alpha}_2(t)$. Thus, $\boldsymbol{\alpha}_1(t)$ and $\boldsymbol{\alpha}_2(t)$ are reduced to a 2-dimensional vector to denote the horizontal gradient.

Each coefficient can be represented by a linear combination of basis functions $\Phi_k(t)$:

$$\begin{cases} \alpha_0(t) = \sum_{k=0}^{K^{\langle 0 \rangle}} a_k^{\langle 0 \rangle} \Phi_k^{\langle 0 \rangle}(t) \\ \boldsymbol{\alpha}_1(t) = \left(\sum_{k=0}^{K^{\langle 1E \rangle}} a_k^{\langle 1E \rangle} \Phi_k^{\langle 1E \rangle}(t) \quad \sum_{k=0}^{K^{\langle 1N \rangle}} a_k^{\langle 1N \rangle} \Phi_k^{\langle 1N \rangle}(t) \quad 0 \right), \\ \boldsymbol{\alpha}_2(t) = \left(\sum_{k=0}^{K^{\langle 2E \rangle}} a_k^{\langle 2E \rangle} \Phi_k^{\langle 2E \rangle}(t) \quad \sum_{k=0}^{K^{\langle 2N \rangle}} a_k^{\langle 2N \rangle} \Phi_k^{\langle 2N \rangle}(t) \quad 0 \right) \end{cases} \tag{2.5}$$

where $a_k^{\langle \cdot \rangle}$ are the coefficients of the kth basis function, $\Phi_k^{\langle \cdot \rangle}(t)$, for each term named $\langle \cdot \rangle$. E and N in $\langle \cdot \rangle$ denote the eastward and northward components of the vector, respectively. For simplification, we compile these coefficients into vector $\boldsymbol{a}$, hereafter.

Because the initial values for $\boldsymbol{M}$ and $\boldsymbol{X}_j$ are usually obtained in the precision of less than meters prior to the GNSS-A analysis, we approximate $\boldsymbol{P}$ and $\boldsymbol{X}_j$ in Γ substituting the initial values, i.e., $\boldsymbol{M}^0$ and $\boldsymbol{X}_j^0$, and not updating them with the iteration. This reduces the number of estimation parameters in the correction term, i.e., $\gamma_i = \gamma_i\left(\boldsymbol{a} \middle| \boldsymbol{X}_j^0, \boldsymbol{M}^0, \boldsymbol{Q}(t), \boldsymbol{\Theta}(t)\right)$.

2.3.2 Observation equation

In the GNSS-A analysis, observed travel time, T_i^o, are compared with the model, T_i^c. For the interpretability of variables and the simplification in the expansion, we took the logarithms of travel time. Summarizing the above expansion, we put the following observation equation

for ith acoustic round-trip travel time:

$$\log(T_i^o/T^*) = \log\left(\tau_i\left(\boldsymbol{X}_j, \boldsymbol{M}\middle|\boldsymbol{Q}, \boldsymbol{\Theta}, V_0\right)/T^*\right) - \gamma_i\left(\boldsymbol{a}\middle|\boldsymbol{X}_j^0, \boldsymbol{M}^0, \boldsymbol{Q}, \boldsymbol{\Theta}\right) + e_i, \tag{2.6}$$

where T^* is the characteristic travel time and e_i is the observation error vector. Figure 2-2 indicates the summary for constructing the observation equation. It should be noted that, in this formulation, the continuity of sound speed field is assumed.

2.3.3 Expression of rigid array constraints

Usually, the local deformation within the transponders' array is assumed to be sufficiently small, so that the same array geometry parameters can be used throughout all visits. Because the relative positions of the transponders in the array are strongly coupled with the sound speed estimates and the position of array centroid, constraining the array geometry is expected to stabilize the GNSS-A solutions. Matsumoto et al. (2008) developed the rigid-array constraint, which has been adopted in the subsequent studies (e.g., Watanabe et al., 2014; Yokota et al., 2016) except in the cases where the rigid-array assumption is inadequate (e.g., Sato et al., 2011).

To implement the rigid-array constraint, slight change in the observation equation is needed. We divide the transponders' positions as $\boldsymbol{X}_j = \overline{\boldsymbol{X}_J} + \boldsymbol{\Delta X}$, where $\overline{\boldsymbol{X}_J}$ and $\boldsymbol{\Delta X}$ denote the relative positions of each transponder and the parallel translation of the transponder array, respectively. The observation equation in the form with the rigid-array constraint is written as,

$$\log(T_i^o/T^*) = \log\left(\tau_i\left(\boldsymbol{\Delta X}, \boldsymbol{M}\middle|\overline{\boldsymbol{X}_J}, \boldsymbol{Q}, \boldsymbol{\Theta}, V_0\right)/T^*\right) - \gamma_i\left(\boldsymbol{a}\middle|\boldsymbol{X}_j^0, \boldsymbol{M}^0, \boldsymbol{Q}, \boldsymbol{\Theta}\right) + e_i. \tag{2.7}$$

The array geometry, $\overline{\boldsymbol{X}_J}$, should be determined prior to the analytical procedure, using the data of multiple observation visits.

Meanwhile, $\overline{\boldsymbol{X}_J}$ can also be determined simultaneously with the positioning procedure by combining the data vectors, model parameter vectors, and observation equation for all series of the observation visits, as the original formulation of Matsumoto et al. (2008). However, it requires huge computational resources to solve all the parameters, as the number of observations increases. Therefore, we are not concerned with the simultaneous determination of the array geometry in this chapter.

2.3.4 Comparison with other models

As mentioned in Section 2.2.1, it is convenient to relate the correction coefficient to the sound speed perturbation by assuming the case for $|\gamma_i| \ll 1$ for better understanding, though observation equation (2.6) is valid for arbitrary value of γ_i. For the relationship $\delta V_i \sim \gamma_i \overline{V_0}$, we can convert each term of Γ into the dimension of speed and speed gradient as, $\delta V_0(t) \equiv \overline{V_0}\alpha_0(t)$, $\boldsymbol{g}_1(t) \equiv \overline{V_0}\boldsymbol{\alpha}_1(t)$, and $\boldsymbol{g}_2(t) \equiv \overline{V_0}\boldsymbol{\alpha}_2(t)$.

The early models by Fujita et al. (2006) and Ikuta et al. (2008) took only the term $\delta V_0(t)$ into account. Whereas Ikuta et al. (2008) used the cubic B-spline functions as basis functions, Fujita et al. (2006) applied the multiple 2nd degree polynomial functions with 10-20-minute time windows. Although these models do not include any transponder dependent term $\boldsymbol{g}_2(t)$, the transponder independent spatial gradient $\boldsymbol{g}_1(t)$ can be indirectly extracted as shown by Yokota et al. (2019).

In addition to estimating the term identical to δV_0, Yokota et al. (2019) implemented the additional process to estimate $\boldsymbol{g}_2$ from the residuals of the solution by the method of Fujita et al. (2006). Strictly, the derived parameters in their scheme, i.e., ΔV_1 and ΔV_2 in Yokota et al. (2019), are the same as $\boldsymbol{g}_1 + \boldsymbol{g}_2$ and $\boldsymbol{g}_2$ in this study, respectively. For these parameters, Yokota and Ishikawa (2019) have already made a qualitative interpretation.

To show the relationship with other conventional models, we expand the proposed formulation to those by Honsho et al. (2019), Yasuda et al. (2017) and Kinugasa et al. (2020). Because Honsho et al. (2019) practically assumed 1-directional sound speed gradient, they constructed the model basically in the 2-dimensional plane spanned by the gradient direction and vertical direction.

For simplification, we assume that the ray path is a straight line connecting both ends. Putting L^* equal to the depth of the observation site, the emission angle θ defined in Figure 3 of Honsho et al. (2019) can be expressed as,

$$\frac{X_j}{L^*} - \frac{P(t)}{L^*} = \tan\theta\,. \tag{2.8}$$

Furthermore, assuming that the transmit/reception positions are the same and that the difference between transmit/reception time is so small that $\alpha_0(t)$, $\alpha_1(t)$ and $\alpha_2(t)$ hardly change, γ_i can be written as,

$$\gamma_i = \alpha_0(t) + \big(\alpha_1(t) + \alpha_2(t)\big)\frac{P(t)}{L^*} + \alpha_2(t)\tan\theta\,. \tag{2.9}$$

Because δT defined in eqs. (2) and (5) of Honsho et al. (2019) is equivalent to $T_i^c - \tau_i$ in our formulation, we have,

$$(\exp(-\gamma_i) - 1)\tau_i = \frac{1}{\cos\theta}(c_0(t) + g(t)x_0 + w(t)\tan\theta), \tag{2.10}$$

where $c_0(t)$, $g(t)$, $w(t)$ and $x_0 = P$ are defined in eqs. (6), (7), and (8) of Honsho et al. (2019) and the transducer's position in their formulation, respectively. Recalling that the slant range of acoustic ray path is $2L^*/\cos\theta$, the reference round-trip travel time can be written as,

$$\tau_i = \frac{2L^*}{\overline{V_0(u)}\cos\theta}. \tag{2.11}$$

Considering the case where $|\gamma_i| \ll 1$, eq. (2.10) is approximated to,

$$-\frac{2L^*}{\overline{V_0}}\gamma_i = c_0(t) + g(t)x_0 + w(t)\tan\theta\,. \tag{2.12}$$

From eqs. (2.9) and (2.12), the following relationships are derived:

$$\begin{cases} c_0(t) = -\dfrac{2L^*}{\overline{V_0}}\alpha_0(t) \\ g(t) = -\dfrac{2}{\overline{V_0}}\big(\alpha_1(t) + \alpha_2(t)\big), \\ w(t) = -\dfrac{2L^*}{\overline{V_0}}\alpha_2(t) \end{cases} \tag{2.13}$$

In Honsho et al. (2019), $w(t)$ is extended to a 2-dimensional vector, i.e.,

$$\boldsymbol{w}(t) = -\frac{2L^*}{\overline{V_0}}\boldsymbol{\alpha}_2(t). \tag{2.14}$$

Similarly, when extending $g(t)$ to the 2-dimensional vector, we can use the following vector form:

$$\boldsymbol{g}(t) = -\frac{2}{\overline{V_0}}\big(\boldsymbol{\alpha}_1(t) + \boldsymbol{\alpha}_2(t)\big), \tag{2.15}$$

though they consequently use the assumption that $\boldsymbol{g}(t)$ is parallel to $\boldsymbol{w}(t)$. It is equivalent to the case that $\boldsymbol{\alpha}_1$ is parallel to $\boldsymbol{\alpha}_2$ in the proposed formulation.

Honsho et al. (2019) supposed the physical model where a spatially homogeneous 1-directional gradient of slowness lies in the certain layer, from sea-surface to the depth D, in the water. In such cases, $\boldsymbol{w}(t)$ is proportional to $\boldsymbol{g}(t)$, as $\boldsymbol{w} = (D/2)\boldsymbol{g}$. This is exactly the same assumption as the model by Yasuda et al. (2017). The model of Kinugasa et al. (2020) is the special case of those models where D equals to the water depth.

In the proposed method, the sound speed field is approximately interpreted by their models when the unit vector of $\boldsymbol{\alpha}_1$ is supposed to be same as that of $\boldsymbol{\alpha}_2$ and $|\boldsymbol{\alpha}_1| \geq |\boldsymbol{\alpha}_2|$. The depth of the gradient layer is calculated as,

$$D = \frac{2L^*}{1 + \boldsymbol{\alpha}_1/\boldsymbol{\alpha}_2}. \tag{2.16}$$

When $\boldsymbol{\alpha}_1 = \boldsymbol{\alpha}_2$, it concludes to the model of Kinugasa et al. (2020). Conversely, when $|\boldsymbol{\alpha}_2| \ll |\boldsymbol{\alpha}_1|$, sound speed gradient lies in the thin layer near the surface.

In addition to the simple model above, the proposed method can extract more complicated sound speed field, which partly described by Yokota and Ishikawa (2019). Additionally, the proposed model has an advantage in avoiding the singularity in the Jacobian matrix in the case where the parameter for the depth of gradient sound speed layer is explicitly included — that would be why Honsho et al. (2019) treated the parameter as a hyperparameter. Extracted model parameters for the sound speed perturbation in the proposed method indicate the complicity of oceanographic structure, as shown in the next section.

2.4 Analytical procedures

This section shows the algorithm to estimate the model parameters from the nonlinear observation equation (2.6). We took a Bayesian approach because of its simple expression when incorporating prior information. Furthermore, it provides a well-defined index for the model selection, i.e., the Akaike's Bayesian Information Criterion (ABIC; Akaike, 1980). The expansion shown in this section is based on Tarantola and Valette (1982) and Matsu'ura et al. (2007).

2.4.1 Prior information

The observation equation can be rewritten as,

$$\boldsymbol{y} = \boldsymbol{f}(\boldsymbol{x}) + \boldsymbol{e}, \tag{2.17}$$

where $\boldsymbol{x} = \begin{bmatrix} \boldsymbol{X}_j^T & \boldsymbol{M}^T & \boldsymbol{a}^T \end{bmatrix}^T$, $y_i = \log(T_i^o / T^*)$, and $f_i = \log(\tau_i / T^*) - \gamma_i$. Let us consider the direct prior information for the model parameters $\boldsymbol{X}_j$ and $\boldsymbol{M}$ written as,

$$\begin{bmatrix} \boldsymbol{X}_j^0 \\ \boldsymbol{M}^0 \end{bmatrix} = \begin{bmatrix} \boldsymbol{X}_j \\ \boldsymbol{M} \end{bmatrix} + \begin{bmatrix} \boldsymbol{d}_X \\ \boldsymbol{d}_M \end{bmatrix}, \tag{2.18}$$

where $\boldsymbol{X}_j^0$, $\boldsymbol{M}^0$ and $\boldsymbol{d} = [\boldsymbol{d}_X^T \quad \boldsymbol{d}_M^T]^T$ denote the predicted model parameter vectors and the error vector, respectively. Let us assume that $\boldsymbol{d}_X$ and $\boldsymbol{d}_M$ follow a normal distribution with a variance-covariance of $D_X(\rho^2)$ and $D_M(\rho^2)$, whose scale can be adjusted by a hyperparameter ρ^2, i.e., $D_X = \rho^2 \widetilde{D_X}$ and $D_M = \rho^2 \widetilde{D_M}$, respectively. The prior probability density function (pdf) for the constraints can be written as,

$$p(\boldsymbol{X}_j, \boldsymbol{M}; \rho^2) = c \cdot \exp\left[-\frac{1}{2} \left(\begin{bmatrix} \boldsymbol{X}_j^0 \\ \boldsymbol{M}^0 \end{bmatrix} - \begin{bmatrix} \boldsymbol{X}_j \\ \boldsymbol{M} \end{bmatrix} \right)^T \begin{bmatrix} D_X(\rho^2) & 0 \\ 0 & D_M(\rho^2) \end{bmatrix}^{-1} \left(\begin{bmatrix} \boldsymbol{X}_j^0 \\ \boldsymbol{M}^0 \end{bmatrix} - \begin{bmatrix} \boldsymbol{X}_j \\ \boldsymbol{M} \end{bmatrix} \right) \right], \tag{2.19}$$

where c denotes the normalization constant.

For the model parameter $\boldsymbol{a}$, an indirect prior information can be applied that the temporal change of sound speed perturbation model Γ is small. Specifically, the roughness which can be defined by the derivatives of each term in eq. (2.4) should be small. In this study, we use the square of second derivative as roughness ϕ, whereas Ikuta et al. (2008) used the first derivative. When using the B-spline functions $\Phi_k^{\langle\cdot\rangle}(t)$ (e.g., de Boor, 1978) as the basis of temporal sound speed variation, the roughness can be written in a vector form, i.e.,

$$\phi = \int_t \left(\frac{\partial^2 \alpha_{\langle\cdot\rangle}(t)}{\partial t^2} \right)^2 dt = \boldsymbol{a}^{\langle\cdot\rangle T} H_{\langle\cdot\rangle} \boldsymbol{a}^{\langle\cdot\rangle}, \tag{2.20}$$

where,

$$H_{\langle\cdot\rangle ij} = \int \frac{\partial^2 \Phi_i^{\langle\cdot\rangle}(t)}{\partial t^2} \frac{\partial^2 \Phi_j^{\langle\cdot\rangle}(t)}{\partial t^2} dt .$$

Then, the prior pdf can be written using the hyperparameter $\lambda_{\langle\cdot\rangle}$ as,

$$p(\boldsymbol{a}^{\langle\cdot\rangle}; {\lambda_{\langle\cdot\rangle}}^2) = c \cdot \exp\left[-\frac{1}{2\lambda_{\langle\cdot\rangle}^2} \boldsymbol{a}^{\langle\cdot\rangle T} H_{\langle\cdot\rangle} \boldsymbol{a}^{\langle\cdot\rangle} \right], \tag{2.21}$$

where c denotes the normalization constant.

Combining these prior informations, we obtain the following prior pdf:

$$p(\boldsymbol{x};\rho^2,\boldsymbol{\lambda}^2) = (2\pi)^{-\frac{g}{2}}\|\Lambda_G\|^{\frac{1}{2}}\exp\left[-\frac{1}{2}(\boldsymbol{x}^0-\boldsymbol{x})^T G(\rho^2,\boldsymbol{\lambda}^2)(\boldsymbol{x}^0-\boldsymbol{x})\right], \tag{2.22}$$

with,

$$\begin{cases} \boldsymbol{\lambda}^2 = \begin{bmatrix}{\lambda_0}^2 & {\lambda_{1E}}^2 & {\lambda_{1N}}^2 & {\lambda_{2E}}^2 & {\lambda_{2N}}^2\end{bmatrix} \\ \boldsymbol{x}^0 = \begin{bmatrix}\boldsymbol{X}_j^{0T} & \boldsymbol{M}^{0T} & \boldsymbol{0}^T\end{bmatrix}^T \\ G(\rho^2,\boldsymbol{\lambda}^2) = \begin{bmatrix} D_X(\rho^2)^{-1} & & \\ & D_M(\rho^2)^{-1} & \\ & & H_{\langle\cdot\rangle}/{\lambda_{\langle\cdot\rangle}}^2 \end{bmatrix} \end{cases},$$

where g and $\|\Lambda_G\|$ represent the rank of G and the absolute value of the product of non-zero eigenvalues of G, respectively.

2.4.2 Variance-covariance of data error

Now for the observed data, we take the assumption that $\boldsymbol{e}$ also follows a normal distribution with a variance-covariance of $\sigma^2 E$, i.e.,

$$p(\boldsymbol{y}|\boldsymbol{x};\sigma^2) = (2\pi\sigma^2)^{-\frac{n}{2}}|E|^{-\frac{1}{2}}\exp\left[-\frac{1}{2\sigma^2}\big(\boldsymbol{y}-\boldsymbol{f}(\boldsymbol{x})\big)^T E^{-1}\big(\boldsymbol{y}-\boldsymbol{f}(\boldsymbol{x})\big)\right], \tag{2.23}$$

where n is the number of data and $|\cdot|$ denotes the determinant of the matrix.

The major error sources for the measurement and calculation of travel time are (1) measurement error when reading the return signal, (2) transducer's positioning error, and (3) modeling error of the sound speed field. Non-diagonal components of E are caused not by measurement error, but by transducer's positioning error and sound speed modeling error. The transducer's positioning error may have temporal correlation which comes from the kinematic GNSS noise. The modeling error has spatio-temporal correlation because the sound speed variation is modeled by a smooth function of space and time. Thus, we assumed the following covariance terms using two hyperparameters, i.e., μ_t and μ_{MT}, to adjust the non-diagonal component of E:

$$E_{ij}(\mu_t, \mu_{MT}) = \begin{cases} \sqrt{E_{ii}E_{jj}} \exp\left(-\dfrac{|t_i - t_j|}{\mu_t}\right) & \text{if transponders for } i \text{ and } j \text{ are the same} \\ \mu_{MT}\sqrt{E_{ii}E_{jj}} \exp\left(-\dfrac{|t_i - t_j|}{\mu_t}\right) & \text{for others} \end{cases}, \quad (2.24)$$

whose formulation refers to Fukahata and Wright (2008). Eq. (2.24) means that the densely sampled data would have smaller weights in the model than the isolated data. A factor $\mu_{MT} \in [0, 1]$ was introduced to surpress the error correlation between the different transponders because the acoustic rays for different transponders take separate paths as the depths increases. Consideration of the non-diagonal components of the data variance-covariance contributes to reduce the complexity of the model against the excessively high-rate data sampling.

Subsequently, we consider the diagonal component of E which controls the weight of individual data. Because the measurement errors of acoustic travel time are caused by mis-reading of the return signal, it is independent on the travel time value. Therefore, it is reasonable to put the assumption that the error of $T_i^o - T_i^c$ follows a normal distribution. Nonetheless, because the GNSS-A typically gives the precision of $T_i^o/T_i^c \sim 1 \pm 10^{-4}$, we can suppose that T_i^o/T_i^c approximately follows a log-normal distribution as assumed in eq. (2.23). To put the same weight for all measured travel time in the real scale, we applied $E_{ii} = (T^*/T_i^o)^2$ for scaling the diagonal component.

2.4.3 Posterior probability

The posterior pdf after the data acquisition, which can be defined to be equal to the likelihood of the model parameter with the given data, can be written as,

$$p(\boldsymbol{x}; \sigma^2, \mu_t, \mu_{MT}, \rho^2, \boldsymbol{\lambda}^2 | \boldsymbol{y}) = c \cdot (2\pi\sigma^2)^{-\frac{(n+g)}{2}} |E|^{-\frac{1}{2}} \left\| \widetilde{\Lambda_G} \right\|^{\frac{1}{2}} \exp\left[-\frac{1}{2\sigma^2} s(\boldsymbol{x})\right], \quad (2.25)$$

with,

$$s(\boldsymbol{x}) = \big(\boldsymbol{y} - \boldsymbol{f}(\boldsymbol{x})\big)^T E^{-1} \big(\boldsymbol{y} - \boldsymbol{f}(\boldsymbol{x})\big) + (\boldsymbol{x}^0 - \boldsymbol{x})^T \tilde{G} (\boldsymbol{x}^0 - \boldsymbol{x}),$$

where $\tilde{G} = \sigma^2 G(\rho^2, \boldsymbol{\lambda}^2)$ and $\left\| \widetilde{\Lambda_G} \right\|$ represents the absolute value of the product of non-zero eigenvalues of $\tilde{G}$.

Defining $\hat{\boldsymbol{x}}(\sigma^2, \mu_t, \mu_{MT}, \rho^2, \boldsymbol{\lambda}^2)$ as $\boldsymbol{x}$ that maximizes the posterior probability given as eq. (2.25) under the given hyperparameters, the partial derivative of $p(\boldsymbol{x}|\boldsymbol{y})$ with respect to $\boldsymbol{x}$

should be zero for $\boldsymbol{x} = \hat{\boldsymbol{x}}$. Hence, $\hat{\boldsymbol{x}}$ should satisfy the following equation:

$$A(\hat{\boldsymbol{x}})^T E^{-1}\big(\boldsymbol{y} - \boldsymbol{f}(\hat{\boldsymbol{x}})\big) + \tilde{G}(\boldsymbol{x}^0 - \hat{\boldsymbol{x}}) = \boldsymbol{0}, \tag{2.26}$$

where $A(\boldsymbol{x})$ is the Jacobian matrix at point $\boldsymbol{x}$ defined as,

$$A(\boldsymbol{x}) = \begin{bmatrix} \frac{\partial f_1}{\partial x_{k1}}(\boldsymbol{x}) & \cdots & \frac{\partial f_1}{\partial x_{km}}(\boldsymbol{x}) \\ \vdots & \ddots & \vdots \\ \frac{\partial f_n}{\partial x_{k1}}(\boldsymbol{x}) & \cdots & \frac{\partial f_n}{\partial x_{km}}(\boldsymbol{x}) \end{bmatrix}.$$

We can solve the nonlinear eq. (2.26) numerically by performing an iterative method, where $\boldsymbol{x}_k$ is corrected in each step with the following algorithm:

$$\boldsymbol{x}_{k+1} = \boldsymbol{x}_k + \big(A(\boldsymbol{x}_k)^T E^{-1} A(\boldsymbol{x}_k) + \tilde{G}\big)^{-1}\Big(A(\boldsymbol{x}_k)^T E^{-1}\big(\boldsymbol{Y} - \boldsymbol{f}(\boldsymbol{x}_k)\big) + \tilde{G}(\boldsymbol{x}^0 - \boldsymbol{x}_k)\Big), \tag{2.27}$$

to satisfy the following convergence criteria:

$$A(\boldsymbol{x}_k)^T E^{-1}\big(\boldsymbol{Y} - \boldsymbol{f}(\boldsymbol{x}_k)\big) + \tilde{G}(\boldsymbol{x}^0 - \boldsymbol{x}_k) \ll 1. \tag{2.28}$$

Ignoring the term $O((\boldsymbol{x} - \hat{\boldsymbol{x}})^2)$ in $f(\boldsymbol{x})$ around $\hat{\boldsymbol{x}}$, $s(\boldsymbol{x})$ can be rewritten as,

$$s(\boldsymbol{x}) \sim s(\hat{\boldsymbol{x}}) + (\boldsymbol{x} - \hat{\boldsymbol{x}})^T\big(A(\hat{\boldsymbol{x}})^T E^{-1} A(\hat{\boldsymbol{x}}) + \tilde{G}\big)(\boldsymbol{x} - \hat{\boldsymbol{x}}). \tag{2.29}$$

Therefore, the linearized variance-covariance matrix around $\hat{\boldsymbol{x}}$ can be obtained as,

$$\hat{C} = \sigma^2\big(A(\hat{\boldsymbol{x}})^T E^{-1} A(\hat{\boldsymbol{x}}) + \tilde{G}\big)^{-1}. \tag{2.30}$$

2.4.4 Hyperparameter tuning

The appropriate values of the hyperparameters can be determined by minimizing Akaike's Bayesian Information Criteria (ABIC; Akaike, 1980),

$$\mathrm{ABIC} = -2\log\int p(\boldsymbol{y}|\boldsymbol{x};\sigma^2,\mu_t,\mu_{MT})p(\boldsymbol{x};\rho^2,\boldsymbol{\lambda}^2)\,d\boldsymbol{x} + 2N_{\mathrm{HP}}, \tag{2.31}$$

where N_{HP} denotes the number of hyperparameters. Although it is difficult to analytically calculate the integral for the marginal likelihood because of the nonlinearity in $\boldsymbol{f}(\boldsymbol{x})$, the Laplace's method can be applied in this case where the degree of freedom is sufficiently large and $s(\boldsymbol{x})$ can be almost unimodal. Thus, an approximated form for ABIC is obtained as follows:

$$\mathrm{ABIC} \cong (n+g-m)\log s(\hat{\boldsymbol{x}}) - \log|E^{-1}| - \log\|\Lambda_G\| + \log\left|A(\hat{\boldsymbol{x}})^T E^{-1} A(\hat{\boldsymbol{x}}) + \tilde{G}\right| + const. \quad (2.32)$$

where m is the number of model parameters. For the derivation, we used the following relationship:

$$\sigma^2 = \frac{s(\hat{\boldsymbol{x}})}{n+g-m}, \quad (2.33)$$

which is derived from the condition that the partial derivative of ABIC with respect to σ^2 should be zero. We can tune the hyperparameters to minimize the approximated ABIC value defined in eq. (2.32), to obtain the solution $\boldsymbol{x}^* = \hat{\boldsymbol{x}}\left(\sigma^{2^*}, \mu_t^*, \mu_{MT}^*, \rho^{2^*}, \boldsymbol{\lambda}^{2^*}\right)$, where $\cdot^*$ denotes the selected hyperparameters.

2.5 Concluding remarks

We extracted the general expression for GNSS-A observation with explicitly expanding the effects of sound speed perturbation and demonstrated one of the estimation procedures using the empirical Bayes approach. The proposed expression of sound speed variation approximately includes all the conventional models. Moreover, in this expression, we can easily replace the sound speed perturbation model eq. (2.4) with more simple or complicate ones to reflect the realistic spatiotemporal structure depending on the oceanographic features in the site.

Introducing the non-diagonal components for variance-covariance of data error reduces the impact of data which are densely obtained (see Section 4.4 for the effects on the actual data). Although the derived GNSS-A solution is not based on the full Bayesian approach such as using the Markov chain Monte Carlo (MCMC) algorithms, the proposed approach compatibly achieves both stable positioning (see Chapter 4) and lower computational cost. On the other hand, there should be a room for further improvement of computational procedures such as the application of machine learning.

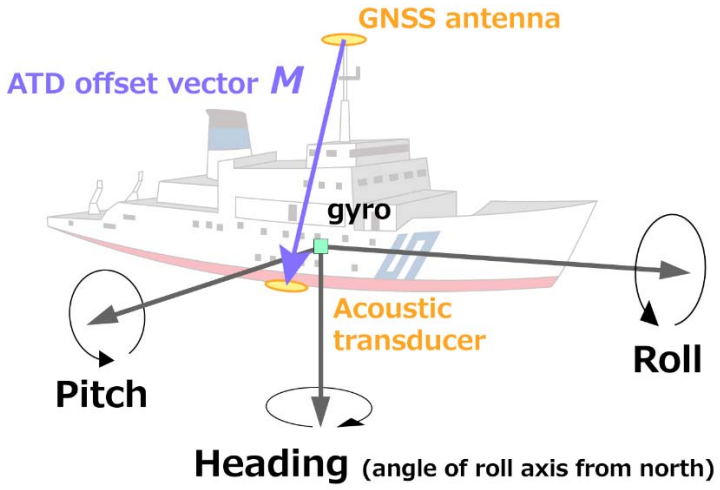

Figure 2-1. Definitions of the attitude parameters and the ATD offset vector for the sea-surface platform. Heading is zero when the roll axis directs to the north. The roll and pitch axes direct forward and rightward (portside) of the vessel, respectively. The figure is adapted from Watanabe et al. (2020c).

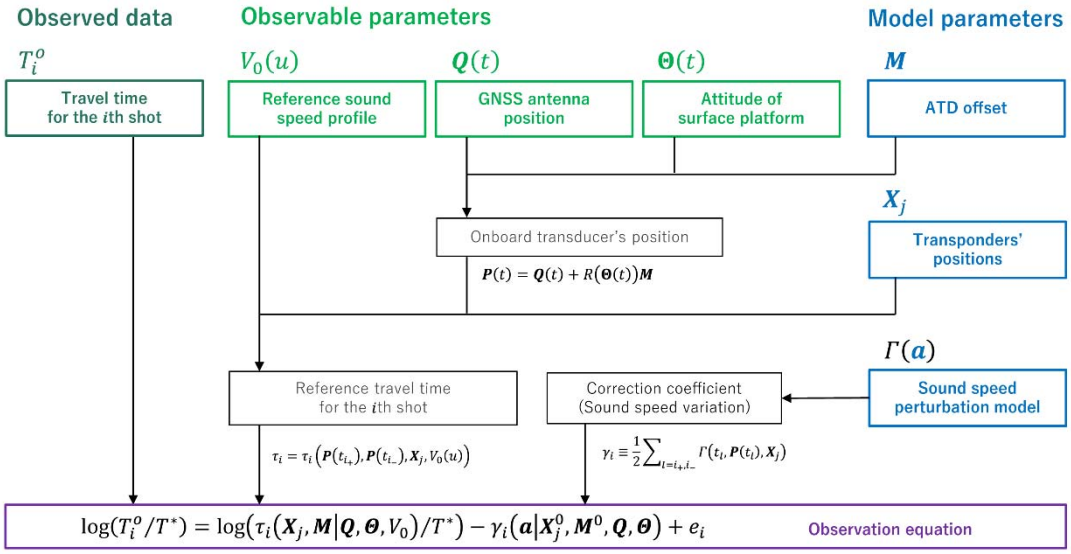

Figure 2-2. Flow chart to construct the observation equation (after Watanabe et al., 2020c).

Chapter 3

Implementation of Precise Point Positioning to GNSS-A seafloor geodesy

---

This Chapter references the author's works published as Watanabe et al. (2017) for Section 3.2 and Watanabe et al. (2020d) for Section 3.3.

References:

Watanabe, S., Bock, Y., Chadwell, C. D., Fang, P., and Geng, J. (2017) Long-term stability of the kinematic precise point positioning for the sea surface observation unit compared with the baseline analysis. *Rep. Hydro. Ocean. Res.*, **54**, 38–73.

Watanabe, S., Yokota, Y., and Ishikawa, T. (2020d) Stability Test to Validate the GNSS-A Seafloor Positioning with Kinematic Precise Point Positioning [in Japanese with English abstract and captions]. *J. Geod. Soc. Japan*, **66**, 1–7, doi:10.11366/sokuchi.66.1

3.1 Background

As described in Chapter 2, precise kinematic positioning in the open ocean is a key component of the GNSS-A observation. It requires the kinematic positioning of the sea-surface platform with an accuracy of several centimeters to detect the seafloor displacement due to the plate motion and plate boundary deformation. As of 2020, the kinematic differential GNSS software "Interferometric Translocation" (IT; e.g., Colombo, 1998) version 4.2 is used for the GNSS-A routine analysis (Fujita et al., 2006) in the Japan Coast Guard (JCG). The accuracy and stability of IT had been discussed by several researchers in the JCG (e.g., Fujita and Yabuki, 2003; Kawai et al., 2006; Saito et al., 2010b). Kawai et al. (2006) showed that IT

provided the stable results for the baseline range within 1000 km, which is a big advantage of IT for the use at the seismogenic zone along the major trenches.

In the JCG's routine GNSS-A analysis, the seafloor positions were aligned to the F3 solution of GEONET (Nakagawa et al., 2009) operated by the Geospatial Information Authority of Japan (GSI). For the baseline analysis, the GSI collects and provides the 1 Hz GNSS RINEX data to the JCG on their request, based on the inter-institutional data exchange agreement. However, non-automated on-demand data collection and transfer would cause vulnerability and/or larger latency, especially when the urgent analysis is required for the prompt investigations for such as devastating earthquake. It is also plausible that the data transfer or in-situ data collection will be stopped because of the earthquake.

Meanwhile, the technique of Precise Point Positioning (PPP; Zumberge et al., 1997) is actually free from the limitation of distance and reference sites. PPP is useful when there is a need for precise dynamic position of the survey vessels in near real-time, because it does not require the transfer of additional high rate GNSS data at the terrestrial reference sites (more than 1 Hz) to the vessels. The reason for "near" real-time is due to the latency of collecting acoustic signals for the static seafloor positioning is longer than GNSS signal acquisition. It should be noted that high quality orbits and clocks should be available when using PPP.

The kinematic PPP using adequate orbit and clock products, which are available via the internet, can provide the sufficiently precise GNSS solutions for the purpose of the GNSS-A seafloor positioning (e.g., Ohta et al., 2006; Guo et al., 2010). Geng et al. (2010) reported that their PPP results for the vessel sailing in the Bohai Sea achieved a horizontal accuracy of 1 cm when using a reference network with an extent of a few thousand kilometers. If its accuracy is stably achieved in the Pacific, PPP would be an alternative way to determine the vessel's position.

In this Chapter, we firstly evaluate the accuracy and stability of kinematic PPP results processed by several software, using the actual GNSS data collected for the GNSS-A observation (Section 3.2). Secondly, we investigate the influence of GNSS solutions on the GNSS-A results, aiming to the implementation of PPP to the routine GNSS-A analysis (Section 3.3).

3.2 Differences in kinematic GNSS solutions

3.2.1 Data and Methods

In this Section, we evaluate the accuracy and stability of kinematic PPP results processed by several software, using the ship-borne 2 Hz GNSS data (dual frequency) collected on the mast of the survey vessels for the GNSS-A observation as the rover station (Table 3-1). We reduced the rover's GNSS data to 1 Hz, to compare them with 1 Hz terrestrial GNSS sites, which are used as the reference sites for the baseline analysis, at the same sampling rate. The locations of the GNSS-A sites (i.e., approximate area of the rover's track) are shown in Figures 3-1 and 3-2. The rover's GNSS data were processed by the following PPP software; PANDA (Shi et al., 2008) and RTKLIB ver. 2.4.2 (Takasu, 2013).

PANDA is the software used in the Scripps Orbit and Permanent Array Center (SOPAC). It has been modified at SOPAC for real-time earthquake and tsunami warning systems (Geng et al., 2013; Melgar and Bock, 2015). The satellite clock and the fractional cycle bias (FCB) were estimated using the regional GNSS network by PANDA, which enables us to fix ambiguities for kinematic PPP (Ge et al., 2008; Geng et al., 2009). Geng et al. (2010) had studied the dependency of the accuracy on the scale of the reference network, and suggested that an accuracy of several centimeters requires the network width of up to several thousand kilometers. However, because the IGS (International GNSS Service) stations around Japan are largely affected by the co- and post-seismic deformation associated with the 2011 Tohoku-oki earthquake (M_w9.0), we selected the IGS stations in broader area for the network solution (Figure 3-1). Another software, RTKLIB, has the GUI (graphical user interface) mode for Widows OS, which is an advantage for users who are unfamiliar with the CUI (character user interface) to learn and use rather than other software. We also processed the rover's data by RTKLIB in post-processing PPP mode to compare the results. We used the IGS final product for the satellite clock data with the interval of 30 sec for RTKLIB (International GNSS Service, b).

To compare the results by PPP with the differential positioning, we determined the rover's position using IT ver. 4.2 in differential mode. The 1 Hz GNSS data collected at the GEONET sites operated by the Geospatial Information Authority of Japan (GSI) were used as the reference (Table 3-1, Figure 3-2). We fixed their positions to the daily F3 position (Nakagawa et al., 2009), taking the 7-day average after removing the 2-sigma outliers. We used the satellite orbits and the earth rotation parameters from the IGS final products (International GNSS Service, a) for all analysis. Configurations for three methods are

summarized in Table 3-2.

In addition to the GNSS data in Japan, we processed the data in the western off the Pacific coast of southern California, United States, using PANDA and RTKLIB (Table 3-1, Figure 3-3), which had been collected on the buoy operated by the Scripps Institution of Oceanography (hereafter called SIO buoy data). We then compared the results with the ambiguity-fixed PPP solution using GIPSY software (Bertiger et al., 2010), which is developed by the Jet Propulsion Laboratory, NASA (https://gipsy-oasis.jpl.nasa.gov/). The IGS stations used for the reference network for PANDA are shown in Figure 3-3.

3.2.2 Results

Some examples for the position differences for the JCG's GNSS data in the local ENU coordinates between (i) PANDA and RTKLIB, and (ii) PANDA and IT are shown in Figures 3-4 and 3-5, respectively. Results for all experiments for JCG's GNSS data are available in Figures 4 and 5 of Watanabe et al. (2017). The positions of the reference stations used in IT were also solved by PANDA as the pseudo-kinematic rover stations (displayed as green lines in Figure 3-5).

The averages and standard deviations of the position difference are shown in Table 3-3. The results indicate that PANDA and RTKLIB provided the consistent results within a few centimeters for the horizontal component. Standard deviations of horizontal discrepancy were less than 2 cm, except the campaign on 2015/09/12 at HYG2 where the differences were increased at the end of the session. On the other hand, standard deviations of vertical discrepancies were up to 10 cm. As shown in the time series (Figure 3-4 and Figure 4 of Watanabe et al., 2017), the vertical discrepancies in some campaigns steeply increased with more than 20 cm for 10–30 minutes. It caused the larger standard deviations in the vertical component.

The results by IT had biases of several centimeters from the PPP results. As shown in Figure 3-5 and Figure 5 of Watanabe et al. (2017), the long-term variations including the offset of the position difference were similar to those of the reference sites. Their standard deviations were the same as those of differences between PANDA and RTKLIB within 1–2 cm, except several cases such as the campaign on 2015/04/27 at TU12 with the reference site 0175. Because the other baseline results were consistent with the PPP results, it is likely that large discrepancies in these cases came from the bad solutions of IT.

The statistics in Table 3-3 are summarized in Figure 3-6, which shows the distribution of

position differences between PANDA – RTKLIB and PANDA – IT solutions for each observation epoch. Upper and lower panels show the case for "best" and "worst" IT solutions, in terms of the minimum and maximum standard deviations of position difference, respectively. The biases of PANDA–IT position difference tend to have larger variations than PANDA–RTKLIB position difference, even in the case of "best" IT solution.

The position differences for the SIO buoy data in the local ENU coordinates between (1) GIPSY and PANDA, and (2) GIPSY and RTKLIB are shown in Figure 3-7. The averages and standard deviations of the position difference are shown in Table 3-4. Whereas the results by GIPSY and PANDA showed good agreement within 0.4–0.6 cm and 2 cm in standard deviation for horizontal and vertical components, respectively, the standard deviations of the differences between GIPSY and RTKLIB were several times larger than those of GIPSY and PANDA.

3.2.3 Discussion

The results indicated that discrepancies of several centimeters in standard deviation were found between the three different GNSS software. In some cases of the IT solution, the selection of the reference site would largely affect the rover's positioning. To avoid such outliers, one can choose better solutions by comparing the IT results with several different references. Actually, the IT solutions are compared with the sea surface height model, with the assumption that the vessels are constrained on the sea surface (Fujita and Yabuki, 2003).

In the case of the SIO buoy, the lack of data between 6:00 and 7:00 (UTC) was considered to cause the step-wise discrepancy between GIPSY and RTKLIB, especially in eastern component. Although it seemed to be restored at 10:20–10:30 (UTC), this was likely caused by other reasons. Because we set RTKLIB to remove the GNSS data during the eclipse, only 4 satellites had been available during 10:20–10:25 (UTC), which might cause another step-wise offset. In addition, less than 4 satellites had been available at 20:41, when spiky noises were appeared in both results in Figure 3-7. However, the missing would not affect to the difference between GIPSY and PANDA. These facts indicated that GIPSY and PANDA provide the similar and robust PPP solutions for the missing data, though it does not necessarily mean the more accurate solutions.

Considering the results from all the datasets analyzed here, the PANDA PPP software with ambiguity resolution (PPP-AR) can provide more stable solution even in situations with loss of data, perhaps due to solving the integer ambiguity, which we did not for RTKLIB. It is noted for the differential positioning, which is a method to reduce the error using the

reference station, that the long-term biases of the reference positions also propagate directly to the rover's solution.

On the other hand, PPP-AR by PANDA requires the additional computational process to estimate the clocks and FCBs. In light of “routine” GNSS-A analysis where the convenience and simplicity for beginners have values, RTKLIB is a good candidate for positioning the vessels. For the purpose of GNSS-A observation, where one solves the static positions using acoustic ranging data from the estimated ship track with the period of about 10–20 hours, long-term variation, rather than short-term, would decrease the precision of the seafloor positioning. Although the PPP by RTKLIB might provide no more stable results than the PPP-AR by PANDA in short time scale, both software can provide the results with almost the same long-term stability. Therefore, RTKLIB is useful for the PPP analysis in the routine GNSS-A analysis.

3.3 Impacts of GNSS solutions on GNSS-A positions

3.3.1 Data and Methods

In this Section, we investigate the long-term stability of GNSS-A solutions by comparing the seafloor positions using the kinematic PPP solutions with the conventional baseline solutions. Additionally, we evaluate the stability of solutions using the rapid products, which have the latency of 17–41 hours, rather than the final products, which have the latency of 12–18 days. For example, the rapid solutions will be required for the urgent GNSS-A observations for the coseismic analysis, or for the data assimilation to seismic cycle models in the future. It should be noted that, as of 2020, the GNSS-A data cannot be analyzed on the survey vessels due to the limitation of data transfer so that the rapid products should be the best for the urgent analysis.

We used the following GNSS-A sites: ASZ2 with the larger water depth and baseline range, TOS1 with smaller water depth and baseline range, and MRT2 where the earlier data since 2008 is available (Table 3-5). GNSS data were continuously recorded at 2 Hz on the mast of the survey vessels during the GNSS-A observations. We processed the GNSS data with the post-processing kinematic PPP mode of RTKLIB version 2.4.2 (Takasu, 2013) applying the forward-backward smoothing.

For the PPP analysis, precise satellite orbit and clock data are required. According to Guo et al. (2010), who investigated the impact of sampling rate of clock products on 1 Hz GNSS data, the solutions with 5-min clock had approximately 30% larger standard deviations than

the solutions with 5-sec and 30-sec clock products. For this reason, we examined the 5-sec and 30-sec clock products, which are distributed via the internet by several organizations such as the International GNSS Service (IGS) and the Center for Orbit Determination in Europe (CODE).

Based on the availability of GNSS products, we processed the PPP analysis with following orbit/clock products: (1) IGS final orbits (International GNSS Service, a) and IGS final 30-sec clocks (International GNSS Service, b), (2) CODE final orbits and final 5-sec clocks (Dach et al., 2018), and (3) CODE rapid orbits and rapid 30-sec clocks (Dach et al., 2019). Because the CODE rapid 30-sec clocks before the mid-2015 are not published, we tested the product set (3) for the GNSS-A observations after 2016. Hereafter, we call the kinematic PPP solutions using the product sets (1), (2), and (3), PPP-Final.30s, PPP-Final.5s, and PPP-Rapid.30s solutions, respectively.

The conventional baseline solutions were derived by IT (e.g., Colombo, 1998) version 4.2 (hereafter, "baseline solution"). Since IT can handle up to three reference sites, better baseline solutions were deliberately selected for each campaign from the combinations of terrestrial sites.

For the purpose of investigating the stability of seafloor positioning, we discuss the differences in the time series of GNSS-A solutions derived from the different GNSS solutions. We used SGOBS version 3.6.3 (Fujita et al., 2006) for the GNSS-A analysis (see Chapter 4 for details of SGOBS), applying the same configuration as Yokota et al. (2018), except the GNSS processing.

3.3.2 Results

Time series of seafloor displacements by baseline and PPP-Final.30s solutions are shown in Figure 3-8. Because the baseline and PPP solutions are aligned to different reference frame, positional offset between the solutions was corrected to align the average positions. Figure 3-9 shows the distributions of differences between the seafloor positions by baseline and PPP-Final.30s solutions. The root mean square (RMS) values of horizontal and vertical position differences were 1–2 cm and 2.6 cm, respectively (Table 3-6). Yokota et al. (2018), who investigated the RMS values of residuals of the linear regression for the data after 2013 in the assumption where the seafloor moves at a constant rate, reported that the standard deviations of horizontal and vertical displacement were approximately 2 cm and 3 cm, respectively, which can be assumed as the reference precision of GNSS-A positioning. Hence, the differences between the baseline and PPP-Final.30s solutions were smaller than the reference precision

of GNSS-A positioning. In addition, linear trends of positional differences between the seafloor positional time series with baseline solution and PPP-Final.30s solution (Table 3-7) indicates that the GNSS-dependency on horizontal velocities was up to 4 mm/year at 95% confidence level. Since the trends of displacement has no significant bias errors, GNSS-A solutions with PPP show almost the same stability as baseline solutions.

Time series of seafloor displacements by three PPP solutions, i.e., PPP-Final.30s, PPP-Final.5s, and PPP-Rapid.30s solutions, are shown in Figure 3-10. Figure 3-10 displays the absolute positions in the ITRF. The RMS values of position differences of PPP-Final.5s and PPP-Rapid.30s with PPP-Final.30s (summarized in Table 3-7) were approximately 0.5 cm and 1 cm in the horizontal and vertical components, respectively. These are much smaller than the reference precision of GNSS-A positioning, which typically caused by the misestimation of sound speed variations.

3.3.3 Discussion

Seafloor displacements determined by using post-processing PPP solutions had almost the same variance as the conventional baseline solutions, which empirically confirmed the reproductivity of the deformation trends. However, it is difficult to quantitatively evaluate the accuracy of each solution, because the GNSS-A has larger error sources than the effects from the GNSS noise. For instance, because the GNSS-A solver estimates the sound speed variations, the GNSS perturbation with temporal scale similar to the sound speed model are possibly corrected as the sound speed perturbation. The random or short-scale GNSS noise should be sufficiently reduced by collecting thousands of acoustic data for the static GNSS-A analysis.

To consider the effect of bias errors of GNSS on GNSS-A solution, we compared the GNSS biases and GNSS-A discrepancies for the PPP-Final.30s and baseline solutions (Figure 3-11). These values are almost the same for all observation epochs. It indicates that the bias errors in GNSS cannot be reduced by the sound speed perturbation models, and that they directly affect to the GNSS-A solutions. Therefore, suppressing the bias errors in GNSS solutions is essentially important for the GNSS-A positioning.

Based on the results of Section 3.2, baseline solutions are directly affected by the errors in reference sites. PPP has an advantage in suppressing the biases of reference which depend on the deliberate selection of terrestrial sites. Additionally, in light of routine analysis operation, we can omit the process to determine the set of terrestrial reference sites in the procedure with PPP, which contributes to realizing more rapid and stable processing.

Whereas the procedures with PPP also have arbitrary for the selection of GNSS products such as the sampling rate of clocks, it did not cause the significant bias errors in GNSS-A solutions. Moreover, it was indicated that the rapid products can produce sufficiently reliable GNSS-A solution. This means that we can provide a sufficiently precise "rapid" GNSS-A solution a couple of days after the urgent observation. In the case of urgent GNSS-A, PPP has another advantage in data collection and robustness, unlike the baseline analysis where the high-rate terrestrial GNSS data and their fixed positions should be collected in advance.

3.4 Conclusions

We discussed the applicability of post-processing PPP instead of the conventional baseline analysis for the routine GNSS-A analysis in this Chapter. Because JCG has used a baseline analysis software IT to estimate the ship track for the routine analysis, the biases of 1–3 cm from the PPP (i.e., the global geodetic reference frame) would affect their results. The horizontal biases of terrestrial sites also varied in a range of about 1 cm with the campaign and the selection of the reference, which results in the long-term uncertainty of the ship track estimation. Although it is smaller than the GNSS-A horizontal error of 2–3 cm which is considered to be mainly caused by the temporal and spatial variations of the acoustic velocity (e.g., Sato et al., 2013b), it is possible that the stability of the time series of the seafloor positioning may improve when using the PPP results.

Taking the convenience, simplicity, and robustness for various operators into account, PPP analysis by RTKLIB is the best candidate for the routine GNSS-A operation. The results also indicate the availability of reliable "rapid" GNSS-A solutions with a latency of a few days. For the purpose of realizing more quick processing including semi-real time analysis for the urgent observation campaigns, in-situ GNSS processing should be performed on the survey vessels. If the "ultra-rapid" orbit and clock products, which consist of the observed half with a latency of 3 hours and the prediction half for next 24 hours, are available on the vessels, in-situ semi-real time GNSS-A analysis can be performed. The accuracy of "ultra-rapid" GNSS-A solutions should also be quantitatively evaluated before the implementation in the future. Simultaneously, the speed of each procedure, including GNSS analysis, correlation analysis for the acoustic data, and the GNSS-A positioning analysis, should be improved for the faster acquisition of seafloor displacement.

Table 3-1. Specifications of GNSS data used in Section 3.2 (modified from Watanabe et al., 2017).

Site name	Center pos. for local coords.	Data period [UTC]	Reference sites for IT (Approx. range)
TU12	38.02 °N 143.53 °E	(1) 2015/04/27 0500 –2015/04/27 2359 (2) 2015/08/07 1200 –2015/08/08 1159 (3) 2015/10/23 0100 –2015/10/23 2232	0036 (190 km), 0037 (230 km), 0172 (200 km), 0175 (200 km), 0179 (240 km), 0549 (210 km), 0550 (180 km), 0918 (200 km)
SAGA	34.96 °N 139.26 °E	(1) 2012/11/24 0200 –2012/11/24 2159	0759 (40 km), 3047 (50 km), 3048 (10 km), 3051 (20 km), 5105 (10 km)
HYG1	32.38 °N 132.42 °E	(1) 2015/05/29 2000 –2015/05/30 1124 (2) 2015/09/11 1200 –2015/09/12 0400 (3) 2015/12/12 0100 –2015/12/12 0950 (4) 2016/01/16 1000 –2016/01/17 0112 (5) 2016/03/19 2300 –2016/03/20 1505	0085 (70 km), 0094 (70 km), 1059 (40 km), 1080 (70 km), 1088 (110 km), 1126 (60 km)
HYG2	31.97 °N 132.49 °E	(1) 2015/05/28 1800 –2015/05/29 0240 (2) 2015/05/29 1000 –2015/05/29 2025 (3) 2015/09/12 0400 –2015/09/12 2359 (4) 2016/01/15 1500 –2016/01/16 0837	0085 (100 km), 0094 (100 km), 1059 (90 km), 1080 (120 km), 1088 (100 km), 1126 (90 km)
SIO buoy	33.21 °N 118.39 °W	2011/03/14 0000 –2011/03/14 2359 (no data b/w 0600–0700)	N/A

Table 3-2. Configurations for GNSS analysis software (modified from Watanabe et al., 2017).

Software	Mode	Sat. orbit	Sat. clock	FCB	Frame.
PANDA	PPP-AR	IGS Final	Estimate (30 sec.)	Estimate	ITRF2008
RTKLIB	PPP	IGS Final	IGS Final (30 sec.)	N/A	ITRF2008
IT	Differential	IGS Final	N/A	N/A	GEONET F3 (ITRF2005)

Table 3-3. Values of average and standard deviation of the position differences for GNSS-A sites between PANDA's solution and other solutions. The names of the reference site for IT are shown as IT_[site name]. The table is modified from Watanabe et al. (2017)

(a) TU12_2015/04/27

Comparison solution	Average (Bias) [m]			Standard deviation [m]		
	E-ward	N-ward	U-ward	E-ward	N-ward	U-ward
RTKLIB	-0.0030	0.0014	-0.0125	0.0128	0.0107	0.0380
IT_0036	0.0185	0.0198	0.0164	0.0113	0.0109	0.0428
IT_0037	0.0115	0.0027	0.0060	0.0087	0.0107	0.0416
IT_0172	0.0015	0.0173	-0.0186	0.0098	0.0131	0.0469
IT_0175	-0.0069	0.0144	0.0196	0.0465	0.0667	0.2895
IT_0179	0.0032	0.0146	-0.0127	0.0168	0.0153	0.0543
IT_0549	0.0107	0.0050	-0.0515	0.0104	0.0159	0.0617
IT_0550	0.0114	0.0084	-0.0089	0.0107	0.0136	0.0460
IT_0918	0.0098	0.0065	-0.0221	0.0074	0.0115	0.0412

(b) TU12_2015/08/07

Comparison solution	Average (Bias) [m]			Standard deviation [m]		
	E-ward	N-ward	U-ward	E-ward	N-ward	U-ward
RTKLIB	-0.0062	0.0035	0.0022	0.0138	0.0131	0.0734
IT_0036	0.0036	0.0231	-0.0040	0.0335	0.0255	0.0816
IT_0037	-0.0068	0.0071	-0.0127	0.0346	0.0249	0.0880
IT_0172	-0.0132	0.0308	-0.0543	0.0183	0.0219	0.0796
IT_0175	-0.0119	0.0201	-0.0384	0.0240	0.0226	0.0848
IT_0179	-0.0226	0.0126	-0.0228	0.0354	0.0304	0.0996
IT_0549	-0.0237	0.0061	-0.0288	0.0251	0.0252	0.0940
IT_0918	-0.0020	0.0117	-0.0386	0.0273	0.0231	0.0799

(c) TU12_2015/10/23

Comparison solution	Average (Bias) [m]			Standard deviation [m]		
	E-ward	N-ward	U-ward	E-ward	N-ward	U-ward
RTKLIB	-0.0028	0.0026	-0.0210	0.0157	0.0134	0.0491
IT_0036	0.0111	0.0201	0.0037	0.0116	0.0147	0.0693
IT_0037	0.0103	0.0067	-0.0043	0.0090	0.0140	0.0638
IT_0172	0.0024	0.0198	-0.0400	0.0115	0.0127	0.0581
IT_0175	0.0067	0.0164	-0.0356	0.0101	0.0116	0.0544
IT_0179	0.0039	0.0139	-0.0079	0.0138	0.0168	0.0585
IT_0549	-0.0032	0.0094	-0.0416	0.0159	0.0144	0.0697
IT_0550	0.0075	0.0092	-0.0214	0.0104	0.0113	0.0542
IT_0918	0.0076	0.0091	-0.0369	0.0107	0.0133	0.0624

(d) SAGA_2012/11/24

Comparison solution	Average (Bias) [m]			Standard deviation [m]		
	E-ward	N-ward	U-ward	E-ward	N-ward	U-ward
RTKLIB	0.0052	0.0000	-0.0020	0.0093	0.0066	0.0289
IT_0759	0.0104	0.0126	-0.0519	0.0173	0.0124	0.0584
IT_3047	0.0187	0.0026	-0.0139	0.0161	0.0160	0.0407
IT_3048	0.0142	0.0102	-0.0274	0.0077	0.0096	0.0382
IT_3051	0.0143	0.0140	-0.0057	0.0084	0.0101	0.0299
IT_5105	0.0113	0.0138	-0.0319	0.0095	0.0107	0.0417

(e) HYG1_2015/05/29

Comparison solution	Average (Bias) [m]			Standard deviation [m]		
	E-ward	N-ward	U-ward	E-ward	N-ward	U-ward
RTKLIB	0.0019	-0.0011	-0.0224	0.0117	0.0110	0.0924
IT_0085	0.0179	0.0165	-0.0448	0.0104	0.0114	0.0939
IT_0094	0.0057	0.0079	-0.0250	0.0239	0.0238	0.1208
IT_1059	0.0158	0.0100	-0.0702	0.0112	0.0136	0.0939
IT_1080	-0.0013	0.0148	-0.0771	0.0124	0.0170	0.0897
IT_1088	0.0029	0.0161	-0.0643	0.0178	0.0190	0.0959
IT_1126	0.0075	0.0151	-0.0453	0.0129	0.0123	0.0985

(f) HYG1_2015/09/11

Comparison solution	Average (Bias) [m]			Standard deviation [m]		
	E-ward	N-ward	U-ward	E-ward	N-ward	U-ward
RTKLIB	0.0012	0.0032	-0.0026	0.0110	0.0085	0.0579
IT_0085	0.0218	0.0155	-0.0176	0.0099	0.0116	0.0608
IT_0094	0.0128	0.0068	0.0032	0.0207	0.0159	0.0614
IT_1059	0.0137	0.0139	-0.0572	0.0147	0.0138	0.0539
IT_1080	0.0074	0.0147	-0.0610	0.0117	0.0146	0.0664
IT_1088	0.0140	0.0136	-0.0348	0.0102	0.0119	0.0539
IT_1126	0.0153	0.0151	-0.0186	0.0123	0.0130	0.0658

(g) HYG1_2015/12/12

Comparison solution	Average (Bias) [m]			Standard deviation [m]		
	E-ward	N-ward	U-ward	E-ward	N-ward	U-ward
RTKLIB	0.0020	0.0016	-0.0151	0.0142	0.0089	0.0480
IT_0085	0.0183	0.0205	-0.0182	0.0098	0.0105	0.0624
IT_0094	0.0180	0.0106	0.0328	0.0146	0.0144	0.1277
IT_1059	0.0160	0.0166	-0.0307	0.0180	0.0159	0.0808
IT_1080	0.0164	0.0077	0.0128	0.0164	0.0189	0.0678
IT_1088	0.0144	0.0250	-0.0300	0.0086	0.0124	0.0598
IT_1126	0.0102	0.0203	-0.0383	0.0101	0.0112	0.0596

(h) HYG1_2016/01/16

Comparison solution	Average (Bias) [m]			Standard deviation [m]		
	E-ward	N-ward	U-ward	E-ward	N-ward	U-ward
RTKLIB	-0.0102	-0.0026	0.0178	0.0080	0.0169	0.0746
IT_0085	0.0030	0.0158	-0.0361	0.0193	0.0108	0.0820
IT_0094	0.0121	0.0092	-0.0255	0.0212	0.0165	0.1038
IT_1059	-0.0010	0.0128	-0.0480	0.0210	0.0147	0.0813
IT_1080	0.0237	0.0044	-0.0662	0.0468	0.0185	0.1032
IT_1088	0.0026	0.0219	-0.0521	0.0184	0.0115	0.0790
IT_1126	-0.0033	0.0142	-0.0497	0.0187	0.0124	0.0747

(i) HYG1_2016/03/19

Comparison solution	Average (Bias) [m]			Standard deviation [m]		
	E-ward	N-ward	U-ward	E-ward	N-ward	U-ward
RTKLIB	-0.0049	0.0005	0.0027	0.0185	0.0152	0.0995
IT_0085	0.0170	0.0211	-0.0423	0.0161	0.0157	0.0958
IT_0094	0.0164	0.0149	-0.0116	0.0137	0.0142	0.0907
IT_1059	0.0093	0.0163	-0.0542	0.0123	0.0170	0.0931
IT_1080	0.0031	0.0108	-0.0627	0.0218	0.0193	0.1054
IT_1088	0.0136	0.0288	-0.0433	0.0082	0.0134	0.0899
IT_1126	0.0004	0.0164	-0.0561	0.0143	0.0177	0.1007

(j) HYG2_2015/05/28

Comparison solution	Average (Bias) [m]			Standard deviation [m]		
	E-ward	N-ward	U-ward	E-ward	N-ward	U-ward
RTKLIB	-0.0016	0.0033	-0.0057	0.0097	0.0101	0.0452
IT_0085	0.0250	0.0239	-0.0550	0.0131	0.0134	0.0569
IT_0094	0.0149	0.0122	-0.0170	0.0114	0.0146	0.0686
IT_1059	0.0156	0.0169	-0.0830	0.0148	0.0158	0.0716
IT_1080	0.0099	0.0136	-0.0689	0.0106	0.0155	0.0556
IT_1088	-0.0015	0.0224	-0.0522	0.0135	0.0126	0.0545
IT_1126	0.0101	0.0231	-0.0560	0.0114	0.0151	0.0531

(k) HYG2_2015/05/29

Comparison solution	Average (Bias) [m]			Standard deviation [m]		
	E-ward	N-ward	U-ward	E-ward	N-ward	U-ward
RTKLIB	0.0054	0.0007	-0.0054	0.0114	0.0117	0.0549
IT_0085	0.0203	0.0229	-0.0243	0.0156	0.0116	0.0617
IT_0094	0.0115	0.0137	0.0013	0.0130	0.0148	0.0693
IT_1059	0.0172	0.0170	-0.0308	0.0155	0.0125	0.0533
IT_1080	0.0036	0.0118	-0.0619	0.0196	0.0159	0.0705
IT_1088	0.0099	0.0181	-0.0405	0.0120	0.0143	0.0522
IT_1126	0.0174	0.0199	-0.0217	0.0192	0.0123	0.0634

(l) HYG2_2015/09/12

Comparison solution	Average (Bias) [m]			Standard deviation [m]		
	E-ward	N-ward	U-ward	E-ward	N-ward	U-ward
RTKLIB	-0.0044	-0.0041	-0.0056	0.0207	0.0232	0.0896
IT_0085	0.0200	0.0256	-0.0113	0.0127	0.0166	0.0810
IT_0094	0.0084	0.0104	0.0050	0.0172	0.0222	0.0990
IT_1059	0.0210	0.0174	-0.0394	0.0195	0.0224	0.0867
IT_1080	0.0106	0.0195	-0.0609	0.0171	0.0195	0.0924
IT_1088	0.0045	0.0187	-0.0299	0.0179	0.0226	0.0793
IT_1126	0.0155	0.0214	-0.0221	0.0172	0.0226	0.1080

(m) HYG2_2016/01/15

Comparison solution	Average (Bias) [m]			Standard deviation [m]		
	E-ward	N-ward	U-ward	E-ward	N-ward	U-ward
RTKLIB	0.0132	-0.0006	-0.0166	0.0162	0.0141	0.0836
IT_0085	0.0218	0.0180	-0.0241	0.0131	0.0165	0.0790
IT_0094	0.0257	0.0120	-0.0072	0.0130	0.0176	0.0786
IT_1059	0.0194	0.0133	-0.0361	0.0129	0.0166	0.0793
IT_1080	0.0162	0.0056	-0.0525	0.0142	0.0242	0.0848
IT_1088	0.0161	0.0223	-0.0493	0.0129	0.0150	0.0841
IT_1126	0.0139	0.0157	-0.0563	0.0183	0.0190	0.0849

Table 3-4. Values of average and standard deviation of the position differences for SIO buoy between GIPSY's solution and other solutions (modified from Watanabe et al., 2017).

Comparison solution	Average (Bias) [m]			Standard deviation [m]		
	E-ward	N-ward	U-ward	E-ward	N-ward	U-ward
PANDA	0.0014	0.0038	0.0167	0.0042	0.0063	0.0227
RTKLIB	-0.0088	0.0093	0.0077	0.0223	0.0150	0.0499

Table 3-5. Locations and observation periods for GNSS-A observation site used in Section 3.3 (after Watanabe et al., 2020d).

GNSS-A site name	Latitude [°N]	Longitude [°E]	Height [m]	Observation period [MM/DD/YYYY]	Number of epochs
ASZ2	31.9294	133.5756	-2942	01/30/2012 – 11/11/2019	33
TOS1	32.8170	133.6671	-996	01/27/2012 – 11/21/2019	30
MRT2	32.8717	134.8163	-1404	09/15/2008 – 11/23/2019	43

Table 3-6. Root mean square (RMS) values of positional difference with respect to PPP-Final.30s solution. Only in the case of baseline solution, averages of positional differences are corrected. The table is modified from Watanabe et al. (2020d).

GNSS solution type	Eastward	Northward	Upward
Baseline solution by IT	1.3 cm	0.9 cm	2.6 cm
PPP-Final.5s solution by RTKLIB	0.5 cm	0.4 cm	0.9 cm
PPP-Rapid.30s solution by RTKLIB	0.5 cm	0.4 cm	1.3 cm

Table 3-7. Linear trends of positional differences between the GNSS-A seafloor positional time series with baseline solution and PPP-Final.30s solution (after Watanabe et al., 2020d).

GNSS-A site name	Eastward [cm/year] with 95% CL	Northward [cm/year] with 95% CL	Upward [cm/year] with 95% CL
ASZ2	0.17 +/– 0.21	0.07 +/– 0.20	-0.43 +/– 0.48
TOS1	0.03 +/– 0.26	0.17 +/– 0.12	-0.17 +/– 0.32
MRT2	0.15 +/– 0.11	0.11 +/– 0.06	-0.33 +/– 0.24

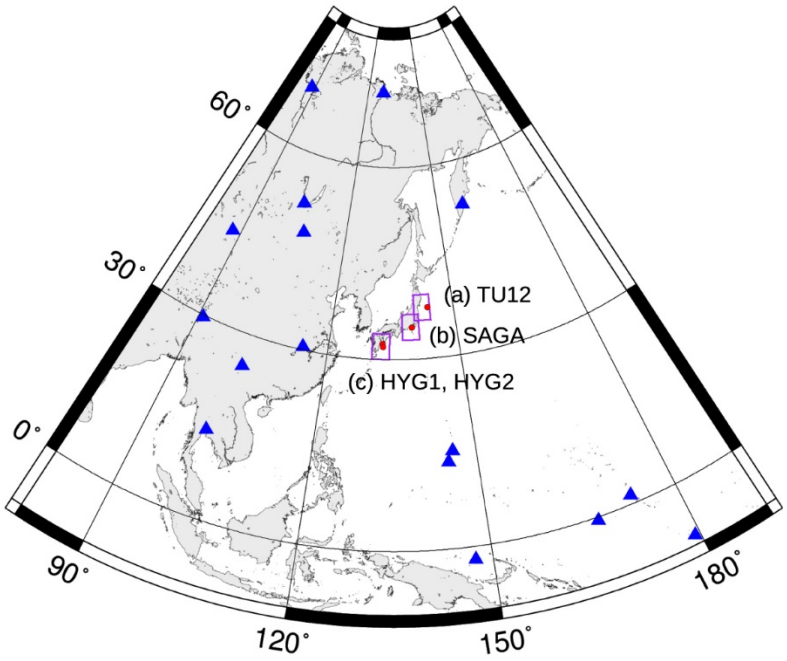

Figure 3-1. Locations of the GNSS-A sites where the rover's data in this study were collected (red circles). Blue triangles indicate the locations of the IGS stations used for the network solution in PANDA. Purple rectangular areas are enlarged in Figure 3-2. The figure is adapted from Watanabe et al. (2017).

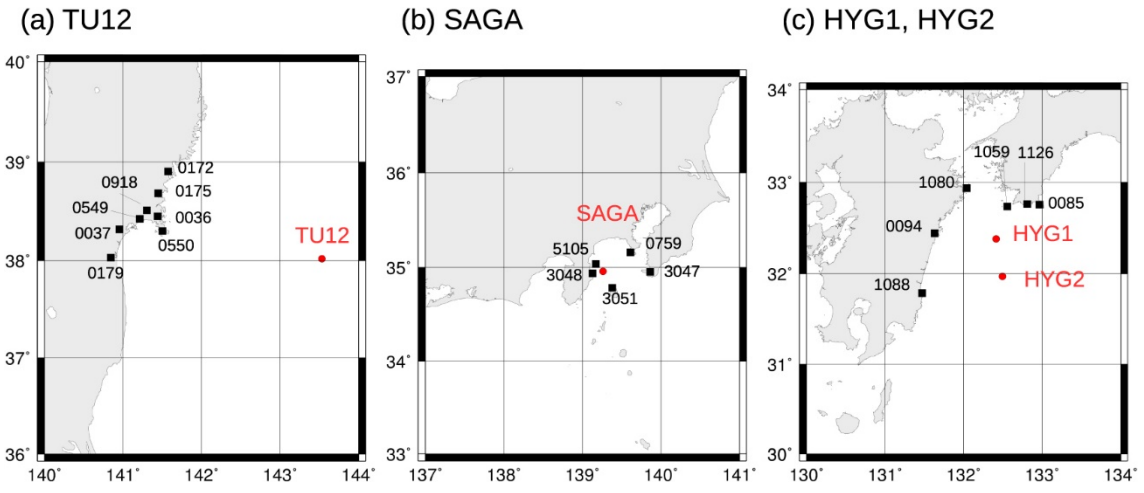

Figure 3-2. Locations of the GNSS-A sites where the rover's data in this study were collected (red circles) and the terrestrial reference sites for the differential positioning in IT (black squares) for (a) TU12, (b) SAGA, and (c) HYG1 and HYG2. The figure is adapted from Watanabe et al. (2017).

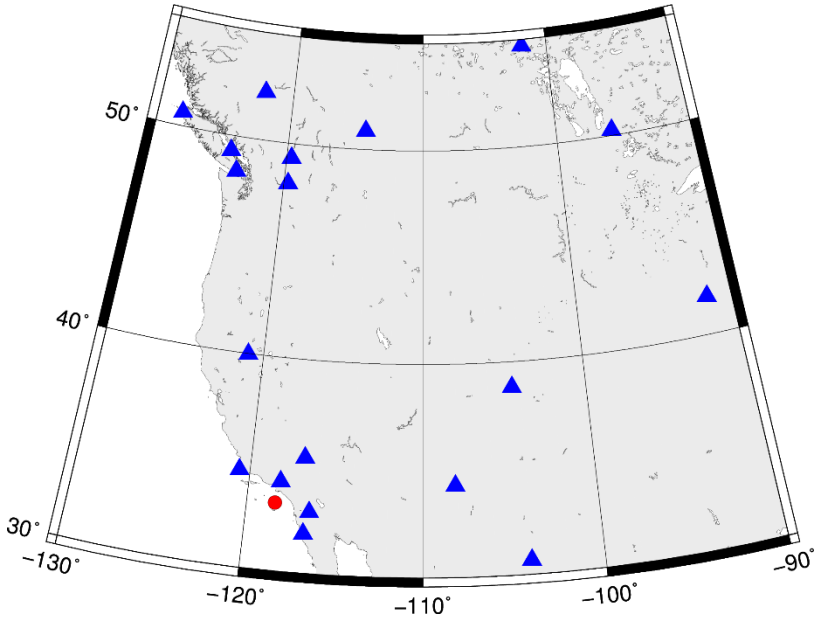

Figure 3-3. Location of the SIO buoy where the GNSS data was collected (red circle). Blue triangles indicate the locations of the IGS stations used for the network solution in PANDA. The figure is adapted from Watanabe et al. (2017).

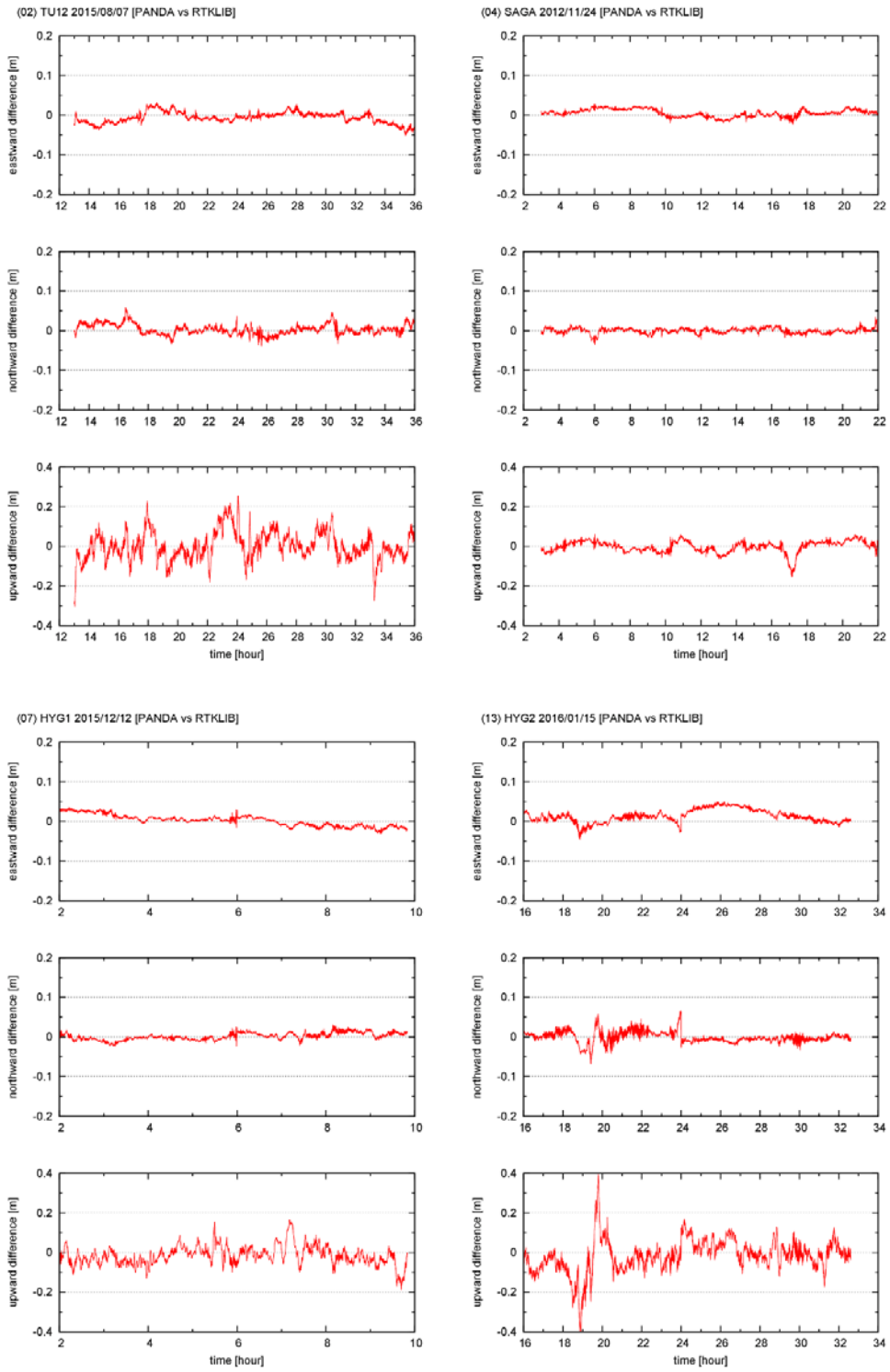

Figure 3-4. Examples for time series of position differences between the results by PANDA and RTKLIB in the local ENU coordinates. Eastern, northern, and vertical components are displayed on top, middle, and bottom panels, respectively. The figure is adapted from Watanabe et al. (2017).

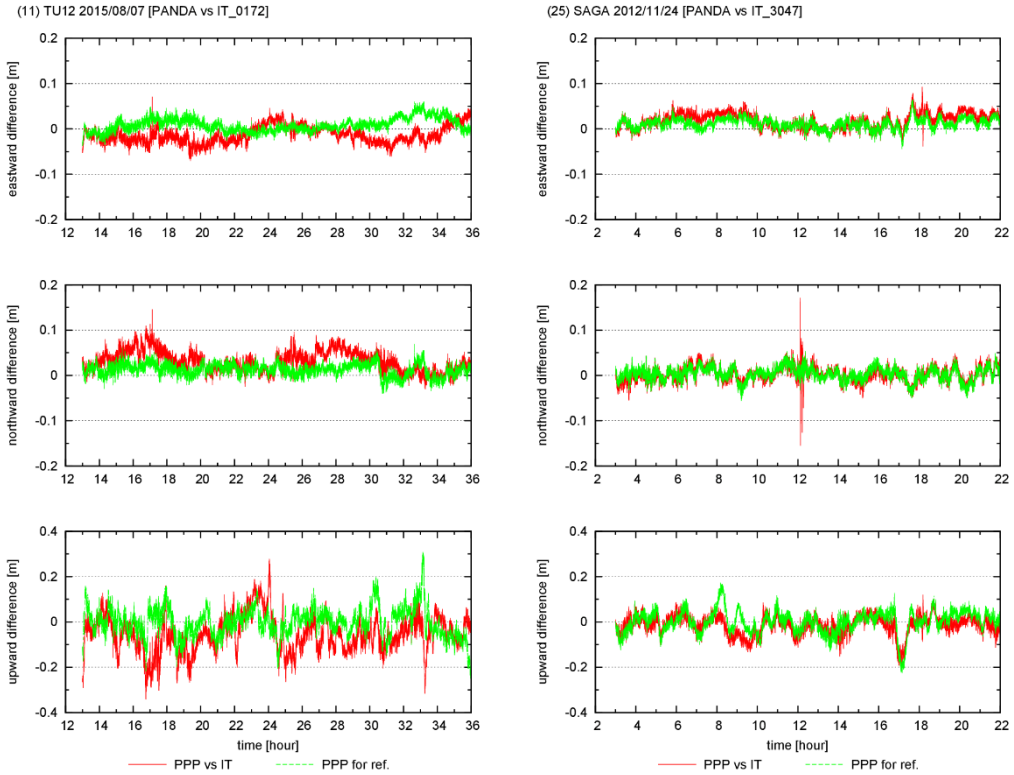
(11) TU12 2015/08/07 [PANDA vs IT_0172]
(25) SAGA 2012/11/24 [PANDA vs IT_3047]
eastward difference [m]
northward difference [m]
upward difference [m]
time [hour]
PPP vs IT
PPP for ref.

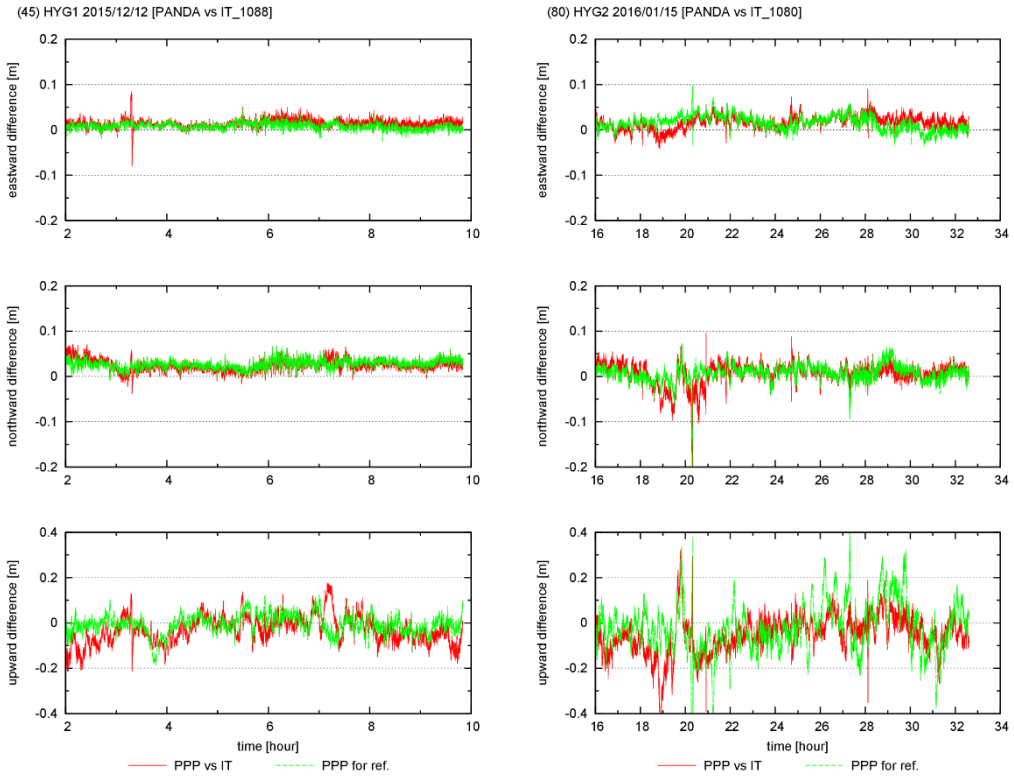
(45) HYG1 2015/12/12 [PANDA vs IT_1088]
(80) HYG2 2016/01/15 [PANDA vs IT_1080]
eastward difference [m]
northward difference [m]
upward difference [m]
time [hour]
PPP vs IT
PPP for ref.

Figure 3-5. Examples for time series of position differences between the results by PANDA and IT in the local ENU coordinates (red lines). The names of the reference site for IT are shown on the title as IT_[site name]. Eeastern, northern, and vertical components are displayed on top, middle, and bottom panels, respectively. Green lines indicate the pseudo-kinematic solution of the reference solved by PANDA, relative to the fixed position used in IT. The figure is adapted from Watanabe et al. (2017).

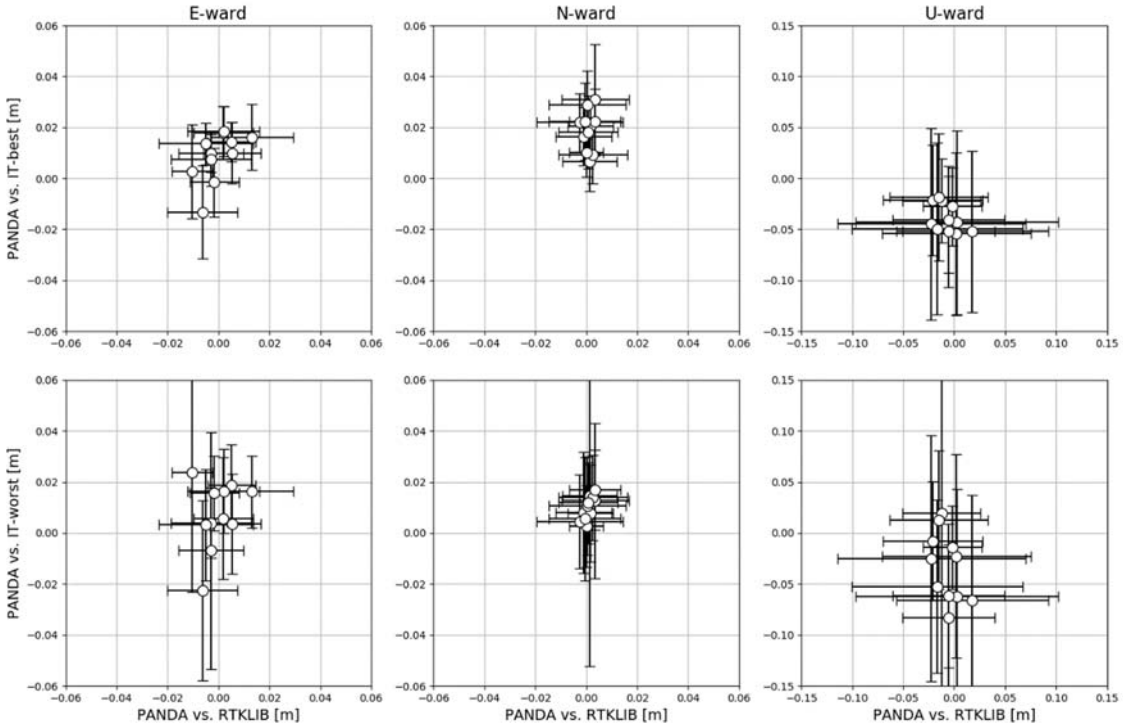

Figure 3-6. Summary of position differences between PANDA–RTKLIB and PANDA–IT solutions. Upper and lower panels show the results of IT with minimum and maximum horizontal standard deviations in tested baseline solutions for each observation epoch, respectively. Error bars indicate the value of standard deviations (1σ).

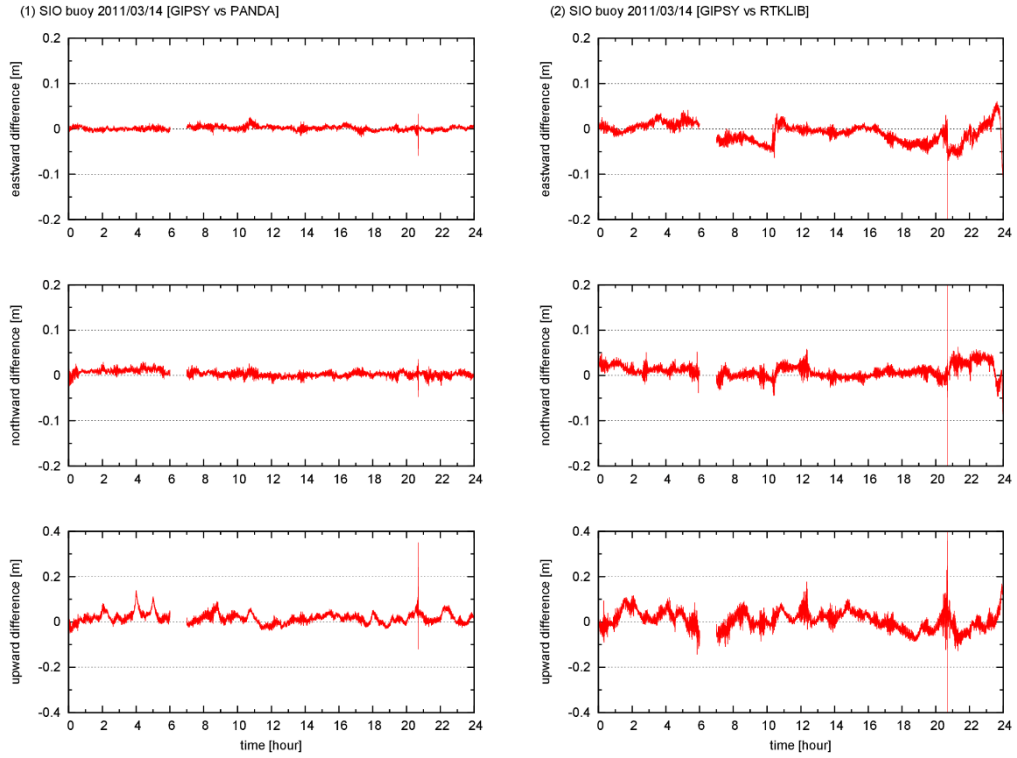

Figure 3-7. Time series of position differences of the SIO buoy between the results by (1) GIPSY and PANDA, and (2) GIPSY and RTKLIB in the local ENU coordinates. The eastern, northern, and vertical components are displayed on the top, middle, and bottom panels, respectively. The figure is adapted from Watanabe et al. (2017).

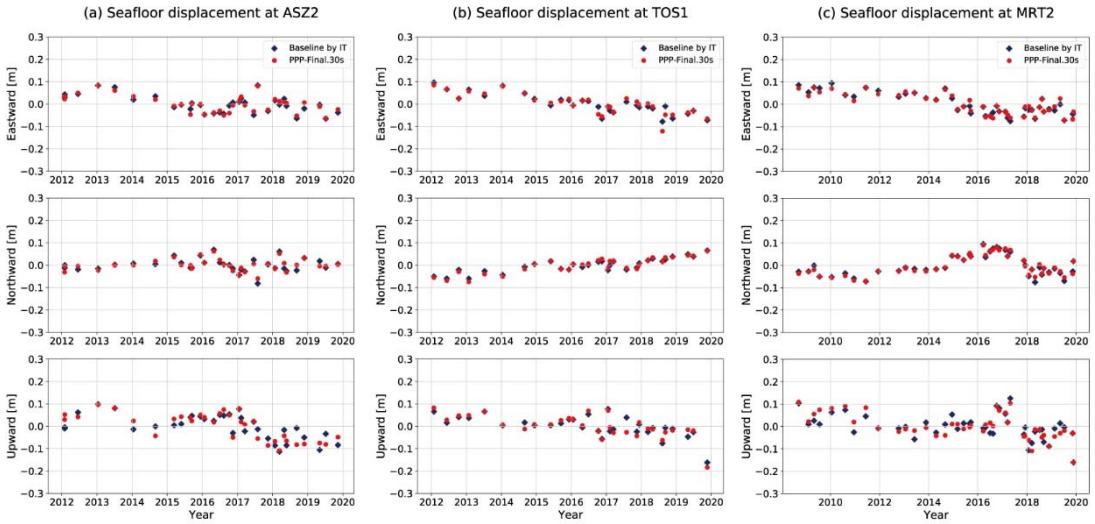

Figure 3-8. Time series of displacements at (a) ASZ2, (b) TOS1, and (c) MRT2 GNSS-A sites. Blue squares and red circles indicate the GNSS-A seafloor positions determined by using baseline solution by IT and PPP-Final.30s solution by RTKLIB, respectively. Averages of positional differences were corrected. The figure is adapted from Watanabe et al. (2020d).

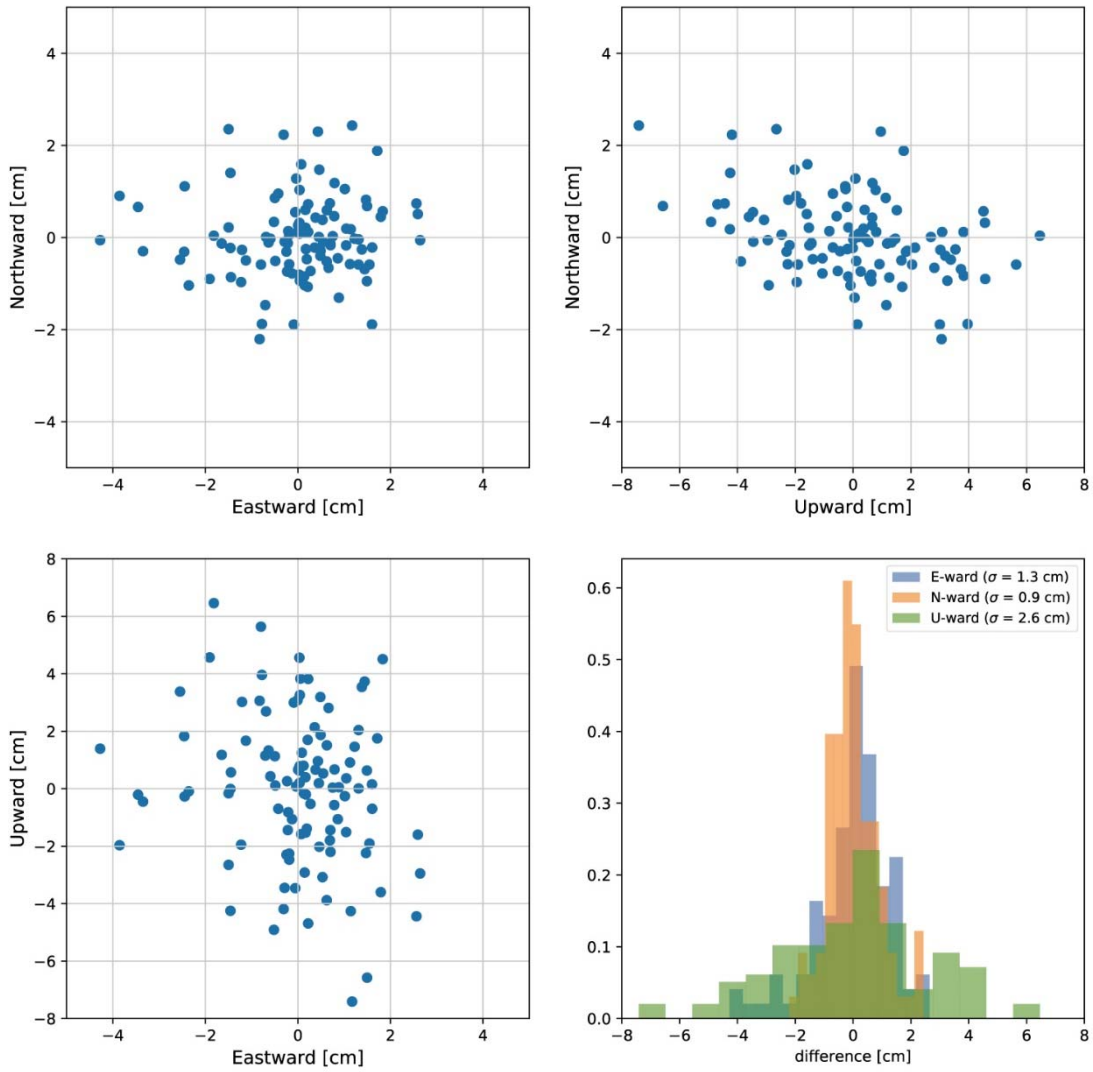

Figure 3-9. Distributions of differences between the GNSS-A seafloor positions determined by using baseline solution and PPP-Final.30s solution for northward-eastward (top-left), northward-upward (top-right), and upward-eastward (bottom-left) components. Histograms of eastward (blue), northward (orange), and upward differences (green) are shown in the bottom-right panel. The figure is adapted from Watanabe et al. (2020d).

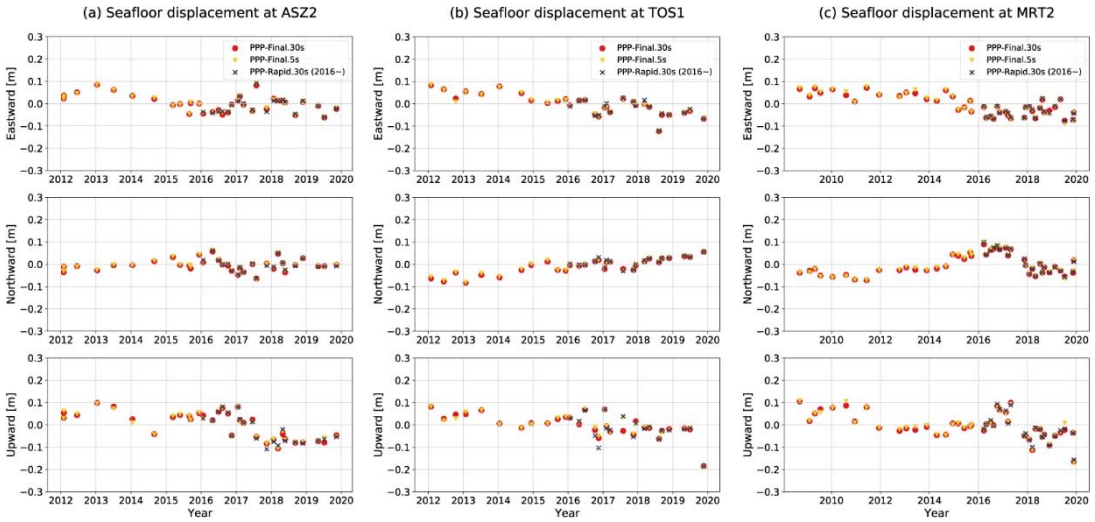

Figure 3-10. Time series of displacements at (a) ASZ2, (b) TOS1, and (c) MRT2 GNSS-A sites. Red circles, yellow triangles and navy crosses indicate the GNSS-A seafloor positions determined by using PPP-Final.30s solution, PPP-Final.5s solution, and PPP-Rapid.30s solution, respectively. In case of PPP-Rapid.30s, only the displacements after 2016 are shown. Displacements are calculated on the same reference frame. The figure is adapted from Watanabe et al. (2020d).

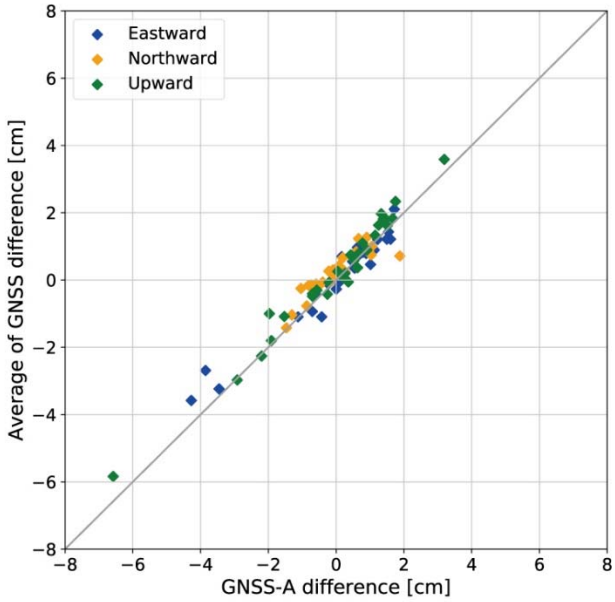

Figure 3-11. Scatter diagram of the differences between the GNSS-A seafloor positions determined by using PPP-Final.30s solution and baseline solution (horizontal axis), and the averages of differences between PPP-Final.30s solution and baseline solution of the survey vessel GNSS during each observation epoch (vertical axis). Blue, orange and green squares indicate eastward, northward and upward components, respectively. The figure is adapted from Watanabe et al. (2020d).

Chapter 4

Development of GNSS-A analysis tool "GARPOS"

Sections 4.2 and 4.4 in this Chapter references the author's work published as Watanabe et al. (2020c).

Reference:

Watanabe, S., Ishikawa, T., Yokota, Y., and Nakamura, Y. (2020c) GARPOS: Analysis Software for the GNSS - A seafloor positioning with simultaneous estimation of sound speed structure. *Front. Earth Sci.*, **8**, 597532. doi:10.3389/feart.2020.597532

4.1 Background

In the Japan Coast Guard, the GNSS-A analysis software "SGOBS" created by Fujita et al. (2006) had been used for the GNSS-A positioning analysis. SGOBS was originally written in FORTRAN 77, which had been upgraded by the members of GNSS-A analysis team. As of 2020, the SGOBS version 3.6 series is used in the routine analysis. The multi-epoch analysis applying the rigid-array constraint has been implemented in this version. Yokota et al. (2019) experimentally developed the SGOBS version 4 series to improve the positioning accuracy, where the transponder-dependent sound speed variations can be corrected in the end of the analysis. Although SGOBS version 4 is written in Fortran 90/95, it was almost a literal translation from FORTRAN 77.

However, the FORTRAN-based SGOBS had difficulties in extensibility and efficiency to conduct the routine analysis as the data accumulated. In the stage of the first development of

SGOBS, the GNSS-A observation was performed with the drifting configuration using the pole-system (see Ishikawa et al., 2020 for detail). For this reason, the input/output data format and the temporal expressions for sound speed variation were adapted for the drifting configuration rather than the sailing configuration. Furthermore, the multi-epoch analysis required larger memory capacity, where the larger float array should be prepared beforehand. It became also difficult to modify the original FORTRAN code because many staffs had contributed to the update and increased the number of ad hoc variables and parameters.

Accordingly, the author created a Python-based analysis software "GARPOS" from scratch to overcome the difficulties seen in the previous code. In this code, the analytical procedure shown in Chapter 2 is implemented. This Chapter shows the features of newly developed code and demonstrates the performance in applying to the actual data.

4.2 Features of GARPOS

GARPOS (an open beta version 0.1.0 was published as Watanabe et al., 2020a which is available at https://doi.org/10.5281/zenodo.3992688; the latest version 1.0.0 was published as Watanabe et al., 2021e which is available at https://doi.org/10.5281/zenodo.4522027) has been developed as an open source software to implement the GNSS-A analysis procedure. GARPOS is compatible with Python 3, with other packages NumPy, SciPy, pandas, and matplotlib. These packages are pre-installed in most of the Python distributions such as Anaconda. Sample scripts and data for testing GARPOS are also stored in the repository.

GARPOS is distributed as a series of files, which requires a driver script to run. The toolset consists of multiple Python files and a Fortran90 library for acsoutic ray tracing calculation. GARPOS requires the following input files:

(I-1) Initial site parameter file (in Python's configuration format),

(I-2) Acoustic observation data file (in csv format),

(I-3) Reference sound speed data file (in csv format),

(I-4) Setting file (in Python's configuration format).

Initial site parameter file (I-1) contains the initial values of the transponders' positions, the ATD offset and the relevant prior covariance information, as well as the metadata for the observation site and conditions. Acoustic observation data file (I-2) contains the list of the observation data associated with each acoustic ranging, such as travel time, positions, attitude

and other metadata. Reference sound speed data file (I-3) contains the reference sound speed profile approximated into a polygonal curve. Setting file (I-4) contains the parameters to control the analysis procedures including the hyper parameters. Users can put the lists of candidates of hyperparameters in which the best combination may be within. The parameters $nmp0$, $nmp1$, and $nmp2$ in the setting file control the number of basis functions, $K^{(\cdot)}$ in eq. (2.5).

The results are written in the following output files:

(O-1) Estimated site parameter files (in Python's configuration format),

(O-2) Modified acoustic observation data file (in csv format),

(O-3) Model parameter list file (in csv format),

(O-4) Posterior variance-covariance matrix file (in csv format).

Estimated site parameter files (O-1) is written in the same format as the file (I-1). Modified acoustic observation data file (O-2) contains the calculated travel time data and the coefficients of sound speed perturbation model, as well as the original data/metadata set in (I-2). Model parameter list file (O-3) and posterior variance-covariance matrix file (O-4) contain the whole estimated model parameter vector and its variance-covariance, respectively. Major input/output parmeters and hyperparameters for GARPOS are listed in Tables 4-1 and 4-2, respectively. Examples for the site parameter file (I-1/O-1) and observation data file (I-2/O-2) are shown in Figures 4-1 and 4-2, respectively.

We developed GARPOS to be compatible with both observation configurations, i.e., the move-around and stationary configurations, including the drifting observations. When handling the GNSS-A data collected in the stationary configurations or the ill-distributed move-around configurations, we should process data with some constraints on model parameters. Specifically, (1) upward components of transponders' positions should be fixed to zero, and (2) spatial gradient components of the sound speed perturbation model should not be solved, i.e., $nmp1 = nmp2 = 0$, because these parameters cannot be well resolved in the stationary configuration. Although further parameter tuning may be required for optimization, users can solve the seafloor position by GARPOS with the stationary data in addition to the move-around data.

4.3 Major changes from the conventional software

The largest difference in analytical procedures between GARPOS and SGOBS is the iterative method to estimate the model parameters. Whereas GARPOS estimates all the model parameters at once based on the posterior pdf defined in eq. (2.25), SGOBS took a step-by-step approach to extract the transponders' positions and sound speed perturbations. SGOBS solves the transponders' positions with constraining the sound speed coefficients in the first step, then estimates the sound speed coefficients with constraining the transponders' positions determined in the previous step. The iterations of two estimation steps continues until the convergence criteria are satisfied. This enabled us to stably obtain a reasonable sound speed variation without assuming the smoothness of temporal derivatives, such as defined in eq. (2.20).

The sound speed perturbation model used in SGOBS version 3 is comparable with the case where $\boldsymbol{\alpha}_1 = \boldsymbol{\alpha}_2 = \mathbf{0}$ in eq. (2.4). It is also understood that the basis functions $\Phi_k^{\langle 0 \rangle}$ are assumed as the group of independent piecewise polynomials. The transponder-dependent term, $\boldsymbol{\alpha}_2$, is taken into account in SGOBS version 4. When the sound speed perturbation has transponder-dependent component, systematic biases should appear in the travel time residuals even after processing by SGOBS version 3. SGOBS version 4 analyzes the residuals to extract one-directionally inclined sound speed structure (e.g., Yokota et al., 2019). Hence, all SGOBS versions are characterized by the stepwise approach, when compared with GARPOS.

4.4 Applications to the actual data

In this Section, we apply GARPOS to the actual GNSS-A data obtained at two sites with different oceanographic settings.

4.4.1 Data and settings

To verify the proposed analytical procedure, we reanalyzed the GNSS-A data at the sites named "TOS2" and "MYGI" (Table 4-3, Figure 4-3) in 2011-2019. The test sites were selected for several reasons: (1) whereas TOS2 is expected to move at almost constant rate, MYGI will show the transient displacement due to the postseismic crustal deformation of the 2011 Tohoku-oki earthquake; (2) the oceanographic environments are different, i.e., the effect of the Kuroshio current is dominant at TOS2; but (3) the depths of both sites are almost the same. The observation epochs used in this study is listed in Supplementary Tables 1 and 2 of Watanabe et al. (2020c). The datasets used in the performance tests are available at

https://doi.org/10.5281/zenodo.3993912 (Watanabe et al., 2020b).

Acoustic round-trip travel times were measured on the survey vessel using the hull-mounted acoustic transducer (e.g., Ishikawa et al., 2020). Processing delays in the acoustic devices were subtracted from the acoustic data beforehand.

Solid-earth-tide-free positions of GNSS antenna $\boldsymbol{Q}(t)$ were determined at 2 Hz by the open source software RTKLIB version 2.4.2 (Takasu, 2013) in post-processing kinematic Precise Point Positioning (PPP) mode, using the precise satellite orbit and the 30-sec satellite clock solutions (final products) provided by the International GNSS Service (International GNSS Service, a; b), in the same procedures as Watanabe et al. (2020d). The ATD offset values for each vessel, $\boldsymbol{M}$, were measured by leveling, distance, and angle surveys before the first GNSS-A observation cruise, to be used as $\boldsymbol{M}^0$.

Along with the acoustic observations, the profiles of temperature and/or conductivity were measured by CTD, XCTD or XBT probes several times. The reference sound speed profile, $V_0(u)$, was calculated from the observed temperature and salinity profiles using the empirical relationship proposed by Del Grosso (1974). To save the computational cost for ray tracing, the profile was approximated into a polygonal curve with several tens of nodes (Figure 4-4).

During a GNSS-A survey, the vessel sails on a pre-determined track over the seafloor transponder array to collect geometrically balanced acoustic data (e.g., Figure 1-1). The along-track observation (called "subset", hereafter) is repeated several times by reversing the sailing direction to reduce the bias due to the errors in the ATD offset.

During an observation cruise, it occasionally took more than a few weeks to collect sufficient acoustic data at a single site due to weather conditions or other operational restrictions. Even so, we compiled a single dataset per site per cruise for the static seafloor positioning in practice, because the positional changes should be too small to detect. We call the collection of a single GNSS-A dataset "observation epoch" or "epoch", hereafter.

We set the parameters for the numbers of basis functions, $K^{\langle\cdot\rangle}$, in eq. (2.5), as $nmp0 = nmp1 = nmp2 = 15$ for both preprocess and main process. Knot intervals of B-spline basis functions were approximately 10-20 min. for most epochs.

4.4.2 Array geometry determination

To calculate the proper array geometry $\overline{\boldsymbol{X}_j}$ in eq. (2.7) for the rigid-array constraint, we first determined the positions of each transponder for all observations. Note that not all

transponders are used in each observation, for example, because of additional installation of transponders for replacing transponders which were decommissioned due to battery outage. $\overline{\boldsymbol{X}_j}$ and the positional difference of the array center for nth observation, $\boldsymbol{c}^{(n)}$ were calculated by solving the following simultaneous equations:

$$\begin{cases} \boldsymbol{X}_j^{(n)} = \delta_j^{(n)}\overline{\boldsymbol{X}_J} + \delta_j^{(n)}\boldsymbol{c}^{(n)} & (\text{for } j = 1 \dots J \text{ and } n = 1 \dots N) \\ 0 \quad = \sum_{n=1}^{N} \boldsymbol{c}^{(n)} \end{cases}, \tag{4.1}$$

with,

$$\delta_j^{(n)} = \begin{cases} 1 & \text{if the transponder } j \text{ is used in } n \text{ th observation} \\ 0 & \text{others} \end{cases},$$

where J and N are the number of transponders and observations, respectively, and $\boldsymbol{X}_j^{(n)}$ denotes the predetermined transponders' positions for the nth observation.

The preliminary array-free positioning was also used for the verification of the collected data. We eliminated the outliers whose discrepancies from the preliminary solution were larger than the arbitrary threshold. We set the threshold to be 5 times as large as the root mean square value (RMS) of the travel time residuals.

4.4.3 Hyperparameter search

To get the solution $\boldsymbol{x}^*$, we should determine the appropriate values for the various hyperparameters, i.e., σ^2, μ_t, μ_{MT}, ρ^2, ${\lambda_0}^2$, ${\lambda_{1E}}^2$, ${\lambda_{1N}}^2$, ${\lambda_{2E}}^2$, and ${\lambda_{2N}}^2$. In the scheme of the ABIC minimization, σ^2 can be determined analytically by eq. (2.33). It is reasonable to assume ${\lambda_{1E}}^2 = {\lambda_{1N}}^2 = {\lambda_{2E}}^2 = {\lambda_{2N}}^2$ because these hyperparameters control the smoothness of the spatial sound speed structure. We hereafter use a variable ${\lambda_g}^2$ to represent the value of these hyperparameters. For the purpose of single positioning, ρ should be a large number, for example in meter-order. The large ρ hardly changes the ABIC value and thus the solution.

To save the computational resources, we should further reduce the number of hyperparameters. We tentatively put $\mu_{MT} = 0.5$. For the sound speed variations, we had to assume the strong constancy of spatial sound speed structure to resolve them with the single transducer GNSS-A. For this reason, we selected the ratio of ${\lambda_0}^2$ and ${\lambda_g}^2$, as ${\lambda_g}^2 = 0.1\,{\lambda_0}^2$. The last two hyperparameters, μ_t and ${\lambda_0}^2$, were determined with the grid search method. The tested values for μ_t and ${\lambda_0}^2$ are $\mu_t = (0\text{ min.}, 0.5\text{ min.}, 1\text{ min.}, 2\text{ min.}, 3\text{ min.})$ and ${\lambda_0}^2 = (10^{-3}, 10^{-2}, 10^{-1}, 10^{0}, 10^{1}, 10^{2})$, respectively.

4.4.4 Results

Figure 4-5 shows the time series of the estimated positions at sites TOS2 and MYGI. The positions are aligned to the ITRF 2014 (Altamimi et al., 2016) and transformed into local ENU coordinates. Comparing the time series derived by the existing scheme (SGOBS version 4.0.2; used in Yokota et al., 2019; see also Section 4.3), GARPOS reproduced almost the same trends for both sites. GARPOS might have succeeded in slightly suppressing the dispersion around the averaged velocity extracted from the neighboring epochs. Whereas the previous method corrected the sound speed gradient structure with step-by-step procedure, the proposed method has an advantage in directly extracting the structure by simultaneous estimation of all parameters.

TOS2 is located offshore in the south of Shikoku Island, southwestern Japan, above the source region of the 1946 Nankaido earthquake (e.g., Sagiya and Thatcher, 1999) along the Nankai Trough. According to Yokota and Ishikawa (2020), who investigated the transient deformations at the GNSS-A sites along the Nankai Trough, no significant signal was detected at TOS2. The results by the proposed method show the same trends as the conventional results. Although the trend of horizontal displacement seems to be changed in 2018 or 2019, careful inspection is needed because the transponders had been replaced during this period.

MYGI is located in the offshore east of Miyagi Prefecture, northeastern Japan, which experienced the 2011 Tohoku-oki earthquake (Sato et al., 2011). After the earthquake, significant westward postseismic movement and subsidence due to the viscoelastic relaxation has been observed at MYGI (Watanabe et al., 2014; see also Chapter 5). The postseismic movements continue but appear to decay. It is true that the changes in the displacement rate at these sites are crucial in seismic and geodetic researches, but discussing these matters is beyond the scope of the present paper. The point is that the seafloor positioning results were well reproduced by the proposed method.

4.4.5 Discussion

Typical examples for the estimation results for each observation, i.e., the time series of travel time residuals, and sound speed perturbation interpreted from the correction coefficient, are shown in Figure 4-6. Results for all the datasets are available in Supplementary Figure 1 of Watanabe et al. (2020c).

In the most cases for site TOS2, both terms of the estimated sound speed gradient vector stably direct south to southeast. Because the sound speed increase with the water temperature,

it means that the water temperature is higher in the southern region. The results that $\boldsymbol{g}_2$ is comparable with $\boldsymbol{g}_1$ in many cases indicate that the gradient of water temperature continues to the deeper portion, as discussed in the previous section. This is consistent with the fact that the Kuroshio current continuously flows on the south of TOS2.

In contrast, the directions of gradient terms at MYGI have less constancy than TOS2. Unlike the area around TOS2 where the Kuroshio current dominantly affects the seawater structure, MYGI is located in an area with a complicated ocean current system (e.g., Yasuda, 2003; Miyazawa et al., 2009). Watanabe and Uchida (2016) have also shown that the temperature profiles at MYGI vary widely with observation epochs. These features cannot be resolved by the simpler model with single sound speed gradient parameter.

The complexity in the sound speed variation at MYGI tends to lead to large variations in the residual travel time. Nevertheless, the proposed method successfully extracted the smooth sound speed structure for many observation epochs, except a few epochs such as June 2013 (MYGI.1306.kaiyo_k4) and June 2019 (MYGI.1906.meiyo_m5) shown in Supplementary Figure 1 of Watanabe et al. (2020c). In these epochs, relatively larger values for the hyperparameter ${\lambda_0}^2$ were adopted and caused larger variations in each term of Γ. Possible causes of this include the systematic errors in other observation subcomponents such as the random walk noise in GNSS positioning, the drifts of gyro sensor, or the time synchronization error between the devices.

Preferred models for all the tested epochs had positive values for data correlation length, μ_t. It is considered that the plausible estimation of sound speed is realized by introducing the statistic information criteria and the information of data covariances.

To discuss the effects of the data covariance, we tested the cases for the models without assuming the data correlation, i.e., $\mu_t = 0$. Figure 4-7 shows the preferred models selected from ${\lambda_0}^2 = (10^{-3}, 10^{-2}, 10^{-1}, 10^{0}, 10^{1}, 10^{2}, 10^{3}, 10^{4})$ and $\mu_t = 0$. It is clear that the preferred models without assuming the data correlation have larger ${\lambda_0}^2$. Although the residuals of travel time were reduced in these models, overfittings occurred for each term of Γ. Comparing the preferred and less-preferred results, the existence of data covariance components contributes to suppressing the overfitting and to selecting a model with less perturbation by decreasing the impact of individual data on model parameters.

To confirm the stability of the seafloor positioning results, the differences of seafloor position for the tested models from the most preferred models are summarized in Figure 4-8.

The differences in estimated positions for most of the tested models converged in several centimeters. For both sites, variations in the vertical component tend to be larger for larger values of $\lambda_0{}^2$. It indicates that finer hyperparameter tuning is not required when considering the application to seafloor positioning.

As another application of GNSS-A to oceanography, temporal changes of the oceanographic structure within the observation epoch can be extracted using the proposed method. For example, the estimated sound speed gradient $\boldsymbol{g}_1$ in the epoch of MYGI.1802.kaiyo_k4 (Figure 4-6f) suggests that the dominant oceanographic structure had changed at 01:00-03:00 UTC. On the other hand, a temporal variation with a relatively short period of several tens of minutes remains in the travel time residuals, which might be caused by the internal gravity wave. To improve the detectability of relatively short-period perturbations, further adjustments and verifications of the proposed model will be required.

4.5 Conclusions

The author developed the new GNSS-A analysis software GARPOS and published it as an open source software, based on the algorithm demonstrated in Chapter 2. GARPOS provides a stable solution for a generally ill-posed problem caused by the correlation among the model parameters, by introducing the hyperparameter tuning based on the ABIC minimization and data covariance to rationalize the normalization constant of the posterior pdf (see Chapter 2 for theoretical detail).

The most important point is that GARPOS succeeded in directly extracting the time-dependent sound speed field with two end members of spatial gradient terms, which are roughly characterized by depths, even when the observers used only one sea-surface unit. Statistical approach allowed us to suppress the overfitting and thus to obtain simpler sound speed field from densely collected dataset. It successfully reproduced the stationary southward sound speed gradient at TOS2, which is consistent with the Kuroshio current.

On the other hand, model overfits were shown in several epochs. These overfits can be caused not only by the actually complicated sound speed field but also by other error sources which were not well included in the model. It means that the hyperparameter tuning also plays a role in the verification of dataset and model. Error analyses in such cases might rather help improving the GNSS-A accuracy and methodology.

The author also suggested a simplified and readable formatting for the GARPOS input/output files. Researchers can enter into the field of seafloor geodesy by collecting the

listed data with adequate precision. Since each subcomponent of GNSS-A technique, i.e., GNSS positioning, acoustic ranging, and so on, has been well established, observers can combine them on their platform. Especially, GNSS-A is expected to be practicalized in the near future with an unmanned surface vehicle (Chadwell, 2016) or a buoy (e.g., Tadokoro et al., 2020; Kinugasa et al., 2020). Even in the case of the stationary observation due to small cruising speed, GARPOS may provide the solutions by making a slight modification in the prior variance-covariance matrix.

There is a room for improvement in setting the prior information for transponders' positions, $\boldsymbol{X}_j^0$. For instance, the displacement of transponder array from the previous epoch is predicted as small as several centimeters when the interval of observation visits is short. Such assumption leads to the application of the inter-epoch filtering. Furthermore, it has a possibility to progress to the kinematic seafloor positioning, as shown by Tomita et al. (2019). The publication of GARPOS on the open-access repository will contribute to enhancing the researchers' engagement and the future development on the GNSS-A technique.

Table 4-1. List of observable and estimation parameters used in GARPOS (modified from Watanabe et al., 2020c).

Parameter	Description	Name in I/O file	I/O file	type	unit
t_{i_+}	transmit time	*ST*	I-2	obs	s
t_{i_-}	reception time	*RT*	I-2	obs	s
$\boldsymbol{Q}(t_{i_+})$	Position of GNSS antenna at t_{i_+} in ENU coordinates	*ant_e0* *ant_n0* *ant_u0*	I-2	obs	m
$\boldsymbol{Q}(t_{i_-})$	Position of GNSS antenna at t_{i_-} in ENU coordinates	*ant_e1* *ant_n1* *ant_u1*	I-2	obs	m
$\boldsymbol{\Theta}(t_{i_+})$	Attitude of platform at t_{i_+}	*roll0* *pitch0* *head0*	I-2	obs	deg.
$\boldsymbol{\Theta}(t_{i_-})$	Attitude of platform at t_{i_-}	*roll1* *pitch1* *head1*	I-2	obs	deg.
γ_i	Correction coefficient	*gamma*	O-2	est	-
$\boldsymbol{M^0}$	Prior ATD offset	*ATDoffset*	I-1	obs	m
$\boldsymbol{X_j^0}$	Prior position of transponder	*M{j}_dPos*	I-1	obs	m
$\boldsymbol{\Delta X^0}$	Prior offset of transponder array	*dCentPos*	I-1	obs	m
$\widehat{\boldsymbol{M}}$	Posterior ATD offset	*ATDoffset*	O-1	est	m
$\widehat{\boldsymbol{X_j}}$	Posterior position of transponder	*M{j}_dPos*	O-1	est	m
$\widehat{\boldsymbol{\Delta X}}$	Posterior offset of transponder array	*dCentPos*	O-1	est	m
$V_0(u)$	Reference sound speed profile	CSV table	I-3	obs	m/s
$K^{\langle 0 \rangle}$	Number of internal knots for α_0	*nmp0*	I-4	setting	-
$K^{\langle 1E \rangle}, K^{\langle 1N \rangle}$	Number of internal knots for $\boldsymbol{\alpha_1}$	*nmp1*	I-4	setting	-
$K^{\langle 2E \rangle}, K^{\langle 2N \rangle}$	Number of internal knots for $\boldsymbol{\alpha_2}$	*nmp2*	I-4	setting	-

* Note that $K^{\begin{Bmatrix}0\\1E,1N\\2E,2N\end{Bmatrix}} = nmp\begin{Bmatrix}0\\1\\2\end{Bmatrix} \times (\text{number of subset})$ in GARPOS.

Table 4-2. List of hyperparameter in GARPOS (after Watanabe et al., 2020c).

Hyper-parameter	Description	Formulation set in (I-4)	Name in Setting file	unit
μ_t	Correlation length of data	μ_t	*mu_t*	min.
μ_{MT}	Data correlation coefficient b/w the different transponders	μ_{MT}	*mu_mt*	-
${\lambda_0}^2$	Smoothness parameter for α_0	$\log_{10}{\lambda_0}^2$	*Log_Lambda0*	-
${\lambda_{1E}}^2$	Smoothness parameter for α_{1E}	$\log_{10}\left(\frac{{\lambda_{\langle\cdot\rangle}}^2}{{\lambda_0}^2}\right)$	*Log_gradLambda*	-
${\lambda_{1N}}^2$	Smoothness parameter for α_{1N}			-
${\lambda_{2E}}^2$	Smoothness parameter for α_{2E}			-
${\lambda_{2N}}^2$	Smoothness parameter for α_{2N}			-
σ^2	Scale of measurement error	N/A	N/A	-
ρ^2	Scale of a priori positioning error	N/A	N/A	m^2

* Note that σ^2 is calculated analytically, and that ρ^2 is set in (I-2).

Table 4-3. Locations and observation periods of the GNSS-A observation sites used in Chapter 4 (after Watanabe et al., 2020c).

Site	Latitude	Longitude	Height	Number of epochs	Observation period
TOS2	32.43 °N	134.03 °E	–1740 m	31	2011.904 – 2019.863
MYGI	38.03 °N	142.92 °E	–1640 m	33	2011.238 – 2019.803

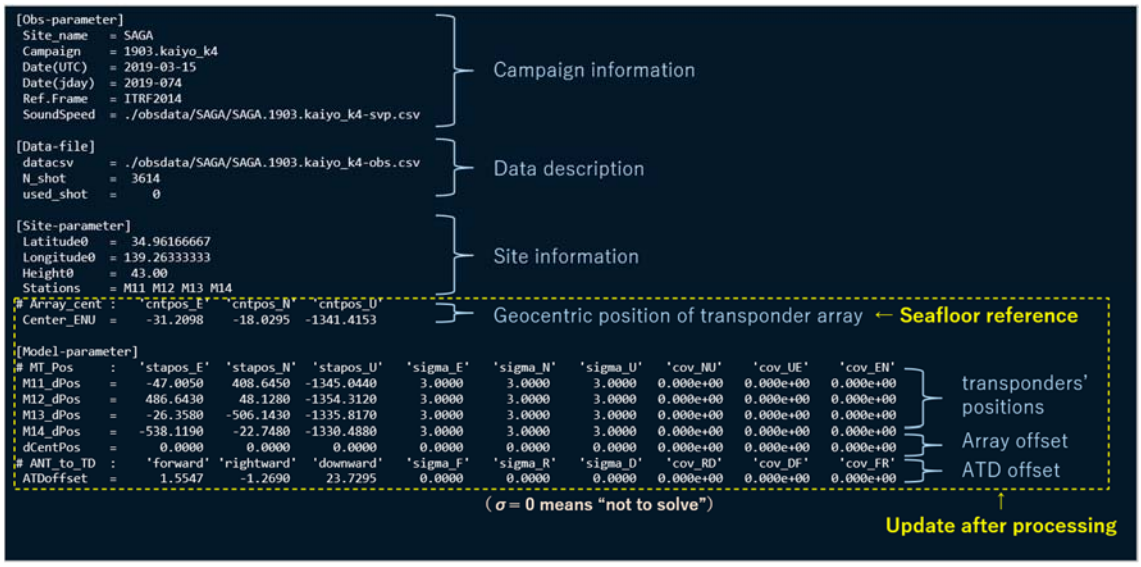

Figure 4-1. An example for the site parameter file (I-1/O-1).

```
,SET,LN,MT,TT,flag,ST,ant_e0,ant_n0,ant_u0,head0,pitch0,roll0,RT,ant_e1,ant_n1,ant_u1,head1,pitch1,roll1
0,S01,L01,M01,2.271449,False,12998.546235,-8.76681,1474.63035,13.59756,186.4,-0.76,0.71,13001.87919,-8.50997,1465.94866,13.39895,186.19,1.95,-1.04
1,S01,L01,M02,3.027084,False,13008.54628,-8.62977,1450.56564,12.7152,188.86,-1.35,0.93,13012.63487,-9.15161,1440.50533,13.80715,189.16,-0.25,0.48
2,S01,L01,M03,3.593219,False,13028.546345,-11.55922,1401.97245,13.50447,191.2,2.0,-0.53,13033.20107,-12.29072,1391.65533,12.53032,191.93,-0.4,-0.86
3,S01,L01,M04,2.954364,False,13038.546375,-13.60719,1378.3708,13.4282,189.78,-0.5,-0.76,13042.562245,-14.65926,1368.03363,12.89624,189.59,1.44,0.93
4,S01,L01,M11,2.138648,False,13048.546455,-15.38928,1354.52261,13.03522,187.99,-2.41,1.43,13051.74661,-14.90793,1345.65016,13.46705,187.15,1.01,-1.35
5,S01,L01,M12,2.875131,False,13058.5464,-15.54531,1329.28916,12.57873,186.09,-1.22,0.2,13062.48304,-14.64234,1319.03164,12.79195,186.08,-1.47,-0.97
6,S01,L01,M13,3.360925,False,13068.5465,-15.8706,1303.541,12.93603,184.7,1.51,1.66,13072.96893,-14.26268,1293.26341,12.65954,185.87,-2.32,0.77
7,S01,L01,M14,2.740823,False,13078.546545,-13.77302,1277.97544,13.20333,183.7,1.21,-2.37,13082.348875,-14.39044,1269.76292,12.37441,183.87,1.02,1.79
8,S01,L01,M01,2.152039,False,13088.54653,-13.83453,1254.04902,13.82523,181.4,-0.75,4.7,13091.760075,-12.29386,1245.41211,13.31,180.52,2.56,-0.54
...
```

Figure 4-2. An example for the observation data file (I-2/O-2).

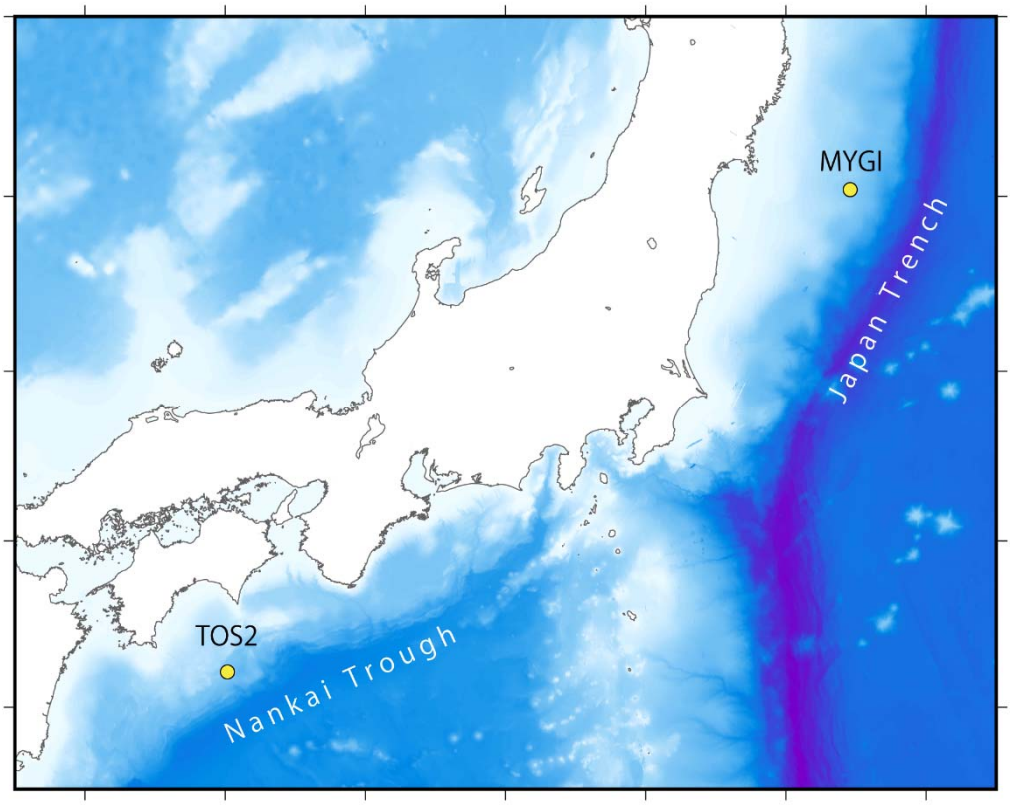

Figure 4-3. Locations of the tested GNSS-A sites TOS2 and MYGI (after Watanabe et al., 2020c).

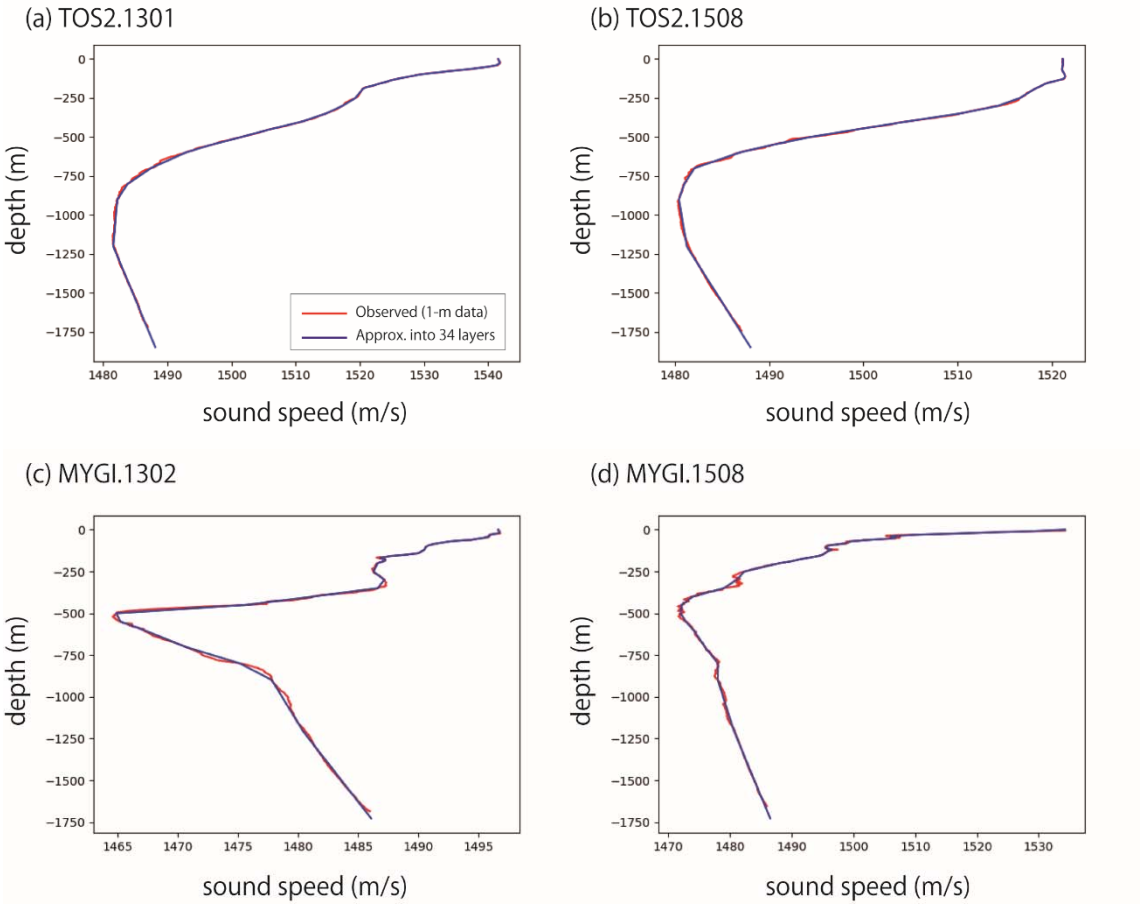

Figure 4-4. Reference sound speed profiles (blue lines) for epochs (a) TOS2.1301 (Jan. 2013), (b) TOS2.1508 (Aug. 2015), (c) MYGI.1302 (Feb. 2013), and (d) MYGI.1508 (Aug. 2015). Red lines indicate 1-m sound speed profiles obtained from the 1-m layered XBT/XCTD data. The figure is adapted from Watanabe et al. (2020c).

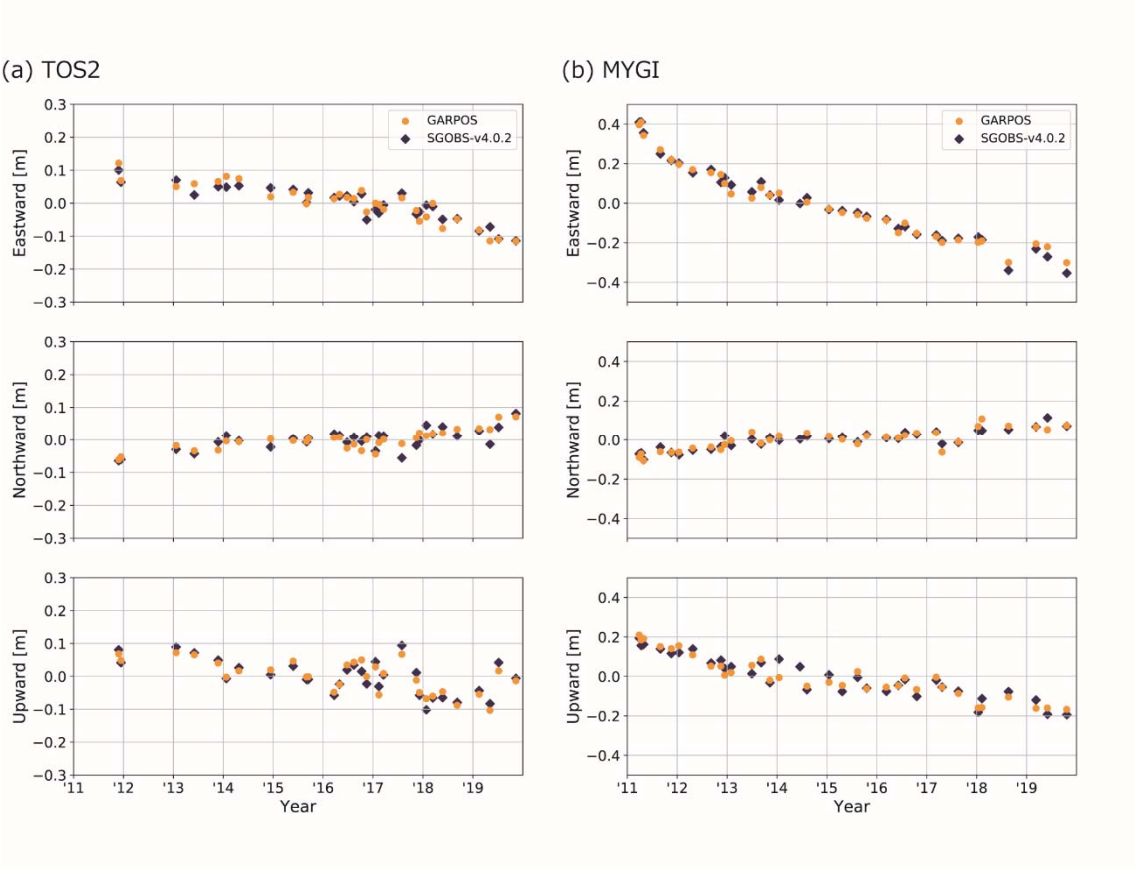

Figure 4-5. Time series of displacement at (a) TOS2 and (b) MYGI solved by GARPOS (orange circles) and SGOBS version 4.0.2 (blue squares). The positions are aligned to the ITRF 2014. The figure is adapted from Watanabe et al. (2020c).

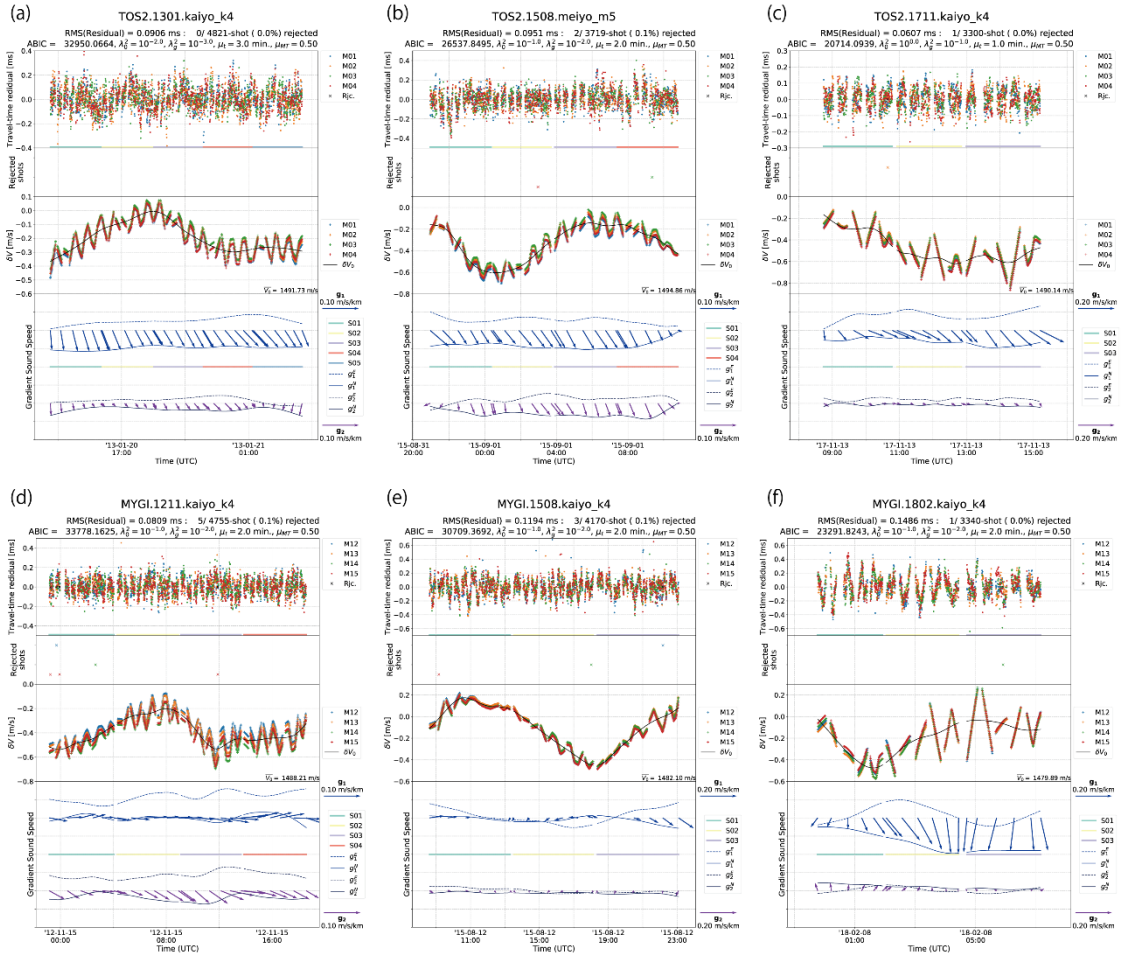

Figure 4-6. Estimated results of the most preferred model for epochs (a) TOS2.1301.kaiyo_k4, (b) TOS2.1508.meiyo_m5, and (c) TOS2.1711.kaiyo_k4 (d) MYGI.1211.kaiyo_k4, (e) MYGI.1508.kaiyo_k4, and (f) MYGI.1802.kaiyo_k4. The top panels show the model residuals of the round-trip travel time. The second panels show the rejected acoustic data in the preprocessing step for determining the array geometry. The third panels indicate the sound speed perturbations, i.e., $\gamma_i \overline{V_0}$ (the crosses), and $\delta V_0(t) \equiv \overline{V_0}\alpha_0(t)$ (black line). The colours of the symbols in these panels identify the target transponders. The blue and purple arrows on the bottom panels indicate the spatial gradient of the sound speed perturbations in north-up expression, i.e., $\boldsymbol{g}_1(t) \equiv \overline{V_0}\boldsymbol{\alpha}_1(t)$, and $\boldsymbol{g}_2(t) \equiv \overline{V_0}\boldsymbol{\alpha}_2(t)$, respectively. Dotted lines and solid lines show the temporal variations of eastward and northward components, respectively. The colored horizontal lines denote the ranges of the observation subsets. The figure is adapted from Watanabe et al. (2020c).

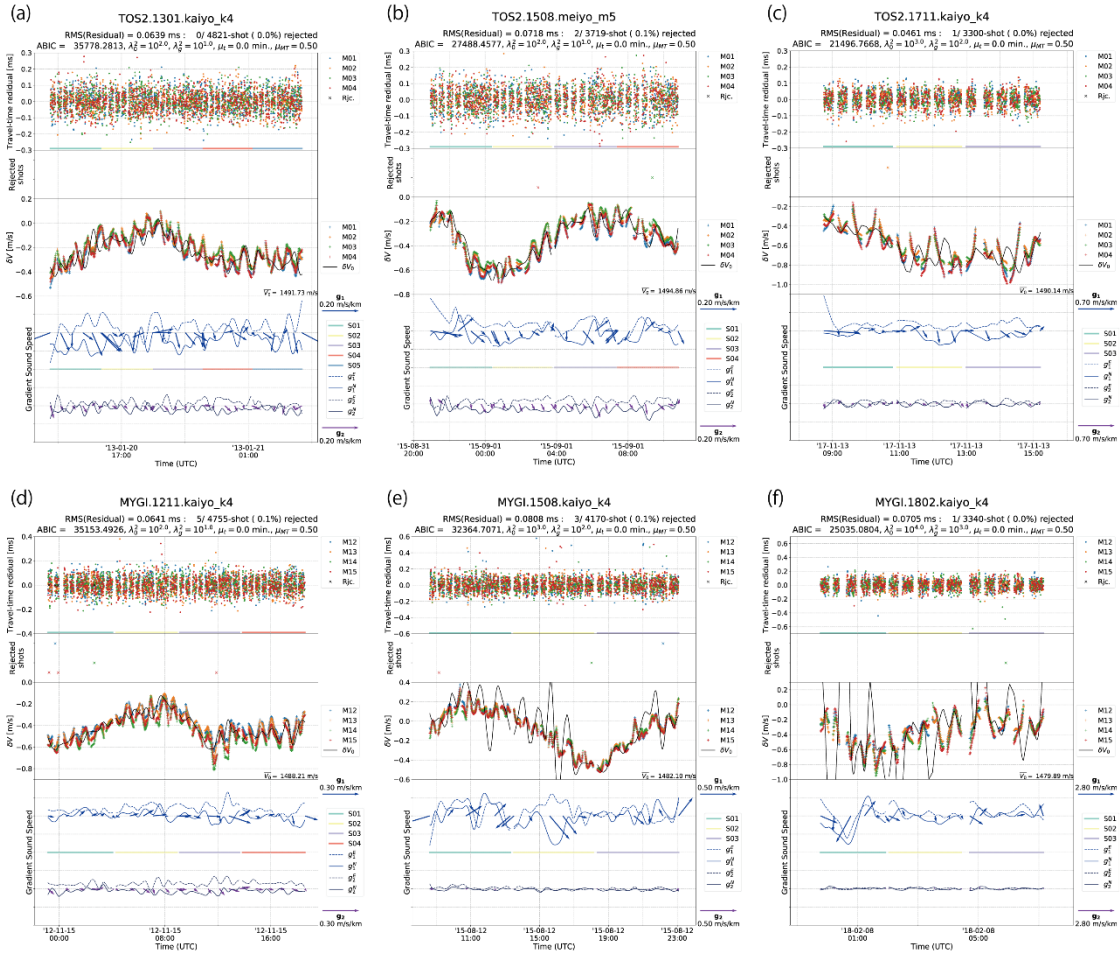

Figure 4-7. Same as Figure 4-4, but for the most preferred model in the models with $\mu_t = 0$. The figure is adapted from Watanabe et al. (2020c).

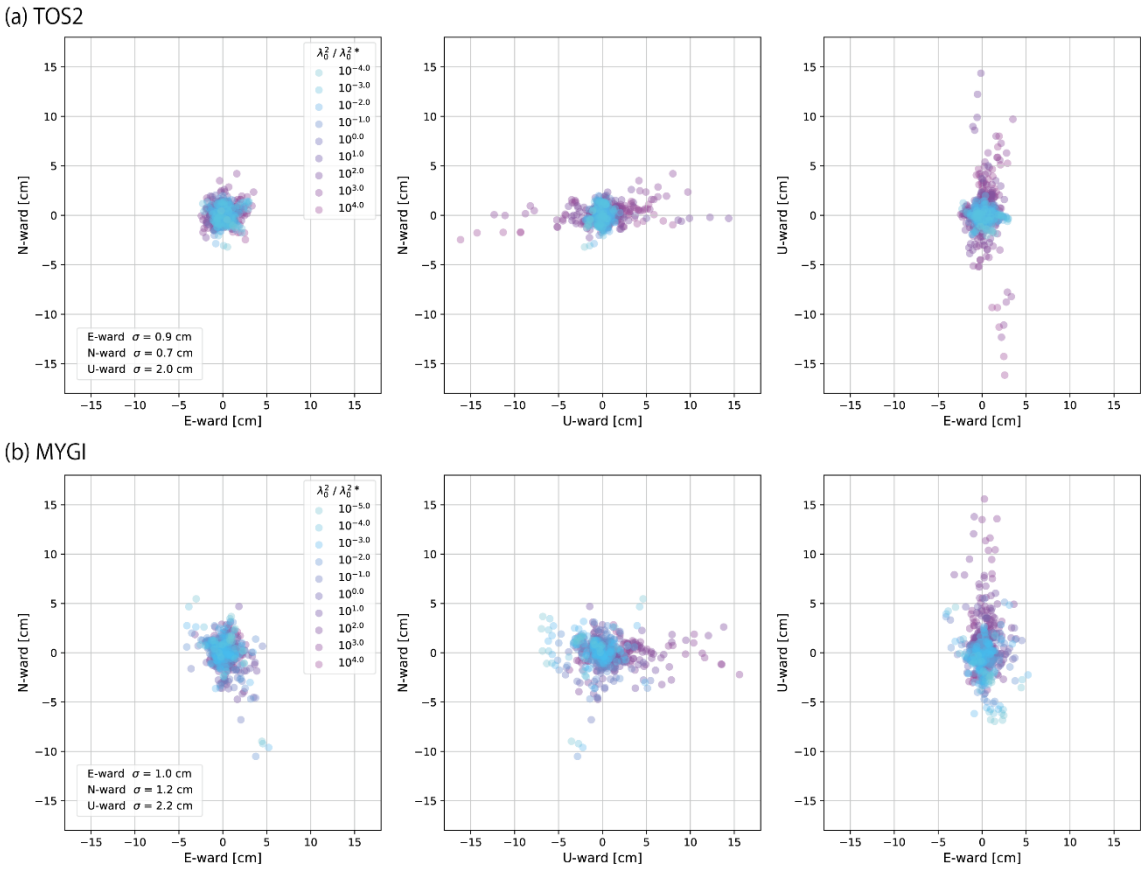

Figure 4-8. Distributions of differences of positions of the tested models from the preferred ones at (a) TOS2 and (b) MYGI for northward-eastward (left), northward-upward (center), and upward-eastward (right) components. The colours of circles indicate the value of ${\lambda_0}^2/{\lambda_0}^{2^*}$. The figure is adapted from Watanabe et al. (2020c).

PART II

GNSS-A applications to the investigation of subduction zone earthquakes

Chapter 5

Detecting secular motion of the subducting Philippine Sea plate

---

This Chapter references the author's work published as Watanabe et al (2015).

Reference:

Watanabe, S., Ishikawa, T., and Yokota, Y. (2015) Non-volcanic crustal movements of the northernmost Philippine Sea plate detected by the GPS-acoustic seafloor positioning. *Earth Planets Space*, **67**, 184. doi:10.1186/s40623-015-0352-6

5.1 Background

The northernmost part of the Philippine Sea plate (PHS) subducts beneath the North American plate (NA) along the Sagami Trough. In this region, thrust earthquakes such as the 1923 Taisho Kanto earthquake (M7.9) and the 1703 Genroku Kanto earthquake (M7.9–8.2) had occurred repeatedly. Additionally, slow slip events off the Boso Peninsula with a recurrence interval of several years have been observed (e.g., Ozawa, 2014). In the northern side of the PHS, the Izu microplate (IM) is considered to move relative to the PHS, whose boundary is located on the west edge of the Sagami Bay (e.g., Sagiya, 1999). The IM subducts beneath the Eurasian plate (EU) along the Suruga Trough, where a large earthquake had occurred in 1854 (Ando, 1975). To investigate the accumulation and/or the release of strain on the plate interface, it is necessary to estimate the precise convergence rate of the subducting oceanic plate relative to the continental plates, as Yasuda et al. (2014) had directly investigated in the Suruga Trough using the GNSS-A technique. Their results of the seafloor geodetic observation indicated the strong coupling in the shallow portion of the plate

boundary.

On the other hand, researchers had estimated the motion of the PHS in the frame of the whole plate kinematics, with geological (e.g., Seno et al., 1993) and geodetic observations (e.g., Sella et al., 2002; DeMets et al., 2010). However, because the most part of the PHS is covered with ocean, the insufficiency of precise geodetic observations makes it difficult to reduce the indeterminacy of the velocities.

Especially in the portion near the boundaries, tectonic plates would not behave as rigid body but deform elastically and inelastically due to the subduction. One of such inelastic deformation on the PHS is caused by back-arc rift along the Izu-Bonin (Ogasawara) trench where the Pacific plate (PAC) subducts beneath the PHS (Taylor et al., 1991). Nishimura (2011) divided the northern PHS into several tectonic blocks, one of which is the fore-arc along the Izu-Bonin trench, to simultaneously evaluate the rigid velocities of blocks and elastic deformation due to the slip deficits on the boundary faults and the volcanic inflations using the GNSS data. However, many geodetic sites on the PHS relatively near the Sagami Trough are located on the islands in the volcanic front, which would be the cause of the local deformation. Investigation of the plate kinematics just subducting along the Sagami Trough is important to evaluate the mechanisms of interplate Kanto earthquake, which possibly causes a severe damage to the Tokyo metropolitan area.

Thus, to obtain the non-volcanic geodetic data in the northernmost part of the subducting PHS in the southern Kanto area, the Japan Coast Guard conducted the campaign GNSS-A seafloor geodetic observations since the middle of the 2000's. In this chapter, comparing the results of the seafloor observation to the models of crustal block kinematics, we clarified the motion of the northernmost PHS.

5.2 Data and Methods

We analyzed the GNSS-A data at the sites along the Sagami Trough named BOSS and SAGA (Figure 5-1, Table 5-1), for the periods from September 2007 to November 2013 and from January 2005 to April 2015, respectively, using SGOBS (Fujita et al., 2006) version 3.6.3 (see Section 3.3) under rigid-array constraints (Matsumoto et al., 2008). The positions of seafloor transponders are aligned to the ITRF2005 (Altamimi et al., 2007), via being tied to the F3 solution for the terrestrial GEONET stations operated by the Geospatial Information Authority of Japan (Nakagawa et al., 2009). BOSS is located 50 km southern off the Cape Nojima-saki, while SAGA is located in the Sagami Bay, 10 km eastern off the Cape Kawana-

saki. Both sites had been installed on the flat seafloor of the PHS along the Sagami Trough, distant from the active volcanoes (Izumi et al., 2013).

As described by Ishikawa et al. (2020), for the earlier stage of the observations, specifically before 2007, the on-board equipment was mounted at the stern of the vessel with an 8-m-long pole. During the GNSS-A observations at that time, the vessel was adrift. In 2008, the construction of hull-mounted system enables us to operate the sailing observation, in which we can control the track lines to collect spatially well-balanced data. Detailed methodologies and accuracy of this technique are shown in Sato et al. (2013b) and Ishikawa et al. (2020).

5.3 Results

Figure 5-2 plots the estimated coordinates of the observation sites represented in the ITRF2005 by setting those of the first sailing observation epoch at each site as a reference. The relative positions of each epoch are shown in Table 5-2.

Linear trends for each component of the displacement using the M-estimation method (a robust regression technique) are also shown in Figure 5-2, with the blue hyperbolic lines indicating the 90% two-sided confidence intervals. For the period before the 2011 Tohoku-oki earthquake (M_w 9.0), GNSS-A results indicated the velocity of 1.0 ± 1.1 cm/year westward and 0.5 ± 1.1 cm/year northward, and the velocity of 0.5 ± 0.3 cm/year westward and 1.1 ± 0.3 cm/year northward in the ITRF2005 with the 90% confidence at BOSS and SAGA, respectively. For the period after the Tohoku-oki earthquake, the postseismic deformation affects the motions at both sites (see also Chapter 7). It was unable to extract the reliable postseismic trend at BOSS, because the only four times of GNSS-A observations had performed after 2011. At SAGA, average displacement rate of 0.3 ± 0.7 cm/year eastward and 0.4 ± 0.9 cm/year northward in the ITRF2005 was obtained for the period from 2012 to 2015. From the discontinuous step of positions between just before and after the Tohoku-oki earthquake, eastward coseismic displacement of about 10 cm was detected at SAGA.

Table 5-3 and Figure 5-3 show the velocities before the Tohoku-oki earthquake adjusted to values relative to the stable part of the EU, on the basis of the angular velocity presented by Altamimi et al. (2007). The ellipses in Figure 5-3 indicate the 90% confidence interval. The velocities at the terrestrial sites deployed by the Geospatial Information Authority of Japan are also shown in Figure 5-3, which were derived from the daily coordinates of the GEONET F3 solution from January 2008 to July 2009 (Nakagawa et al., 2009). The consistency of seafloor results with the regional velocity field of the GEONET in Figure 5-3 supports for the

validation of our seafloor results.

The reason why the confidence interval of the rate at SAGA is smaller than that at BOSS is due to not only the number of the positioning data but also the oceanographic condition. The condition was usually simpler in the Sagami Bay than off Boso Peninsula where the Kuroshio Current is more likely affect the sound speed.

5.4 Discussion and conclusions

First, we compared the result at BOSS before the Tohoku-oki earthquake with the plate kinematics models. Because BOSS is located in the trench-side of the volcanic front and away from block boundaries, slip deficits on the plate boundaries cause no significant deformation at BOSS except on the PAC-PHS boundary. In fact, a southward displacement of up to 0.1 cm/year is expected at BOSS from the slip deficit on the PHS-NA boundary faults listed in Nishimura (2011), whereas the PAC-PHS boundary has possibility to cause a westward displacement of approximately 1–2 cm/year. However, the geodetic observations on the islands have little resolution in the slip deficit on the PAC-PHS boundary. We therefore made the assumption that the deficit rate is zero tentatively.

The Euler vector for the rigid PHS had been evaluated by several models. Estimated values of velocity at BOSS are shown in Table 5-4. Seno et al. (1993) determined the velocities of the PHS using the earthquake slip vectors including northern boundaries of the PHS. It led to the NUVEL-1A model (DeMets et al., 1994), in which the PHS is expected to move at a rate of 0.7 cm/year westward and 0.7 cm/year northward relative to the ITRF at BOSS. According to the MORVEL model and the REVEL model, which were proposed using the geodetic data by DeMets et al. (2010) and Sella et al. (2002), respectively, BOSS moves relative to the ITRF at a rate of 2.4 cm/year westward and 1.3 cm/year northward, and a rate of 2.2 cm/year westward and 1.3 cm/year northward, respectively. The residuals of the observed velocity to the plate motion models are statistically significant. The eastward component of the residuals is unaccountable even if the PAC-PHS interface is assumed to be locked. That is because the slip deficit on the PAC-PHS interface would cause the westward deformation at BOSS, as Sella et al. (2002) had already pointed out at the islands in the Izu-Bonin arc. They thus considered the residuals as non-rigid plate deformation such as spreading of the back-arc basin.

Whereas these models had estimated the motion of the PHS from geodetic data at only several sites far from its boundaries, Nishimura (2011) used additional sites near the

boundaries to simultaneously estimate rigid velocities and elastic deformation of the tectonic blocks. In this block kinematics model, back-arc rift along the Izu-Bonin Trench was taken into account as well. The fore-arc area along the Izu-Bonin Trench is considered as a rigid block separated from the PHS, called Izu-arc block (IA). At BOSS, the IA is calculated to move at a rate of 1.3 cm/year westward and 1.4 cm/year northward relative to the ITRF.

Although the seafloor geodetic data is quantitatively consistent with the velocities derived from both the NUVEL-1A and Nishimura's model, the difference between these models is emphasized in the easternmost part of the Nankai Trough. In this region, the strong coupling on the plate boundary was indicated by Yokota et al. (2015) from the observed displacement rates at the seafloor sites TOK1 and TOK2. According to them, the velocity obtained at TOK2 was significantly larger than the velocity of the PHS in the NUVEL-1A model. Thus, they pointed out that the motion of the IM should be considered. On the basis of Nishimura's tectonic model, the velocity at TOK2 is almost as large as that of both the PHS and the IM, despite the uncertainty about the location of the PHS-IM boundary. It supports the Nishimura's model, though more direct evidences by seafloor observation in the southwestern part of the IM are needed to clarify the tectonics of the subducting IM.

On the other hand, SAGA is located near two block boundaries. One is the Sagami Trough, and the other divides the IM from the IA in the west side of the Sagami Bay. Figure 5-4 plots the cross section of the observed displacement rates relative to the EU. Along the Sagami Trough, the IA subducts northward (Figure 5-4a), almost perpendicular to the trough (No et al., 2014). In the western boundary between the Sagami Bay (on the IA) and the Izu Peninsula (on the IM), the left-lateral strike slip fault is indicated (Figure 5-4b), as the 1980 Izu-Hanto-Toho-oki earthquake (M6.7) had occurred on a portion of the boundary (e.g., Takeo, 1988; Nishimura et al., 2007).

To estimate the slip deficit rate on the IM-IA boundary fault, we calculated the northward component of the surface deformation in an elastic half-space by the method of Okada (1992), applying backslip model (Savage, 1983). The geometry and location of the faults are the same as the IM-IA boundary faults indicated in Table 2 of Nishimura (2011), but depths are set to 0 km. Four green lines in Figure 5-4a indicate the assumed displacement rates with the coupling rate of 0%, 50%, 80%, and 100%. The results suggest that deformation with 50–80% coupling fits to the observed data, which is consistent with Nishimura's estimation. Therefore, the IM-IA boundary fault in the western side of the Sagami Bay is coupled with the deficit rate of a few centimeters per year.

For the seismogenic area of the Kanto earthquakes along the Sagami Trough, interplate backslip on the PHS-NA boundary would cause no significant deformation on the PHS because of its low dip angle. The GNSS-A results indicated that the movement at BOSS is interpreted as the rigid motion of the IA, which supports the consistency of Nishimura's model even on the seafloor near the trough axis. It provided the additional supporting evidence that the direction and rate of PHS subduction along the Sagami Trough can be described as the kinematics of the IA. These seafloor geodetic results can contribute to evaluating the seismic cycle and risks of the thrust earthquakes. In the future, seafloor geodetic data on the eastern area along the Sagami Trough, where the larger tsunami could be excited, will be required for the further investigations for the seismogenesis beneath the seafloor.

After the Tohoku-oki earthquake, GNSS-A observations were performed four times at BOSS. The change of the displacement rates before and after the earthquake is not significant. Thus, we assumed that the postseismic deformation of the Tohoku-oki earthquake would cause no significant movement at BOSS. Then comparing the average positions relative to the IA before and after the Tohoku-oki earthquake, we derived the eastward coseismic displacement of 3.9 ± 2.0 cm at BOSS. We also detected the eastward coseismic displacement of about 10 cm at SAGA. According to the coseismic slip model estimated by Iinuma et al. (2012), coseismic displacements of 4.5 cm eastward and of 12 cm east-southeastward were estimated at BOSS and SAGA, respectively, which are both consistent with our results.

The displacement rate at SAGA after the earthquake (specifically 2012-2015) slightly changed from the rate before the earthquake, though the difference of 0.8 ± 0.7 cm/year eastward and 0.7 ± 0.9 cm/year southward is almost as small as the confidence level. The change is considered to be caused by the postseismic deformation of the event (e.g., Wang et al., 2012), like other geodetic sites in Japan (e.g., Ozawa et al., 2012; Watanabe et al., 2014). At the GEONET sites Niijima and Toshima on the islands in the IA, the difference between the displacement rates before (from January 2008 to July 2009) and after the Tohoku-oki earthquake (from January 2013 to January 2015) was approximately 0.9 cm/year eastward and 0.2–0.3 cm/year southward, which is consistent with the result at SAGA.

The GNSS-A observations shown in this Chapter provided the non-volcanic geodetic data on the PHS, almost all part of which is covered with ocean except for small volcanic islands. They played an essential role to investigate the kinematics in the southern Kanto area. Although the GNSS-A data determined the velocity of the PHS along the Sagami Trough, the subducting velocity along the Nankai Trough still has ambiguity. The ambiguity of the kinematics models will be reduced by further observations near the troughs, e.g., around the

Zenisu Ridge, simultaneously determining the location of the IM-IA boundary.

Table 5-1. Positions of seafloor sites (after Watanabe et al., 2015).

Site name	Latitude (degree)	Longitude (degree)	Height (m)
BOSS	34.42931 N	139.86505 E	-1409
SAGA	34.96106 N	139.26318 E	-1298

Table 5-2. Estimated relative site positions. Reference frame is ITRF2005. Reference position is the first sailing observation epoch. Asterisks (*) denote the observation epochs with drift observation (after Watanabe et al., 2015).

(a) BOSS

Epoch (year)	Eastward (m)	Northward (m)
2007.712*	0.0160	0.0015
2008.704	0.0000	0.0000
2009.309	-0.0272	-0.0270
2009.542	0.0131	-0.0089
2009.939	-0.0095	0.0019
2010.893	-0.0206	0.0194
2011.301	0.0059	0.0165
2012.706	-0.0184	0.0219
2013.526	0.0030	0.0426
2013.879	-0.0311	0.0763

(b) SAGA

Epoch (year)	Eastward (m)	Northward (m)
2005.076*	-0.0005	-0.0458
2006.027*	-0.0039	-0.0123
2007.084*	-0.0110	-0.0296
2007.731*	-0.0304	-0.0252
2008.284*	-0.0405	-0.0287
2008.517	0.0000	0.0000
2008.520*	-0.0006	0.0160
2009.539	-0.0243	0.0037
2010.589	-0.0381	0.0203
2010.942	-0.0200	0.0069
2011.164	-0.0396	0.0301
2011.347	0.0639	0.0602
2011.463	0.0491	0.0731
2012.101	0.0793	0.0887
2012.712	0.1067	0.1207
2012.901	0.0704	0.0572
2013.534	0.0684	0.0740
2013.876	0.0650	0.0702
2014.073	0.0907	0.0991
2014.463	0.0881	0.0907
2015.208	0.0911	0.0773
2015.326	0.0752	0.0991

Table 5-3. Velocities with respect to the Eurasian plate with component variances and covariances (after Watanabe et al., 2015).

Site name	Epochs	Velocity (cm/year)		Variance and Covariance ($cm^2/year^2$)		
		E-ward	N-ward	Var(E)	Var(N)	Cov (E, N)
BOSS	SEP 2007 - NOV 2010	-3.5 ± 1.1	1.8 ± 1.1	1.11	1.26	0.06
SAGA	JAN 2005 - MAR 2011	-3.1 ± 0.3	2.4 ± 0.3	0.10	0.10	0.01
	FEB 2012 - APR 2015	-2.2 ± 0.7	1.7 ± 0.9	0.44	0.85	0.10

Table 5-4. Comparison of observed velocities at BOSS with model velocities relative to the ITRF2005 (after Watanabe et al., 2015).

observation / model	Velocity at BOSS (cm/year)	
	E-ward	N-ward
observation (this study)	-1.0 ± 1.1	0.5 ± 1.1
PHS in NUVEL-1A	-0.7	0.7
PHS in MORVEL	-2.4	1.3
PHS in REVEL	-2.2	1.3
IA in Nishimura (2011)	-1.3	1.4

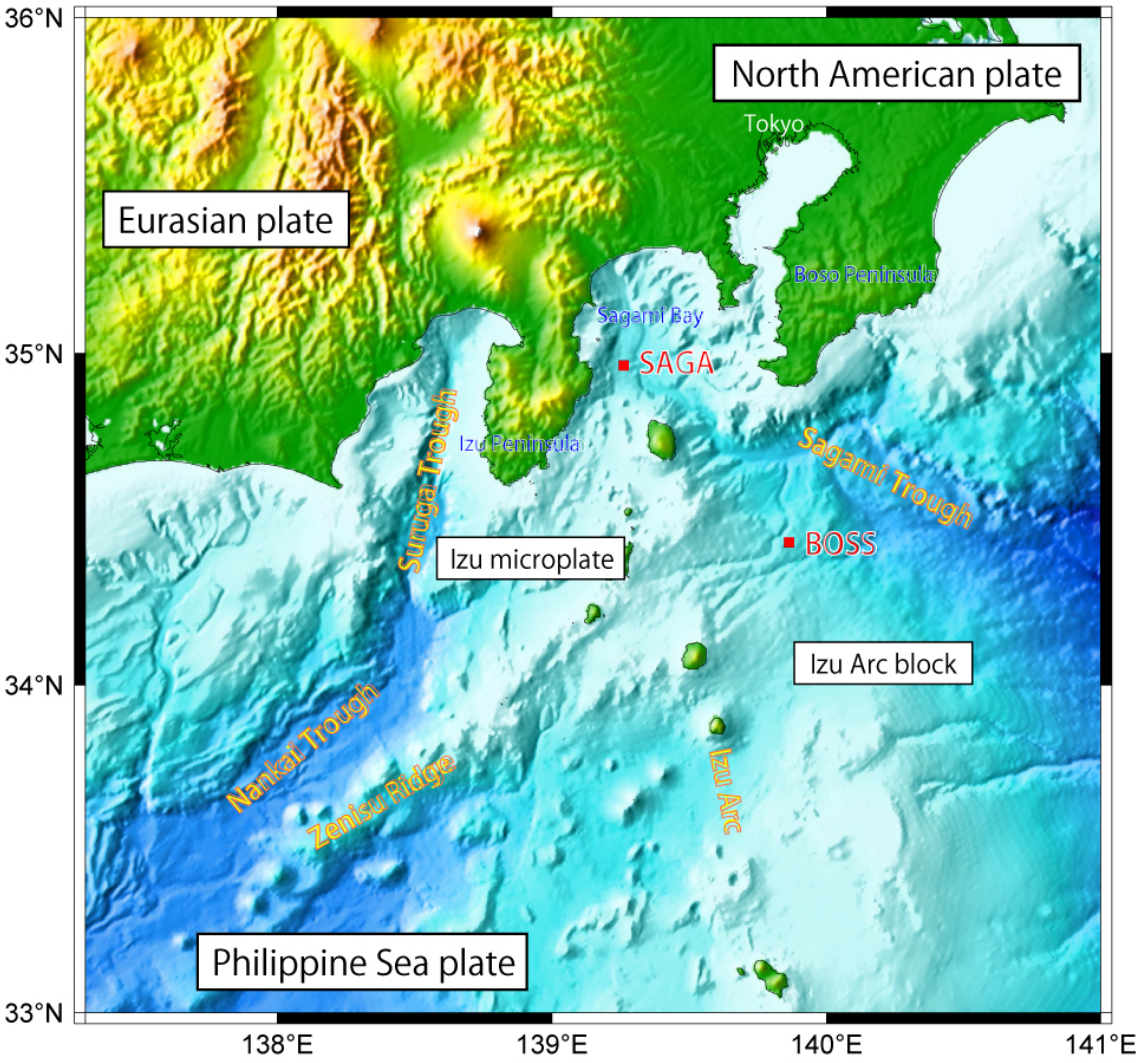

Figure 5-1. Locations of the GNSS-A sites BOSS and SAGA (red squares). BOSS is located on the seafloor between the Sagami Trough and the Izu arc. SAGA is located on the flat seafloor in the Sagami Bay, between the Sagami Trough and the Izu microplate. The figure is adapted from Watanabe et al. (2015).

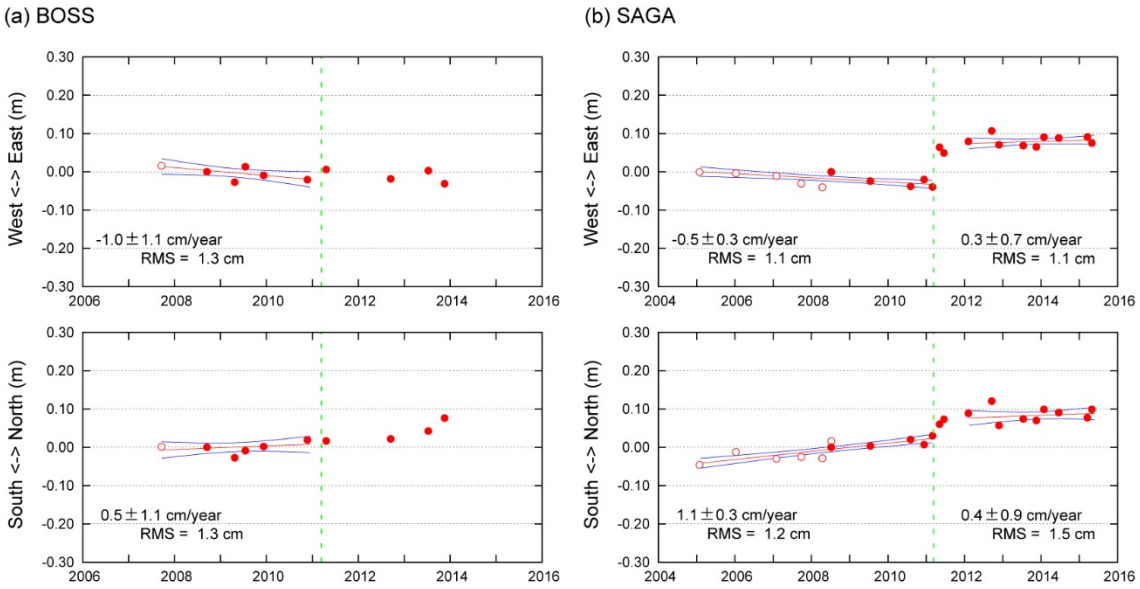

Figure 5-2. Time series of estimated horizontal displacements of array centroid at (a) BOSS and (b) SAGA. The reference frame is ITRF2005 (Altamimi et al., 2007). Open and solid red circles indicate the results from drift and sailing observation, respectively. Linear fitting using the M-estimation method (a robust regression technique) and the 90% two-sided confidence intervals are shown with red and blue lines, respectively. Green dashed lines indicate the occurrence time of the 2011 Tohoku-oki earthquake (M9.0). The figure is adapted from Watanabe et al. (2015).

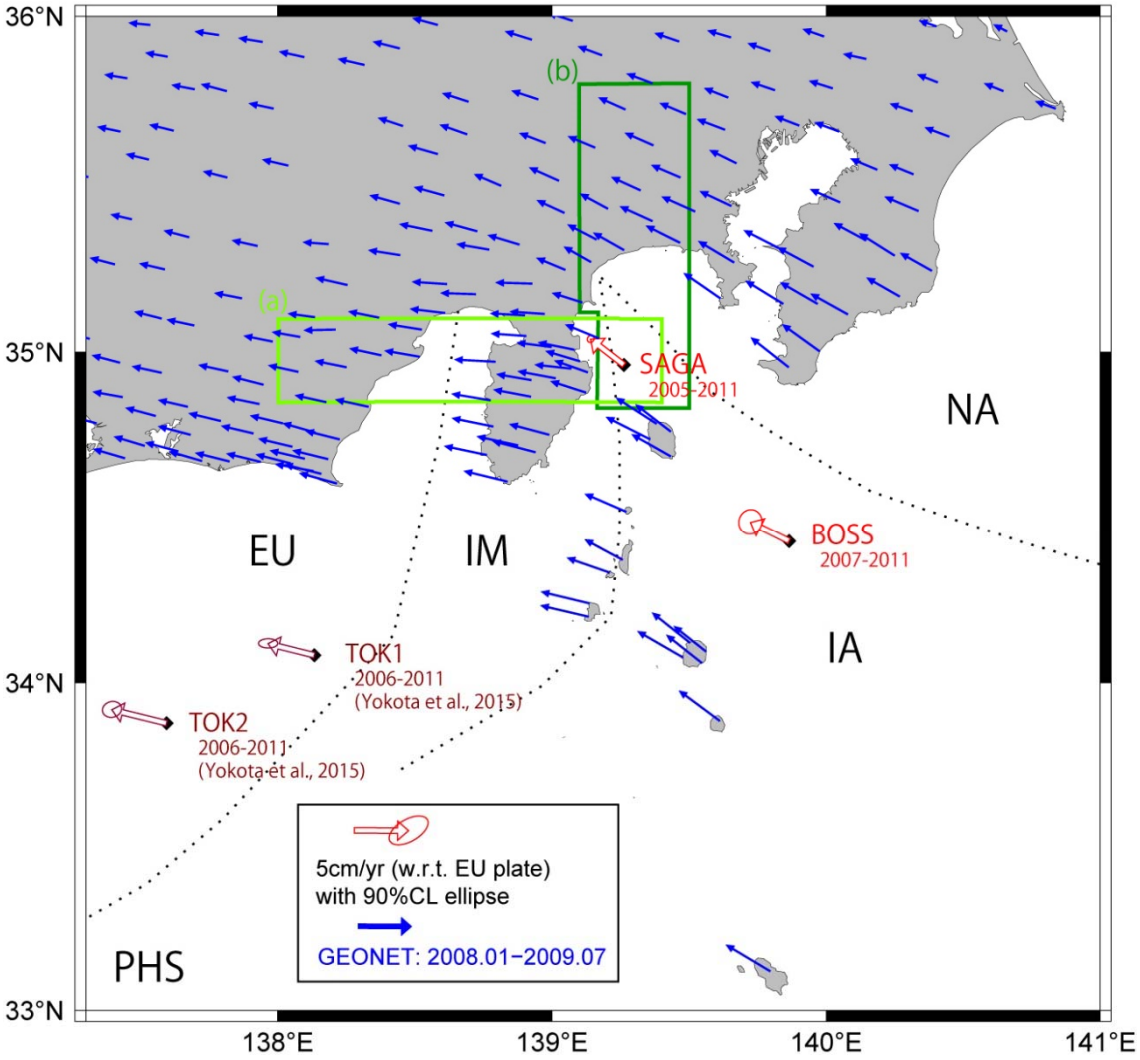

Figure 5-3. Horizontal velocities relative to the Eurasian plate before the 2011 Tohoku-oki earthquake in the Kanto distinct. Red and brown arrows indicate the velocities at the seafloor sites detected in this study and by Yokota et al. (2015), respectively, with 90% confidence-interval ellipses. Terrestrial velocities are estimated using the GEONET sites for the period from January 2008 to July 2009 (blue arrows). Black dotted lines indicate the boundaries of tectonic blocks, though some boundaries are uncertain (e.g., the PHS-IM and the PHS-IA boundaries). Green regions indicate the areas for the cross section shown in Figure 5-4. The figure is adapted from Watanabe et al. (2015).

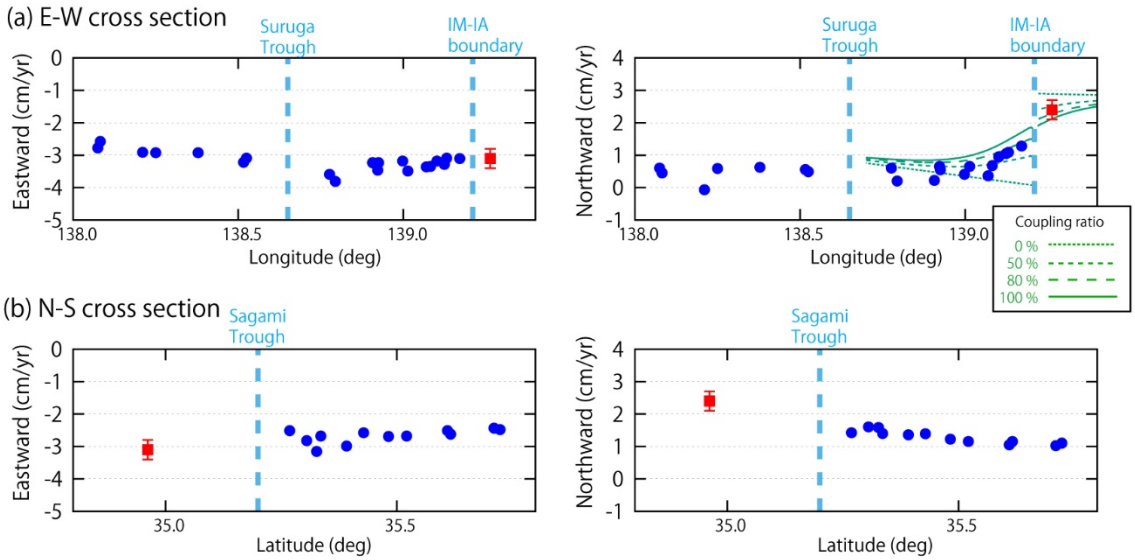

Figure 5-4. Velocity profiles in (a) westward and (b) northward directions from SAGA. Red squares and blue circles indicate the velocities at SAGA and the GEONET sites in the green area in Figure 5-3, respectively. Water blue dashed lines indicate the location of the block boundaries. Green lines indicate the profiles of the northward component of the surface velocity calculated by the method of Okada (1992), applying backslip model, with 0%, 50%, 80%, and 100% coupling. The figure is adapted from Watanabe et al. (2015).

Chapter 6

Tsunami scenarios in the Nankai Trough based on interseismic geodetic data

---

This Chapter references the author's work published as Watanabe et al. (2018).

Reference:

Watanabe, S., Bock, Y., Melgar, D., and Tadokoro, K. (2018) Tsunami scenarios based on interseismic models along the Nankai trough, Japan, from seafloor and onshore geodesy. *J. Geophys. Res. Solid Earth*, **123**, 2448–2461. doi:10.1002/2017JB014799

6.1 Background

By the mid-2000's, the GNSS-A seafloor positioning technique had succeeded in detecting seafloor velocities on the order of several centimeters per year (e.g., Gagnon et al., 2005; Fujita et al., 2006; Bürgmann and Chadwell, 2014). It enabled the researchers to quantify deformation in the offshore regions of subducting plate boundaries where tsunamigenic megathrust earthquakes have repeatedly occurred. For the 2011 Tohoku-oki earthquake (M_w9.0), researchers detected coseismic seafloor displacements greater than 20 m (Sato et al., 2011; Kido et al., 2011) about an order of magnitude greater than onshore GNSS sites (Simons et al., 2011; Melgar et al., 2013). These near-source observations have contributed to significant improvements in the resolution of finite fault slip models (e.g., Iinuma et al., 2012). In this Chapter, we focus on the contribution of widely-deployed near-source GNSS-A sites in the seismogenic zone along the Nankai Trough, southwestern Japan (Yokota et al., 2016), to improve estimates of the slip deficit rate on the plate interface. The motivation is to mitigate hazards by providing constraints on the expected spatial extent and inundation of

tsunamis. Recalling the case of the Tohoku-oki earthquake, land-based geodetic data provided less resolution in the shallow portion of the fault where slip weakening processes during the rupture, e.g., by thermal pressurization of pore fluids (Sibson, 1973), led to the large slip (e.g., Cubas et al., 2015). Even though our understandings of megathrust earthquakes are still rather far from providing the precise description of future coseismic slip, geodetically-derived patterns of slip deficit rate can provide essential constraints on coseismic scenarios, namely, as prior information, more so with the recent availability of GNSS-A observations to supplement onshore GNSS data.

In this Chapter, we introduce two case studies for expected tsunami generation and propagation scenarios at the Nankai Trough. We address one of the main sources of uncertainty in our scenarios, the assumed plate interface geometry, by testing two different geometries and using complementary offshore GNSS-A and onshore GNSS velocity observations for both. First, we refine the model of Yokota et al. (2016) by (1): Adding two GNSS-A data sets at the Kumano basin operated by Nagoya University (Tadokoro et al., 2012) to improve the reliability of the slip deficit estimation; (2) Aligning the geodetic data to the Nankai block (forearc sliver) to derive the slip deficit from the tectonic model of Loveless and Meade (2010) — the earlier model ignored block boundaries such as the Median Tectonic Line (MTL) and may have overestimated the slip deficit rate; (3) Considering two different plate interface geometries — it is essential to use the accurate depth of the plate interface, especially for the offshore region where the faults are located near the observation sites; (4) Estimating and correcting for the postseismic displacements of the 2004 southeastern off the Kii Peninsula earthquakes (M_{JMA}7.1 and 7.4, hereafter the Kii-oki earthquakes). Because the viscoelastic relaxation may last more than several years as directly observed after the 2011 Tohoku-oki earthquake (Watanabe et al., 2014; Sun et al., 2014), it is important to quantify its effects at the near-fault GNSS-A sites and the contribution to the estimated slip deficit rate. Furthermore, the derivation of the postseismic models contributes to the understanding of the rheological properties beneath the Nankai Trough subduction zone, considering the sparseness of measurements with modern geodetic instruments.

Ando (1975) described the occurrence of major earthquakes along the Nankai Trough in terms of segmented source regions namely the Nankaido, Tonankai and Tokai regions experiencing the 1707 Hoei, 1854 Ansei-I and Ansei-II, 1944 Tonankai and 1946 Nankaido tsunamigenic earthquakes, indicating a recurrence time of approximately 100-150 years. Therefore, we assume that a 100-year slip deficit is released instantaneously, and use that as the initial conditions for estimating the expected tsunami propagation and inundation, under

each of two scenarios, as a way to assess hazards along the Nankai Trough.

6.2 Data and Methods

6.2.1 Plate interface geometry

In a previous study (Yokota et al., 2016), the CAMP (Crustal Activity Modelling Program) standard model (Hashimoto et al., 2004) was used as the geometry of the upper surface of the Philippines Sea plate (PHS) (hereafter CAMP geometry, Figure 6-1a). On the other hand, Hirose et al. (2008) considered another geometry of the plate surface, including the previous studies by Baba et al. (2002) and Nakajima and Hasegawa (2007) (hereafter HBN geometry, Figure 6-1b). The HBN geometry includes the surface of a subducting seamount south of the Cape Muroto (Baba et al., 2002). The spatial patterns of both the slip deficit rate and tsunamigenesis strongly depend on the fault geometry in the shallow portion. Therefore, we compared the two geometries in this study. It should be noted that the reference surface for the HBN geometry is the sea surface while the reference surface for the CAMP geometry is the solid Earth surface. This is an important difference especially near the trough, where the water depth reaches 5 km.

6.2.2 Offshore and onshore geodetic data

We used the seafloor GNSS-A data obtained by the Japan Coast Guard (JCG) (from 2006 to 2016; updated from Yokota et al., 2016) and the Nagoya University (from 2004 to 2015; updated from Tadokoro et al., 2012) (see Table S1 of Watanabe et al., 2018), as well as the daily positions of the onshore continuous GNSS sites (GEONET), provided by the Geospatial Information Authority of Japan (GSI) (F3 solution; Nakagawa et al., 2009). To derive our best estimate of the interseismic velocities and the slip deficit rate, the displacements caused by episodic events need to be estimated. Whereas the coseismic and postseismic deformation at the GNSS-A sites associated with the 2011 Tohoku-oki earthquake had been already removed in the earlier studies, the postseismic deformation of the Kii-oki earthquakes (M_{JMA}7.1, 7.4) had not been considered. These earthquakes (foreshock and mainshock), which occurred on Sep. 5, 2004 (UTC), caused the southward coseismic displacements of 20–30 cm at the GNSS-A sites in the Kumano Basin (Kido et al., 2006; Tadokoro et al., 2006). Thus, it is important to quantify the effect of postseismic relaxation at the GNSS-A sites. Previously, Suito (2017) calculated the viscoelastic deformation due to these events using the finite element model (FEM) with a simple Maxwell rheology. They reported postseismic displacement of about 5–6 cm over 10 years at onshore and offshore sites. In this study, to remove the postseismic effect from the geodetic data, we modeled both viscoelastic relaxation

and afterslip using the FEM model with a bi-viscous Burgers rheology by fitting them to the observed postseismic displacements at GNSS sites prior to the slip deficit rate estimation (Section 6.3). Because the used GNSS-A data were observed since 2006 (except KMS since 2004), poroelastic deformation, which typically has smaller relaxation time than the viscoelastic effect, was not taken into account in our model.

6.2.3 Derivation of tsunami scenarios

With the corrected interseismic velocities, the tsunami generation model was derived through the following steps: (1) estimation of the slip deficit rate on the plate boundary by geodetic inversion, (2) modeling seawater lift by the forward calculation, and (3) numerical simulation of the tsunami wave propagation.

To estimate the distribution of slip deficit rate on the plate interface from the GNSS-A and GNSS velocity data with a backslip approach, we modified the static model approach of Melgar and Bock (2013) using the elastic Green's functions of Okada (1992). The source fault consisted of 27 × 9 subfaults (Figure 6-1), which were arranged with approximately 25 km intervals. Each subfault consisted of 5 × 5 rectangular dislocations with approximately 5 × 5 km dimensions to represent the smoother geometry. We assigned the same slip parameterization to 5 × 5 dislocations so that each subfault had a single backslip rate vector. Because the depths of the HBN geometry were measured from the sea surface, we raised all fault depths by the water depth of each GNSS-A site when calculating the Green's functions, according to Iinuma et al. (2015). We applied a constraint of spatial smoothness for estimating the backslip rates on the faults using the Laplacian smoothing matrix. The degree of smoothness was estimated to minimize Akaike's Bayesian Information Criterion (ABIC; Akaike, 1980). The backslip rate on the downdip side was constrained to zero.

We then assumed that the 100-years of slip deficit was released instantaneously based on the average recurrence rate of earthquakes in this region, as referenced earlier. However, one of our major focuses in this study is to investigate how uncertainties in the plate geometry affect the tsunami scenarios so the assumed duration is not critical. The displacements due to the assumed coseismic slip were calculated at the discrete points separated with the range of 0.1 degree within the area of 31.5–35.3 °N and 131.5–139.0 °E (i.e., 39 × 76 points). We took the horizontal effect due to the geographical slope into account according to Tanioka and Satake (1996), using the GEBCO_2014 Grid (30 arcseconds) as the bathymetric data. The distribution of static seawater lift was used as the initial condition of tsunami simulation. We calculated the non-linear but non-dispersive water wave propagation using the open

source software GeoClaw v5.3.1 (available at https://www.clawpack.org/) which solves the two-dimensional shallow water equations with the finite volume technique (LeVeque, 2002). In GeoClaw, adaptive mesh refinement was employed to automatically refine the mesh to higher discretization levels according to the complexity of tsunami. We used topography with several levels of resolution, 50 m, 150 m, and 450 m provided by the JCG and the 30 arcsecond GEBCO_2014 Grid (Figure 6-2).

6.3 Corrections of postseismic deformation due to the 2004 Kii-oki earthquakes

6.3.1 Finite fault model

The Kii-oki earthquake sequence has two large intraplate events whose magnitudes exceed $M7$, i.e., foreshock $M_{JMA}7.1$ (Sep. 5, 10:07 UTC) and mainshock $M_{JMA}7.4$ (Sep. 5, 14:57 UTC) (Figure 6-3a). There are several studies in which the source models were estimated. However, while the northern-dipping fault with the strike parallel to the trough was consistently estimated for the foreshock (e.g., Bai et al., 2007; Park and Mori, 2005; Yagi, 2004), the source model for the mainshock has less consistency. Whereas Yamanaka (2004) and GSI (2005) estimated the southwestern-dipping fault with the strike perpendicular to the trough, Bai et al. (2007) and Park and Mori (2005) estimated the southern-dipping fault with the strike parallel to the trough. Using the offshore tsunami wave records obtained by ocean bottom pressure gauges and a GNSS buoy, Saito et al. (2010a) estimated the fault mechanisms consistent with those of Yamanaka (2004). We determined the faults by trial and error to reproduce both of the GNSS and the GNSS-A results using the dislocation model of Okada (1992), referencing Bai et al. (2007) and Yamanaka (2004) for the foreshock and mainshock, respectively (Table 1, Figure 6-4). A water depth correction of 2 km was made when calculating the displacements at the seafloor sites by shallowing the depth of the fault (Iinuma et al., 2015). Onshore displacements were calculated by comparing daily position averaged over 15 days before and after the events, using the F3 solution of GEONET sites fixed to the Hyougo-Hidaka station (ID 960646, Figure 6-3a). Nevertheless, it should be acknowledged that the resolution of the fault slip model is limited by the current one-sided spatial coverage of the geodetic sites. Using the same input geodetic data, two independent studies produced significantly different fault parameters, including the strike direction (Kido et al., 2006; Tadokoro et al., 2006).

6.3.2 Viscoelastic relaxation

A schematic picture of the viscoelastic structure is shown in Figure 6-3b. The tetrahedral finite element mesh with the dimensions of 550 km × 600 km × 200 km was generated by

the open source software LaGriT v3.2 (available at https://lagrit.lanl.gov). The mesh contains approximately 25,000 elements. Whereas the displacements on the top surface were not constrained, the normal displacements on the side walls and bottom surface were constrained to zero. Since several GNSS-A sites near the source region are located at the depth of about 2 km in the Kumano basin, the top surface included a kink of 2 km between the land and ocean side to approximately reflect the bathymetry. For the subducting slab, we referenced the HBN geometry. The oceanic slab and continental plate were assumed as elastic bodies with a rigidity of 48 GPa. We tested three patterns for the thickness of the continental plate, i.e., D_c = 20, 30, and 40 km. The thickness of the oceanic slab was fixed to 40 km as inferred from the electrical conductivity model in the Shikoku Basin, northern part of the PHS plate near the Nankai Trough (Baba et al., 2010). According to them, the partially molten rock can exist at the depth of 40–80 km, which is also consistent with the sharp reduction of the shear velocity at the lithosphere-asthenosphere boundary observed in the central part of the PHS plate (Kawakatsu et al., 2009). Because partially molten polycrystals have five times smaller viscosity than at the sub-solidus temperature in the steady state (Takei and Holtzman, 2009), the layer can be considered to have weaker rheology in the asthenosphere. In addition, Yamauchi and Takei (2016) had pointed out that the polycrystals at the sub-solidus but near-solidus temperature also show the sharp reduction of the shear wave velocity and the gradual reduction of viscosity to the super-solidus temperature. Therefore, it is possible to make an assumption that the weak layer lies below the oceanic slab even if there is no direct evidence for the melt. The thickness of the weak layer was fixed to 40 km because it is difficult to resolve both the thickness and the viscosity of the weak layer from the geodetic data (e.g., Hu et al., 2016).

The weak layer, the oceanic mantle, and the mantle wedge were assumed as bi-viscous Burgers materials (Figure 6-3c). The Maxwell and Voigt rigidities of these materials were fixed to 64 GPa. We used the same viscosity for the oceanic mantle and the mantle wedge, the Maxwell viscosity η_m^M and the Voigt viscosity η_m^V, but the lower viscosity for the weak layer, the Maxwell viscosity η_w^M and the Voigt viscosity η_w^V. The ratio of the Voigt viscosity to the Maxwell viscosity was fixed to 0.1. We fixed Poisson's ratio and density to 0.25 and 3.4×10^3 kg/m^3 for the entire domain. We then tested three rheological parameters within the ranges as follows; D_c = 20–40 km, $\eta_m^M = 1.0 \times 10^{19}$–$6.0 \times 10^{19}$ Pa · s, and $\eta_w^M = 5.0 \times 10^{17}$–$5.0 \times 10^{18}$ Pa · s.

The viscoelastic response after these events was calculated using Pylith v2.1.4 (Aagaard et al., 2016; available at https://geodynamics.org/cig/software/pylith), which is an open source

FEM code for quasi-static and dynamic problems. The dislocations are imposed by adding zero-volume cohesive cells for each fault surface.

Estimated viscoelastic displacements for the time period between 1 and 2 years after the earthquakes are shown in Figure 6-5a. The time series of the viscoelastic displacements at the ith site, $\boldsymbol{d}_i^{FEM}(t)$ were compared with the observed displacements, $\boldsymbol{d}_i^{obs}(t)$. Because a slow slip event occurred in the period of 2000–2005 in the Tokai region (e.g., Suito and Ozawa, 2009; Ochi and Kato, 2013), we selected several GEONET sites in the Kinki district including the Kii Peninsula to compare with the FEM models (Figure 6-3a). The transient displacements were derived by removing the pre-quake trend (for 2 years before the Kii-oki earthquakes, i.e., 2002.09–2004.09). The horizontal differences of the pre-quake trend from the pre-SSE trend (1998.01–2000.01) at these sites were up to 2 mm/year.

6.3.3 Afterslip estimation

The residuals, $\boldsymbol{d}_i^{resi}(t) = \boldsymbol{d}_i^{obs}(t) - \boldsymbol{d}_i^{FEM}(t)$, should indicate the displacements due to afterslip, $\boldsymbol{d}_i^{as}(t)$. They are usually approximated by a logarithmic function with single time constant; $\boldsymbol{d}_i^{as}(t) = \boldsymbol{A}_i \log(1 + (t - t_0)/t_r)$, where t_0 and t_r indicate the occurrence time of the mainshock and relaxation time of the afterslip, respectively. Because t_r is independent of the station, we first determined it from the sum of the horizontal residuals, $\boldsymbol{d}_i^{resi}(t)$, of the first 2-years of data at all the selected sites (Table S2 of Watanabe et al., 2018). We then estimated the amplitudes for each site, $\boldsymbol{A}_i^{resi}$ (black arrows in Figure 6-5b). We assumed that the spatial variation of $\boldsymbol{A}_i^{resi}$ has coherence with the elastic deformation pattern of the dislocations on the surrounding faults. We assumed that afterslip occurred on the following three rectangular faults; the downdip extent of the faults for the foreshock (AF1d) and the mainshock (AF2d), and the western extent of the foreshock (AF1w) (Figure 6-5b), whose rake angles were the same as the neighboring faults. Non-negative slip amount on each fault was estimated using the least squares method. We then evaluated the postseismic model by calculating the weighted χ^2 misfit between $\boldsymbol{A}_i^{resi}$ and the spatial pattern of the afterslip estimated from the dislocation model, $\boldsymbol{A}_i^{est}$ (pink arrows in Figure 6-5b):

$$\chi^2 = \frac{1}{N - 1 - dof} \sum_i \frac{\left|\boldsymbol{A}_i^{resi} - \boldsymbol{A}_i^{est}\right|^2}{\sigma_i^2}$$

where N, dof, and σ_i^2 indicate the number of sites, the degrees of freedom, and the pre-quake variance of the GNSS observation (2002.09–2004.09), respectively. In this study, dof = 6 (3 for the FEM model, and 3 for the afterslip model). The calculated χ^2 misfit values are

summarized in Table S2 and Figure S2 of Watanabe et al. (2018). The preferred model with the least χ^2 misfit was obtained for D_c = 40 km, $\eta_m^M = 4.0 \times 10^{19}$ Pa·s, and $\eta_w^M = 1.0 \times 10^{18}$ Pa·s (Figure 6-5, and Table S2 and Figure S2 of Watanabe et al., 2018). The relaxation time of afterslip for the preferred model was t_r = 19.23 day. In our modeling it was apparent that the data could hardly resolve afterslip on AF1d and AF2d. Eastward residuals around Kushimoto required relatively large afterslip on AF1w in the preferred model. Its equivalent moment magnitude was 7.0 for the first two years, though it was much higher than expected for typical afterslip following $M7$-class events. This feature might be due to the limitations in deriving the postseismic model only from the far-field and one-sided geodetic data, the simplified rheological properties, and insufficient resolution in the coseismic models.

We removed both the viscoelastic and afterslip effects from the GNSS-A data before deriving the seafloor velocities by linear fitting with a robust regression method (M estimation method) with Turkey's bi-weight function (Figure 6-6, and Table S3 and Figure S3 of Watanabe et al., 2018). Because the estimation errors for the horizontal component at KME were more than 1.5 cm/year (95% confidence level), we disregarded the seafloor velocity at KME. The onshore velocities were derived by calculating the linear trend between 2006/07/01 and 2009/07/01 after removing the viscoelastic and afterslip effects (Table S4 of Watanabe et al., 2018). The velocities were calculated as the relative velocities with respect to the Nankai block (forearc sliver) of Loveless and Meade (2010), in order to remove the deformation on other tectonic boundaries such as the Median Tectonic Line (MTL).

6.4 Results

6.4.1 Slip deficit rate distributions

The distributions of estimated slip deficit rate are shown in Figure 6-7. The slip deficit rate reaches 6 cm/year. Three segments with the slip deficit rate of more than 5 cm/year were clearly estimated for the HBN geometry (Figure 6-7b); (A) off the Shikoku Island to the trough axis, (B) near the trough axis off the Kii Peninsula, and (C) near the trough axis off the Cape Omaezaki. In the case of the CAMP, the segments (A) and (B) seemed to be combined and form the larger segment. The slip deficit off the Cape Muroto, the region between the segments (A) and (B), for the HBN was small because the HBN has a shallower fault due to the subducting seamount. On the other hand, smaller slip deficit was estimated in the eastern region, segment (C), for the CAMP. This is caused by the smaller dip angle of the CAMP geometry in this region.

For the comparison, differences of the distributions of slip deficit rate estimated by the

velocities with and without removing the postseismic effects of Kii-oki earthquakes are shown in Figure S4 of Watanabe et al. (2018). The results with postseismic correction had larger slip deficit of up to 0.5–0.6 cm/year in the Kumano Basin. Due to the zero-slip constraint on the downdip edge, the backslip rate beneath the Shikoku Island sharply decreased to zero. Figure S5 of Watanabe et al. (2018) shows the case for the free boundary on the downdip edge, indicating that this feature is not well resolved. In addition, we performed checkerboard resolution tests for the inversion analysis. Imposed backslip rate in the tests was 4 cm/year, and errors with standard deviations of 1.5 mm/year and 7.5 mm/year were added for each GNSS and GNSS-A synthetic data, respectively. The results are shown in Figures S6 and S7 of Watanabe et al. (2018), which indicate that patches of approximately 250 km square can be well resolved.

6.4.2 Tsunami propagation

The calculated distributions of uplift including the horizontal effect due to the geographical slope after instantaneous releasing the 100-years of slip deficit are shown in Figure 6-8. The equivalent moment magnitude for both models was M_w8.9. The results indicate that the seafloor throughout the area would lift the seawater by 4–5 m. While the area with more than 1 m uplift was broadly distributed for the CAMP, the uplift was strongly concentrated into the near-trough region for the HBN. That is because the dip angle of the HBN geometry near off the Shikoku Island was shallower than the CAMP, in contrast to the eastern edge of the Nankai Trough.

Calculated tsunami wave patterns are shown in Movies S1–S4 of Watanabe et al. (2018). The maximum tsunami amplitudes calculated using 30 arcseconds topography are displayed in Figure 6-9. The results with the HBN show higher tsunami amplitudes along the Pacific coast, except in the eastern Shikoku Island. The tsunami wave forms at several points are shown in Figure 6-10. Although more than 2 m height of tsunami wave was calculated at around 50 min. at Tosa-Shimizu (Figure 6-10b) for both geometries, the earlier additional 2 m peak at around 30 min. was seen only for the HBN. While the two waveforms are similar at Shimotsu (Figure 6-10c) and Irago (Figure 6-10d), initial ground subsidence heightens the relative tsunami peak in the case of the HBN. At Omaezaki (Figure 6-10e) and Yaizu (Figure 6-10f) located near the easternmost part of the Nankai Trough, the HBN model indicated increased tsunami heights, due to the larger slip deficit rate for the HBN, which causes higher initial water lift in the Suruga Bay than for the CAMP model.

6.5 Discussion

Although the distributions of slip deficit rate derived in this study were consistent with the results by Yokota et al. (2016), we proposed several improvements in the interseismic model. By applying the block model; (1) a smaller and more realistic slip deficit rate was estimated, especially in the off Tokai region (easternmost part), where the earlier model had the larger slip deficit rate than the subducting oceanic plate; and (2) the artificial peaks of the slip deficit rate, which appeared on the downdip side (beneath the Lake Biwako and the Bungo channel) in the earlier model, were reduced. Such artifacts should be removed because they may lead to the overestimation of tsunami initiation.

By removing the postseismic deformation of the Kii-oki earthquakes, the slip deficit rate in the Kumano Basin was increased by up to 10%. However, the postseismic model has uncertainties due to the complexity of its coseismic sequence, which may not be resolved by the poor near-field geodetic/seismic observations at that time. Nonetheless, postseismic effects on backslip estimation including its uncertainty will decrease with time. With regard to the viscoelastic modeling, whereas the postseismic effects of the recent earthquakes were corrected, this study disregarded the viscoelastic relaxation of stress caused by the interseismic fault locking (e.g., Wang and Tréhu, 2016) because of technical difficulties and complexity in deriving the Green's functions for interseismic velocities due to the computational costs. On this point, this study certainly has the limitation in deriving the slip deficit rate. Yet in the future work, the interseismic modeling with the viscoelastic behavior is expected to be addressed. For this purpose, our study on the postseismic modeling of the Kii-oki earthquakes will contribute to the understandings of the rheological properties beneath the Nankai Trough.

By comparing the backslip distributions with the different geometries of the plate interface, we found that the HBN geometry provides the smaller slip deficit in the off-Muroto region, where a seamount subducts beneath the continental plate. It divides the region with large slip deficit rate into lateral segments. For the along-dip distribution, the regions with large slip deficit rate are concentrated in the shallow portion in the HBN case, which causes the steep tsunami initiation along the trough axis (Figure 6-8). As a result, higher tsunami waves are shown in the case of the HBN rather than the CAMP at most gauges in the bay especially in the eastern region. These results also indicate that the tsunami initiation along the trough strongly depends on the depths of the fault. Thus, the precise detection of the location and geometry of the seismogenic faults is important for the tsunami prediction.

For further discussions, the block model itself is still capable of improvement, especially in the offshore region, e.g., the segmentation in the forearc sliver including the splay faults. As discussed by Wang and Tréhu (2016), various rupture scenarios in the shallowest portion can be considered in the megathrust earthquakes. Along the Nankai Trough, well-developed splay fault lies in the Kumano Basin (Moore et al., 2007). Due to its higher dip angle, it could generate a larger tsunami. For the tsunamigenesis, it is an essential problem whether the splay fault in the Kumano Basin could rupture. In this region, there have been deployed the various geophysical instruments such as pressure gauges, borehole observatories, and seafloor seismometers, as well as coring and seismic imaging surveys. These observations enabled researchers to detect the occurrence of slow slip events (e.g., Araki et al., 2017; Suzuki et al., 2016). GNSS-A campaign observations, which can be directly compared with the kinematics of the incoming plate, have also been carried out across the splay fault and the trough. Yasuda et al. (2017) showed the first results of the GNSS-A seafloor velocities across the trough with the precision of several centimeters per year (95% confidence level). Their continuous efforts on improving the accuracy of GNSS-A observations are expected to help resolve the features in the frontal prism.

Direct observations of the convergence rate on the subducting plate near the trough can be used to derive the coupling coefficient in the shallow portion. In the eastern part, for instance, we have a few geodetic data across the trough and an out-of-sequence thrust. The JCG had carried out the GNSS campaign observation during the period of 2000–2005 at the Zenisu reef, which is located on the subducting PHS plate. We reprocessed these data using the open source software RTKLIB v2.4.2 (Takasu, 2013; available at http://www.rtklib.com/) in the static PPP (Precise Point Positioning) mode. The velocity was derived from the data between 2000.11 and 2004.07 (Figures 6-6 and 6-11, and Table S1 of Watanabe et al., 2018), because the campaigns in 2000.08 and after 2004.09 were possibly affected by the volcanic events in the northern Izu islands (e.g., Nishimura et al., 2001) and the transient slip in the Izu-Bonin arc (Arisa and Heki, 2016), respectively. The velocity of 4.6 cm/year toward the west was comparable with the velocity of 4.7 cm/year toward the west at TOK1. The observation that little shortening had occurred between these sites suggests two hypotheses; (1) that the plate boundary in the eastern Nankai Trough is fully coupled as suggested in this study, and/or (2) that the seismogenic faults, i.e., the coupled tectonic boundary, are located landward of the TOK1, such as the eastern margin of the out-of-sequence thrust (the Tokai thrust) (e.g., Figure 2 of Kawamura et al., 2009).

There remain several uncertainties and limitations in modeling the coseismic processes.

First, it should be noted that estimated slip deficit rate gives only the first order approximation, since the temporal variation of the slip deficit rate are not considered in this model. To resolve them, the frequency and the accuracy of the GNSS-A observations should be improved. Second, we showed only two of the simplest scenarios with the geodetic prior information, where the recurrence time of the past earthquakes are not taken into account. Additional information such as records of earthquakes in each segment (e.g., Ando, 1975) as well as the remaining slip deficit from the last events (e.g., Nocquet et al., 2016) should be considered for more realistic coseismic rupture scenarios. Third, plate coupling model should be derived based on the concept of mechanical coupling (e.g., Herman et al., 2018; Noda et al., 2021). In such cases, however, it should also be investigated how the faults with "apparent" backslip behaves during the coseismic phase, because the coseismic slips would propagate to the outsides of the mechanically coupled faults.

On the other hand, there may be smaller tsunami generation, when the slip deficit is released as afterslip, rather than coseismic slip, especially in the shallow portion. Simultaneously, the finer topologies including breakwaters should be available when calculating tsunami propagation, especially for the runup modeling. Tidal changes in seawater level should also be considered for more appropriate prediction.

6.6 Conclusions

In this study, we improved the model of the slip deficit rate in the Nankai subduction area, southwestern Japan, by deriving the postseismic deformation model of the Kii-oki earthquakes, in terms of viscoelastic relaxation and afterslip as well as introducing a better alignment with the tectonic block model. The postseismic effect, which leads to about 10% of underestimation in the uncorrected models, was removed though it has some limitations due to the uncertainty of its coseismic sequence and rheological properties.

We derived tsunami wave propagation models based on the geodetically-derived distribution of slip deficit rate using two different plate interface geometries. The differences between the two models indicate the importance of identifying fault locations and geometries. The location of the downdip edge of the coseismic rupture is essential to determine whether the coastal area would subside or not. From the point of view of disaster prevention, subsidence at the southern coast seen in the HBN case would heighten the tsunami runup distance (e.g., at gauges in Shimotsu and Irago).

Other uncertainties in our model should also be considered. The interseismic slip deficit

model can be improved by including viscoelastic modeling. Temporal variations could be resolved by more frequent or continuous GNSS-A measurements with higher accuracy. Precise geodetic observations and geological surveys in the wider region would be helpful for a better understanding of the behavior in the frontal prism during coseismic slip. These improvements should result more reliable tsunami scenarios in the Nankai Trough region.

Table 6-1. Fault parameters for the foreshock and mainshock of the 2004 Kii-oki earthquake sequence (after Watanabe et al., 2018).

	longitude latitude	depth [km]	length [km]	width [km]	strike [°]	dip [°]	rake [°]	slip [m]	M_w
fore-shock	136.957 °E 32.864 °N	5.4	35	20	-80	40	114	2.13	7.2
main-shock	136.613 °E 33.463 °N	5.4	65	25	122	44	120	2.19	7.4

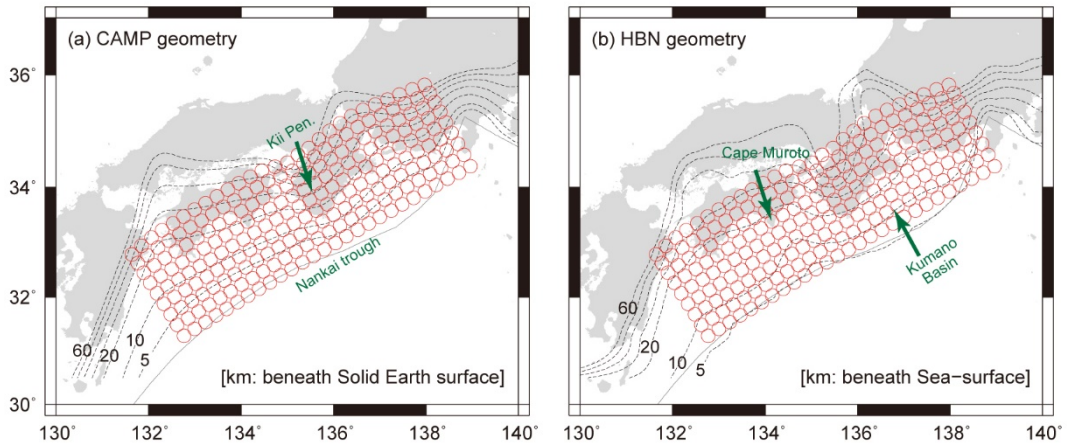

Figure 6-1. Slab depth contours of the plate interface for (a) the CAMP geometry and (b) the HBN geometry (dotted lines). Contours at 5 km depth and every 10 km in the range of 10–60 km are shown. The references of the depth for the CAMP and HBN geometries are the solid Earth surface and the sea surface, respectively. Red circles indicate the location of the subfaults used for the slip deficit inversion. The figure is adapted from Watanabe et al. (2018).

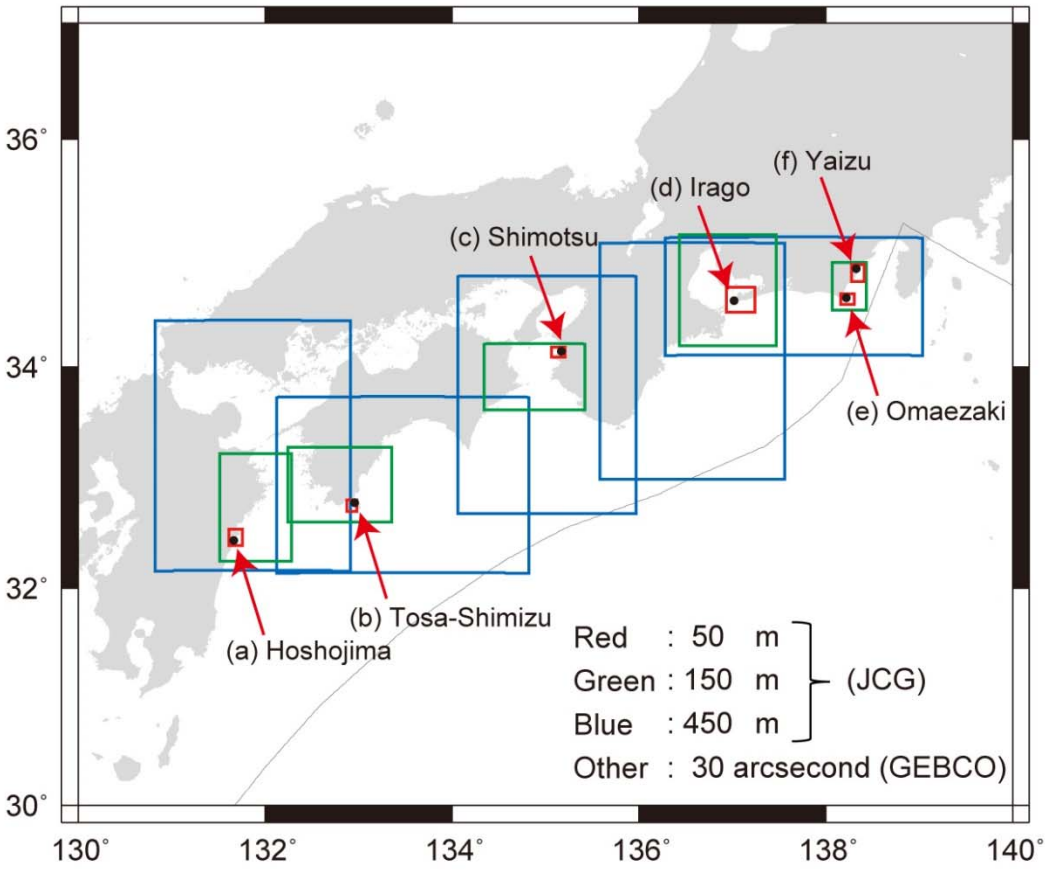

Figure 6-2. Topography for the tsunami propagation model. Red, green, and blue rectangles indicate regions of 50 m, 150 m, and 450 m mesh resolution, respectively. Otherwise, the topography has a resolution of 30 arcseconds. Black circles indicate the locations of the points where the tsunami time series are shown in Figure 6-10. The figure is adapted from Watanabe et al. (2018).

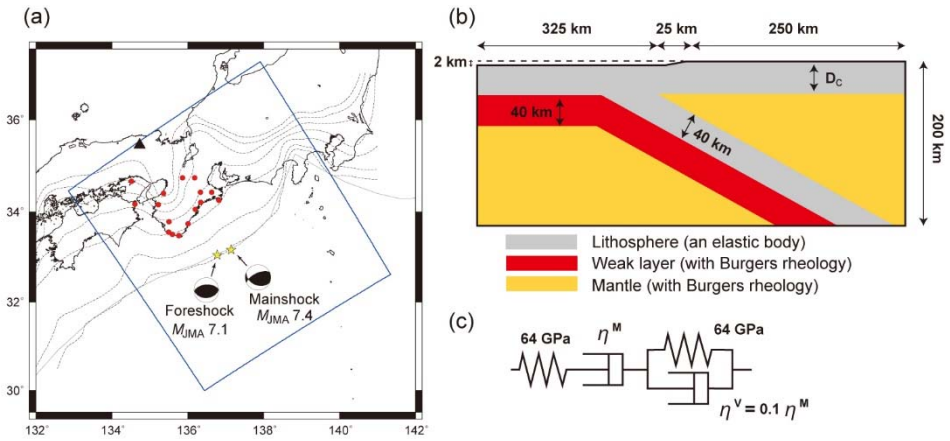

Figure 6-3. (a) Region of the FEM model (blue rectangle). The epicenters of the foreshock and the mainshock of the 2004 Kii-oki earthquake sequence are indicated as yellow stars with the centroid moment tensor solutions determined by the National Research Institute for Earth Science and Disaster Prevention (NIED). Red circles indicate the location of the GEONET sites used to compare with the FEM results. Black triangle indicates the Hyougo-Hidaka station (ID 960646), used as the reference site. Dotted contours indicate the plate interface depths of the HBN geometry. (b) Cross section for the schematic FEM structure. Gray, red, and orange regions indicate the elastic lithosphere/slab, the weak layer, and the mantle, respectively. The top surface had a kink to reflect the water depth in the Kumano Basin. The weak layer and the mantle have the linear viscoelastic property modeled by (c) the bi-viscous Burgers rheology. The figure is adapted from Watanabe et al. (2018).

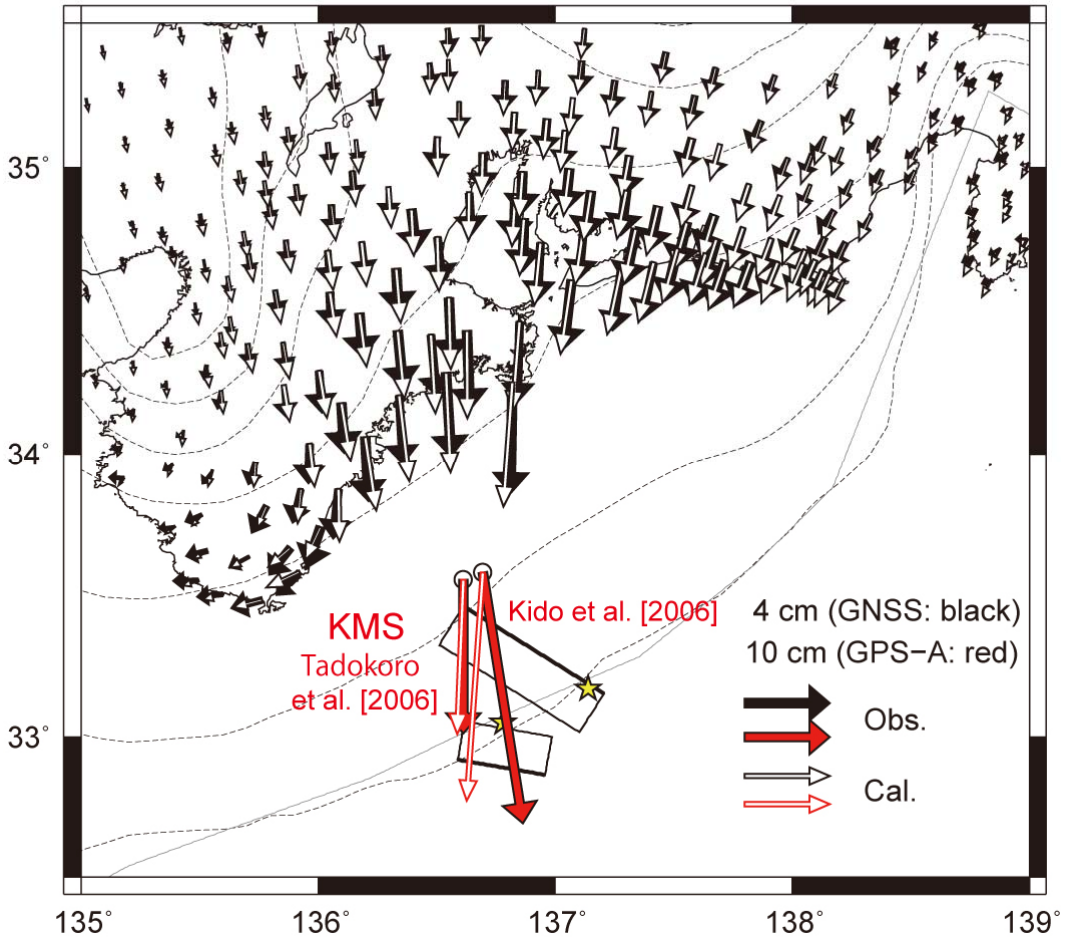

Figure 6-4. Horizontal coseismic displacements associated with the Kii-oki earthquakes. Solid and open arrows indicate the observed and calculated displacements at the GEONET sites (black) and the GNSS-A sites (red), respectively. Note that the length scales for the GEONET and GNSS-A sites are different. Yellow stars indicate the epicenter of the foreshock and mainshock of the Kii-oki earthquake sequence. Black rectangles indicate the finite faults estimated in this study, whose updip sides are indicated by the thick lines. The figure is adapted from Watanabe et al. (2018).

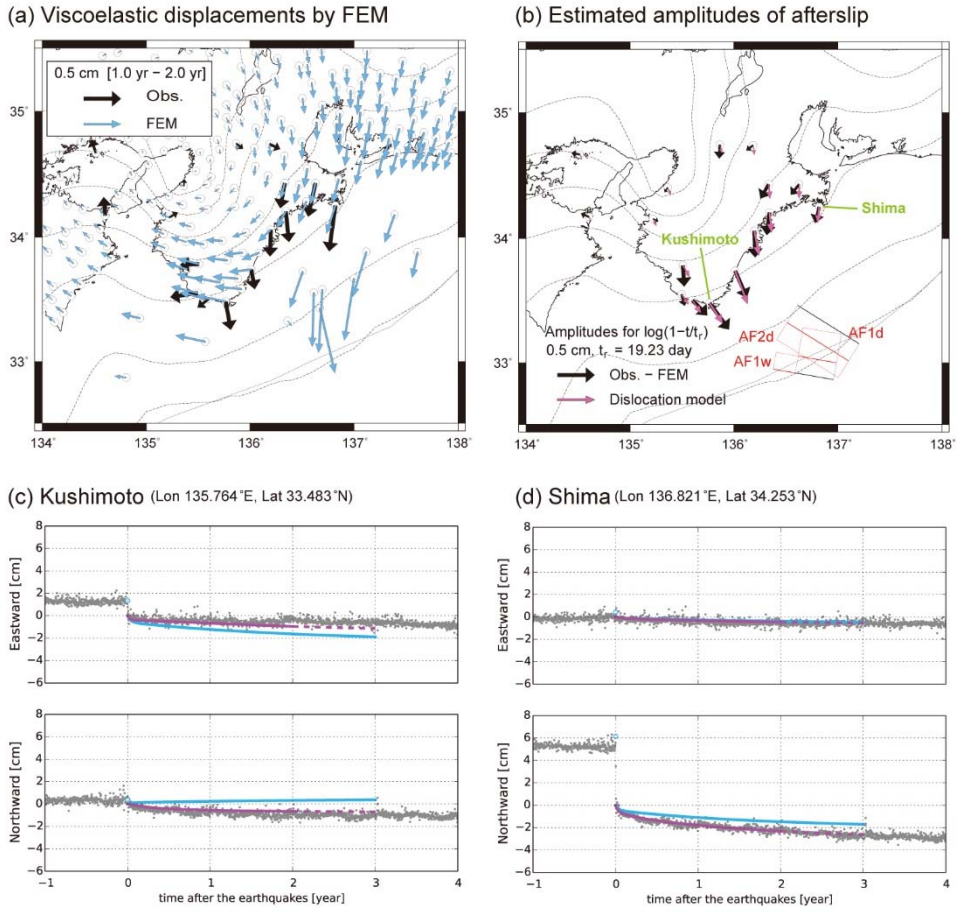

Figure 6-5. (a) Viscoelastic displacements for the time period between 1 and 2 years after the earthquakes estimated with FEM for the preferred model (blue arrows). Black arrows indicate the observed displacements in the same period. (b) Spatial pattern of horizontal amplitudes of afterslip, $\boldsymbol{A}_i^{resi}$ (black arrows) and $\boldsymbol{A}_i^{est}$ (pink arrows) for the preferred model. In this panel, only the effects of afterslip are shown. Red and black rectangles indicate the finite faults, whose updip sides are indicated by the thick lines, for the afterslip (AF1d, AF2d, and AF1w) and the coseismic dislocation, respectively. Time series of the displacement at GEONET site (c) Kushimoto and (d) Shima are displayed. Gray dots, blue lines, and pink lines indicate the observed displacements, only the viscoelastic displacement by FEM, and the sum of the viscoelastic and the afterslip model, respectively. Because the afterslip fittings were estimated from the data between 0–2 years, the extrapolated values for years 2–3 are shown as dashed pink lines. The figure is adapted from Watanabe et al. (2018).

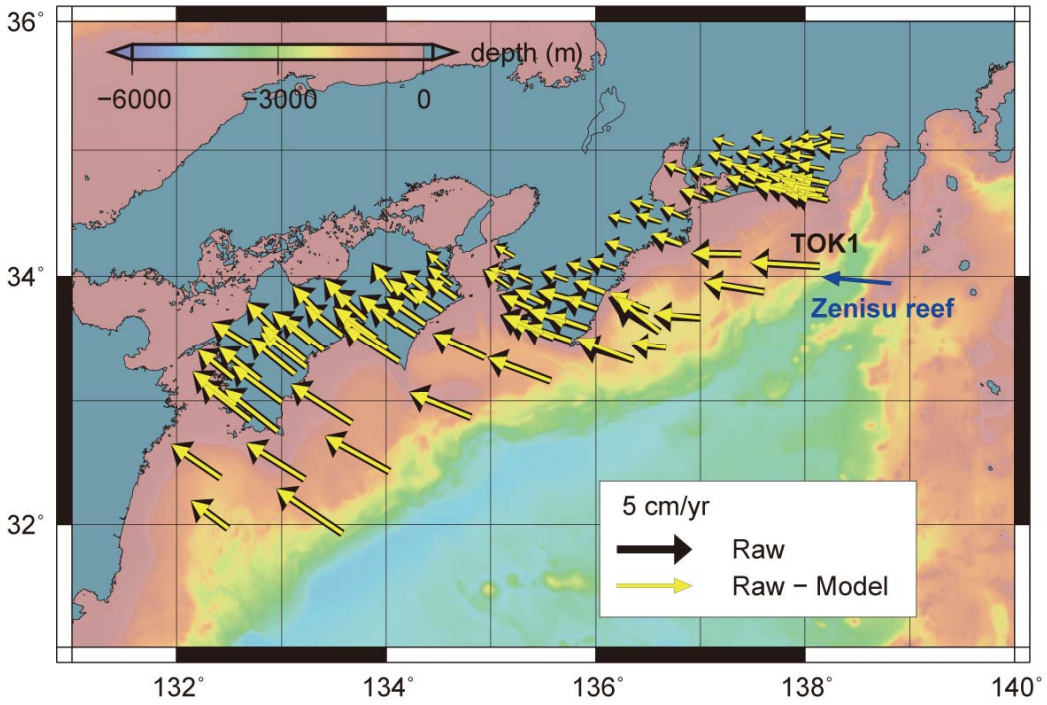

Figure 6-6. Velocities at GNSS-A sites (period: 2004–2016) and GNSS sites (period: July 2006 – July 2009) with respect to the Nankai block derived from the corrected (yellow arrows) and uncorrected (black arrows) time series. Blue arrow indicates the velocity at the Zenisu reef, which is located on the incoming plate, derived from the campaign observations between 2000 and 2004. Bathymetric data of the GEBCO_2014 Grid (30 arcseconds) are shown as color contours. The figure is adapted from Watanabe et al. (2018).

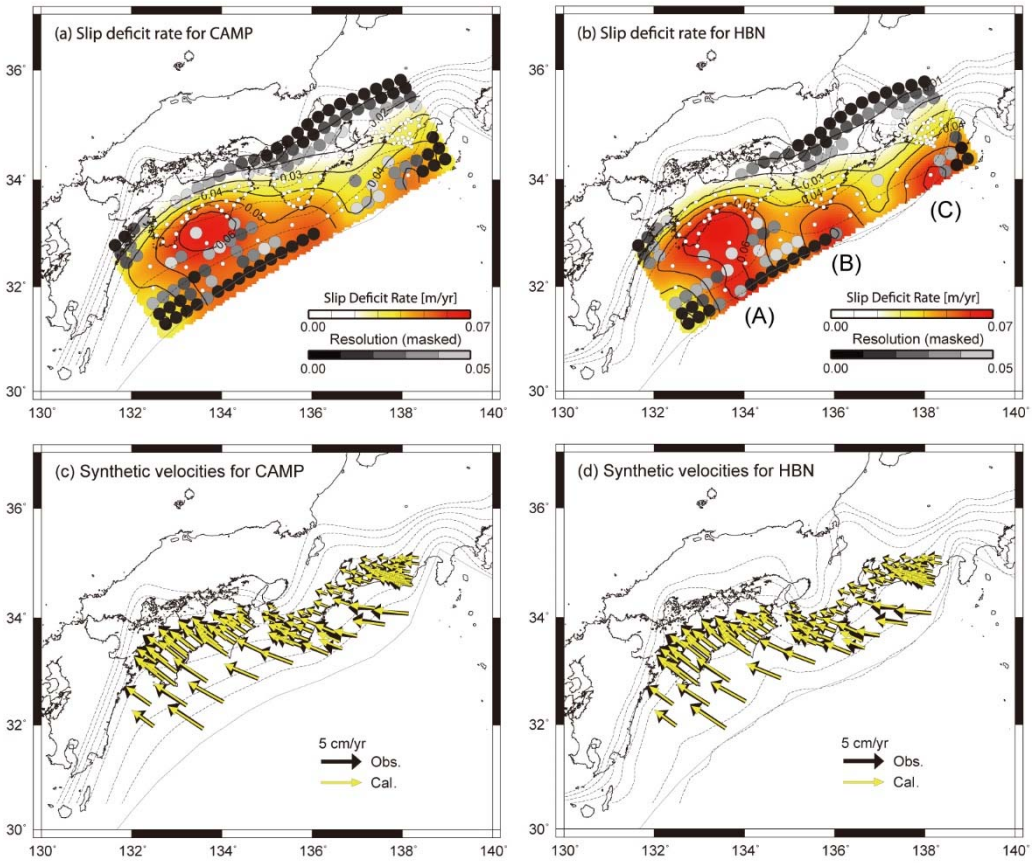

Figure 6-7. Distributions of slip deficit rate estimated for (a) the CAMP geometry and (b) the HBN geometry. White circles indicate the location of the geodetic sites. The regions with less resolution (<0.05) are masked by gray circles. (c) and (d) Observed (black arrows) and calculated velocities (yellow arrows) at each site for the CAMP and HBN geometries, respectively. Regions (A)–(C) in panel (b) indicate the lateral segmentation of high slip deficit rate. The figure is adapted from Watanabe et al. (2018).

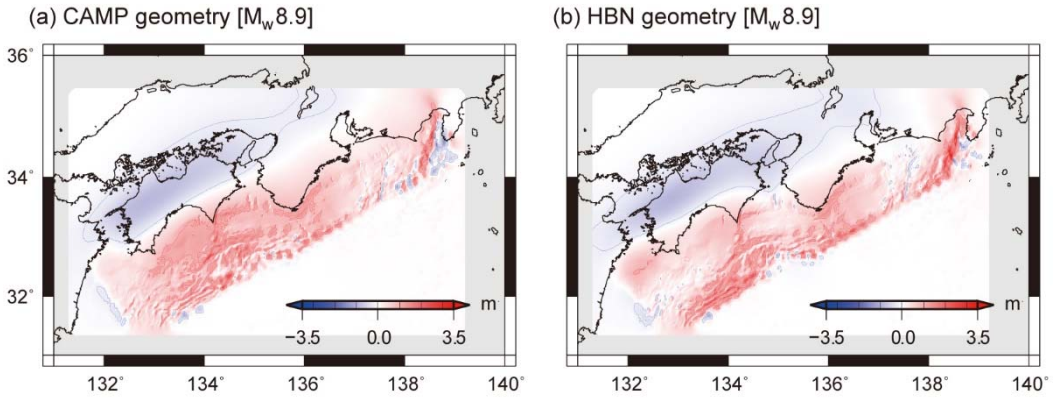

Figure 6-8. Distributions of seawater lift and vertical motion on land due to the release of the 100-year backslip for (a) the CAMP geometry and (b) the HBN geometry. Red and blue lines show the +1.0 m and –0.2 m contours, respectively. The figure is adapted from Watanabe et al. (2018).

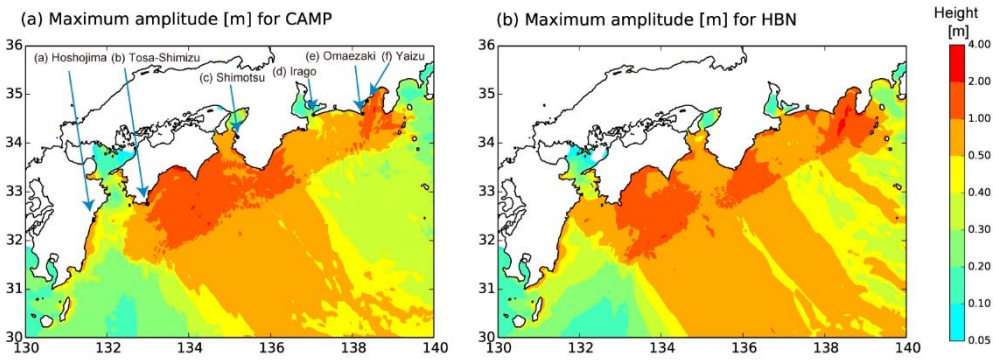

Figure 6-9. Maximum tsunami amplitudes for (a) the CAMP geometry and (b) the HBN geometry by 2 hours after the earthquake. The amplitudes were calculated at a resolution of 1 arcminute. The figure is adapted from Watanabe et al. (2018).

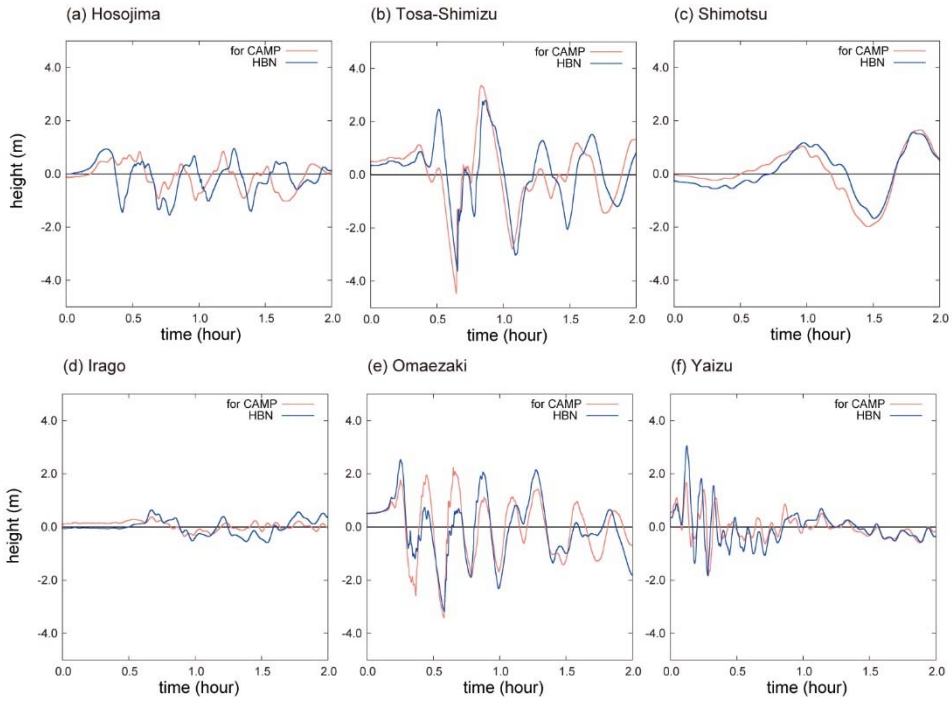

Figure 6-10. Time series of sea-surface height at each point near the harbor for the CAMP geometry (pink lines) and the HBN geometry (blue lines). The figure is adapted from Watanabe et al. (2018).

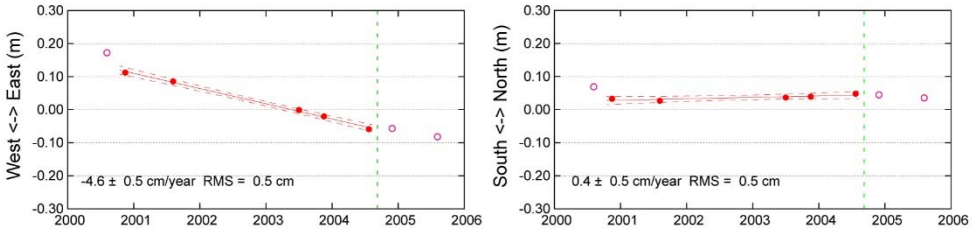

Figure 6-11. Time series of displacement at the Zenisu reef. The velocity was derived from data collected during 5 campaign GNSS observations between November 2000 and July 2004 (solid circles). The linear trends and the 95% two-sided confidence intervals are shown with red solid and dotted lines, respectively. Green lines indicate the occurrence time of the Kii-oki earthquake sequence. The figure is adapted from Watanabe et al. (2018).

Chapter 7

Postseismic deformation along the Japan Trench following the 2011 Tohoku-oki earthquake

---

Almost all part of this Chapter references the author's work published as Watanabe et al (2021d), which contains the advanced discussion based on the author's earlier work published as Watanabe et al. (2014).

References:

Watanabe, S., Sato, M., Fujita, M., Ishikawa, T., Yokota, Y., Ujihara, N., and Asada, A. (2014) Evidence of viscoelastic deformation following the 2011 Tohoku-oki earthquake revealed from seafloor geodetic observation. Geophys. Res. Lett., 41, 5789–5796. doi:10.1002/2014GL061134

Watanabe, S., Ishikawa, T., Nakamura, Y., and Yokota, Y. (2021d) Co- and postseismic slip behaviors extracted from decadal seafloor geodesy after the 2011 Tohoku-oki earthquake. Earth Planets Space, 73, 162. doi:10.1186/s40623-021-01487-0

7.1 Background

In general, a large fault rupture is followed by postseismic relaxation processes such as viscoelastic relaxation in the asthenosphere and aseismic slip on the fault plane, which lead to transient crustal deformation on the solid Earth's surface (e.g., Wang et al., 2012).

Postseismic geodetic data following a megathrust earthquake show the sum of these relaxation processes and deformation caused by interplate coupling due to the secular plate subduction. Along the Japan Trench, postseismic processes were triggered by the 2011 Tohoku-oki earthquake (M_w 9.0) and continue in this decade. Clarifying the interplate slip behaviors for the co- and postseismic phase will contribute to the understanding of the frictional state of faults, slow earthquake activities, and seismic cycles in this region.

The Tohoku-oki earthquake caused trench-ward seafloor displacements of several tens of meters (Sato et al., 2011; Kido et al., 2011), reaching about 50 m at the trench (Fujiwara et al., 2011). Using seafloor geodetic data (Sato et al., 2011; Kido et al., 2011), an extremely large slip was estimated at the plate interface shallower than the hypocenter (Figure 7-1) (e.g., Ozawa et al., 2012; Iinuma et al., 2012). Except for the north-south extent of the shallow rupture, which could not be resolved by the geodetic data at that time, a consensus has been reached on the north-south rupture propagation at depths near the hypocenter, where almost all of the fault models produce similar results (summarized by Sun et al., 2017; Wang et al., 2018; Lay, 2018; Uchida and Bürgmann, 2021). This implies that the rupture in 2011 did not progress to the northern region (> 39 °N), even though M_w 8 earthquakes have historically occurred in this region (Figure 7-1) (Nagai et al., 2001; Yamanaka and Kikuchi, 2004). Investigations of the postseismic behaviors, including the occurrence of afterslip, in the northern and southern regions outside the main rupture area provide useful information on how rupture propagation may have been restrained in a compact region in the depths near the hypocenter.

For the detection of transient postseismic crustal deformation to decompose the elementary processes, sufficiently long-term, high-frequency, and well-distributed geodetic data are required because these sources have different decay times and deformation patterns (e.g., Wang et al., 2012). Although the terrestrial Global Navigation Satellite System (GNSS) observation network has an extremely high spatiotemporal resolution, it cannot easily decompose the transient processes because the two processes of interest cause similar trench-ward movements in the onshore regions and thus cannot be distinguished from one another. In contrast, the viscoelastic relaxation in the oceanic asthenosphere and the afterslip are expected to cause displacements in opposite directions on the seafloor above the main rupture, i.e., landward and trench-ward directions, respectively (e.g., Hu et al., 2016). Therefore, seafloor geodetic observations can be used to decompose transient deformation sources despite their lower temporal resolution compared to that of terrestrial observations. Actually, seafloor geodetic technique detected postseismic landward movements larger than the

subduction rate (~9 cm/year) (Argus et al., 2011) above the main rupture area, whereas terrestrial geodetic sites showed trench-ward movements. This is a conclusive evidence for the dominance of viscoelastic relaxation in the oceanic asthenosphere below the subducting plate on the postseismic deformation in the main rupture area (Watanabe et al., 2014; Sun et al. 2014; Hu et al., 2016; Tomita et al., 2017; Honsho et al., 2019).

The seafloor observation results stimulated researchers to develop postseismic deformation models incorporating the viscoelastic effects. Table 7-1 summarizes the postseismic models (1) referencing the seafloor geodetic data, (2) incorporating the afterslip models, (3) modeling the subducting cold slab, and (4) calculating the viscoelastic deformation in an area wider than the latitude range of 37–39 °N. Every model indicated that the deformation patterns in the main rupture area can be roughly explained as the viscoelastic response, but that the observed deformation outside of main rupture cannot be reproduced only by viscoelastic relaxation. Hu et al. (2016) proposed a model where the afterslip effects are approximated as a viscoelastic flow in a thin layer whose locations are constrained by repeating earthquakes, which was yet insufficient to explain the vertical motions of the seafloor. Some models put additional afterslip patches in the offshore region to reproduce the geodetic data (e.g., Sun and Wang., 2015; Freed et al., 2017; Wang et al., 2018), even though these were only tentative models because of the insufficient spatiotemporal resolution and observation period (at most 5 years) of available seafloor data.

On the other hand, there remains the uncertainty in some coseismic dislocation input for the postseismic deformation modeling. Many researchers had adopted coseismic slip distribution models inverted from seafloor and terrestrial coseismic geodetic data with constraints of smooth slip distribution (e.g., Iinuma et al., 2012; Freed et al., 2017). However, the geodetic network in 2011 did not cover the whole source region, lacking information especially on the coseismic rupture in the shallower portion. Thus, it is important to consider seismic and tsunami waveforms, together with geodetic data (e.g., Lay, 2018; Uchida and Bürgmann, 2021). To visualize the difference, Figure 7-1 displays both the geodetically- and tsunami-derived slip distributions (Iinuma et al., 2012 and Satake et al., 2013, respectively). Tsunami data, which are sensitive to topographical changes of the seafloor, indicate that the tsunamigenic area was extended, especially in the northern (> 39 °N) and southern (~37 °N) areas along the trench (Figure 7-1) (Satake et al., 2013). This feature does not appear in geodetic inversion due to the absence of data. Such difference in the coseismic input would affect the coseismic stress-change field and the postseismic relaxation processes. For instance, Agata et al. (2019) proposed a viscoelastic model using coseismic slip distribution derived

from seismic cycle simulation (Nakata et al., 2016). The coseismic input included an additional shallow slip near the trench eastern off-Fukushima (~37 °N). Their model showed significant seafloor deformation in the off-Fukushima region caused by viscoelastic relaxation, whereas other models based on geodetic coseismic input could not induce enough stress to cause such significant viscoelastic deformation in this region (e.g., Sun et al., 2014; Freed et al., 2017). The difference between the models suggests that we will be able to estimate shallow coseismic slip behavior and following postseismic models by decomposing and discussing the postseismic deformation sources with longer-term seafloor geodetic data, as discussed in Tomita et al. (2020). Some researchers took a different approach to estimate coseismic distribution by constraining their models with postseismic data (e.g., Yamagiwa et al..2015; Tomita et al., 2020; Fukuda and Johnson, 2021).

In this study, decadal seafloor geodetic data that contain the temporal evolutions of surface velocity are used to decompose the deformation sources. Based on the results, we clarify the co- and postseismic slip behaviors in the northern and southern parts of the source region.

7.2 Data and method

To investigate the temporal evolution of seafloor crustal deformation, the Japan Coast Guard (JCG) regularly performs seafloor geodetic observations using GNSS – acoustic ranging combined seafloor positioning system (GNSS-A) (Figure 7-2), in the Japan Trench region (e.g., Watanabe et al., 2020c). GNSS-A data were obtained at six JCG sites (KAMN, KAMS, MYGI, MYGW, FUKU, and CHOS; Table 7-2) from March 2011 to June 2020 using survey vessels, and were processed with GARPOS v1.0.0 (Watanabe et al., 2021e, Chapter 4). Note that the present analysis method, which incorporates the estimation process of horizontal gradients in the sound speed structure, has been applied to the previously published data (Watanabe et al., 2014). The JCG also performed GNSS-A observations at five sites (G08, G10, G12, G14, and G17; Table 7-2) installed by Tohoku University (TU) (Kido et al., 2015) since 2013, independently of TU. We additionally reprocessed the GNSS-A data before the Tohoku-oki earthquake at five JCG sites (Sato et al., 2013a) using the present analysis method to determine the preseismic seafloor velocities.

All GNSS-A data used in this study are available at Zenodo (Watanabe et al., 2021a; b). Note that the GNSS-A data before 2009 were obtained by the old “drifting observation” system, where the ship engine had to be turned off during the observation; thus, the ship track cannot be controlled (Figure 7-2a). The data obtained by the “drifting observation” system is less precise than the “sailing observation” system, where the ship moves along a planned track

(Sato et al., 2013b; Ishikawa et al., 2020).

To extract the annual-scale velocity changes, we took the following steps: We first subtract the effects of aftershocks that can cause coseismic displacement of more than 1 cm at seafloor sites (sources are shown in Figure 7-1) by applying the method of Okada (1992). We used the Centroid Moment Tensor (CMT) solution catalogue provided by the Japan Meteorological Agency, which are available online. We then smoothen the time series of postseismic displacements, $x(t)$, where t denotes the time after the event, by fitting with a function which is modified from the fitting function of Tobita (2016), i.e.,

$$x(t) = x_0 + vt + \alpha_1 \log\left(1 + \frac{t}{\tau_1}\right) + \alpha_2 \log\left(1 + \frac{t}{\tau_2}\right), \tag{7.1}$$

where x_0, v, α_1 and α_2 are estimation parameters. For the time constants τ_1 and τ_2, we applied the values of Fujiwara et al. (2021), i.e., $\tau_1 = 2.1176\,\text{day}$ and $\tau_2 = 287.45\,\text{day}$, because the GNSS-A observation frequency is as low as several times per year per site which is insufficient to determine these parameters. Additionally, we approximated the exponential term in their formulation to a linear component, vt, since an extremely large time constant was found by Fujiwara et al. (2021). It should also be noted that we put $\alpha_1 = 0$ for the TU sites where the observation started in 2013.

7.3 Results

Time series of post- and preseismic seafloor displacements with respect to the Okhotsk plate of NNR-MORVEL56 model (Argus et al., 2011) within a framework of the International Terrestrial Reference Frame 2014 (Altamimi et al., 2016; 2017) are shown in Figures 7-3 and 7-4, respectively. The values of the displacement, without corrections for aftershocks, are available at Zenodo (Watanabe et al., 2021c). To discuss the motion changes over several years, we extracted 3-year cumulative movements from the fitted curves for the periods of Apr. 2011 – Apr. 2014, Apr. 2014 – Apr. 2017, and Apr. 2017 – Apr. 2020 (Table 7-3, Figure 7-1). For the preseismic period, we only consider the average velocity (Table 7-3, Figure 7-1a).

The GNSS-A results at the TU sites independently observed by the TU research group (Kido et al., 2015; Honsho et al., 2019) are simultaneously plotted in Figures 7-3g–k for comparison. Because the absolute positions estimated in the different GNSS-A systems tend to be biased due to the differences in the GNSS's reference or the assumed sound speed model, there are offsets in the results between two observation systems, i.e., JCG and TU. The offsets were estimated and corrected as follows: We first estimated the linear trend of JCG's results

in the period of 2013–2017 as a reference. Offsets were calculated from the average of the residuals of the TU's time series for 2013–2017 relative to the JCG's trend.

The previous study performed by the TU research group (Honsho et al., 2019) showed an average velocity of approximately 10 cm/year toward the trench at G17 in a period between 2012 and 2016 and is consistent with our results of the period after 2014, which we are discussing in this study. However, the results at G17 indicated a lower positioning precision compared to the other sites. There could be several reasons as follows: Firstly, mirror transponders installed at G17 frequently misrecognized their identification numbers for acoustic ranging, which are necessary to distinguish the transponder that responded to the acoustic signal. Secondly, the on-board systems on some vessels were unable to perform acoustic ranging longer than 10 seconds, so the track line had to be shrunken, until restoration in 2019 (Figure 7-5). In practice, lack of acoustic data from the outside of the transponder array significantly degrades the positioning accuracy (Nakamura et al., 2021). These errors have also occurred at G12, but G17 seemed to be affected more significantly. The difference between G12 and G17 might be caused by the transponder arrangement or the complexity in the seawater sound speed structure. Although we cannot quantify the positioning accuracy, the results from late 2016 to 2018 tend to have larger uncertainty than in the other period with wider track line.

7.4 Discussions

Based on the temporal changes of seafloor movement (Figure 7-1), we discuss the expressions of viscoelastic relaxation and afterslip in the northern (off-Kamaishi), central (off-Miyagi/main rupture), and southern (off-Fukushima and off-Choshi) parts of the source region, which are conceptually illustrated in Figure 7-6.

7.4.1 Central part/main rupture (off-Miyagi region)

In previous studies that analyzed the data until 2014 (Watanabe et al., 2014; Sun et al. 2014), landward movements at rates larger than the Pacific plate subduction were detected at the sites located above the main rupture, i.e., KAMS and MYGI (Figure 7-1b). This indicated the dominance of the effects of viscoelastic relaxation in the oceanic asthenosphere beneath the Pacific plate, and the interplate backslip, assuming that the interplate coupling was restored (Figure 7-6b). Crustal deformation in this area was consistent with the quantitative models incorporating the viscoelastic response to the geodetically constrained coseismic input (Sun et al. 2014; Sun and Wang, 2015; Freed et al., 2017; Wang et al., 2018). The large landward movements at these sites continued with a slight decay over the whole period, as

well as at G08, G10, G12, and G14 (Figure 7-1c). The decay of the landward motion can be explained as the time-dependent viscoelastic deformation (Figure 7-6b).

Little temporal change in the present decade was found in the horizontal movement at MYGW near the downdip edge of the main rupture (Figures 7-1b–d). If the interplate coupling in the main rupture had been restored, its landward motion of about 4–5 cm/year should be canceled by a trench-ward motion driven by viscoelastic relaxation in the mantle wedge (e.g., Figure 4a of Hu et al., 2016) or afterslip to maintain balance for almost 10 years. Although the landward motion cannot be clearly detected, it seems to have been slightly restored after 2017. This might indicate a decrease in the dominance of relaxation processes similar to those in the main rupture area (Figure 7-6b).

7.4.2 Northern part (off-Kamaishi region)

At the northern edge of the main rupture, little horizontal displacement was observed at KAMN until 2014 (Figure 7-1b). Because viscoelastic relaxation is mainly driven by the stress induced in the low-viscosity layer beneath the lithosphere, it tends to cause almost the same movements at KAMN and KAMS which are only 30 km apart. To explain the velocity contrast at KAMN and KAMS, some postseismic models require afterslip to reach the trench on the northern side of the main rupture to cause a relative trench-ward motion at KAMN with respect to KAMS (Sun and Wang, 2015; Freed et al., 2017).

After 2014, landward motion significantly accelerated at KAMN and had almost the same velocity at KAMS and MYGI (Table 7-3c and Figure 7-1c). With the preseismic velocities (about 3–4 cm/year at both KAMN and KAMS though with large uncertainty; Table 7-3a and Figure 7-1a) taken into account, the consistency in the movements at KAMN and KAMS after 2014 indicates that the two sites have been similarly influenced by long-term viscoelastic relaxation. Because the spatial pattern of the viscoelastic deformation has not significantly changed in the present decade, the viscoelastic relaxation is expected to have caused almost the same displacements at these sites before 2014. This supports that the afterslip in the off-Kamaishi region actually caused the relative trench-ward motion of 10 cm/year in three-year average at KAMN before 2014 to cancel the landward motion driven by the viscoelastic relaxation and interseismic backslip (Figure 7-6b). Furthermore, the temporal evolution of KAMN's movement (Figure 7-3a) confirms that the afterslip in that region had decayed sufficiently in 3 years. After the decay of the afterslip, the viscoelastic response and interplate coupling became dominant for the crustal deformation around KAMN, similar to the case at neighboring GNSS-A sites (Figures 7-6b).

We then examine how interplate afterslip can reproduce the relative trench-ward (ESE-ward) seafloor movements of 10 cm/year at KAMN with respect to KAMS. We calculated the Green's functions for elastic responses at KAMN and KAMS from rectangular dislocations, specifically, the surface displacements at KAMN and KAMS caused by a dislocation on each 5 km x 5 km subfault placed at intervals of 0.05° in latitude and longitude, in an elastic half-space medium (Okada, 1992). For simplification, strike, dip, and rake angles of the subfaults are fixed to 195°, 13°, and 90°, respectively. The depths of the subfaults are referenced to Nakajima and Hasegawa (2006). Figure 7-7 shows the Green's function of each subfault to the seafloor sites, i.e., movements at KAMN and KAMS. The subfaults located beneath and in the northern side of KAMN significantly contribute to the generation of a relative trench-ward motion at KAMN (green region in Figure 7-7a). Because the surface displacement from a unit slip on a subfault is in the order of 10^{-3} (0.006 at the maximum), roughly 100 subfaults with a slip of 1 m/year can reproduce the relative velocity of 0.1 m/year. This is equivalent to a 50 km x 50 km rectangular fault. There is no resolution for the slip in the white region in Figure 7-7a, which indicates that our data cannot resolve the afterslip in these regions.

According to the estimation above, to reproduce the difference in the average displacement rate of about 10 cm/year between KAMN and KAMS before 2014, afterslip in the northern region outside the coseismic rupture with an average displacement rate on the order of meters per year is required. However, the slip magnitude depends on the afterslip distribution, which cannot be geodetically constrained. Taking into account the tsunami-derived shallow coseismic slip in the off-Kamaishi area, the afterslip would not be expected to have reached the trench at 39 °N (Figure 7-1b).

7.4.3 Southern part (off-Fukushima/Choshi region)

In contrast to the off-Miyagi region, rapid trench-ward movements were observed at FUKU and CHOS in the southern region (< 37.5 °N) especially in the first 1–2 years after the Tohoku-oki earthquake (Figures 7-3e–f). The trench-ward motion became much smaller after 2013. Almost no significant horizontal movement was found at G17, located on the trench side of FUKU, despite the low positioning accuracy due to instrumental malfunction (< 5–6 cm/year for three-year average displacement rate; see Section 7.3 for detail).

For the horizontal movement, it is reasonable to assume that the afterslip caused the trench-ward motion with rapid decay of 1–2 years, as shown in most of the postseismic models (Sun and Wang, 2015; Iinuma et al., 2016; Freed et al., 2017; Agata et al., 2019). Actually, it had been indicated that viscoelastic deformation cannot cause significant motion at FUKU in

some of the finite element models (Sun et al., 2014; Freed et al., 2017), which used the coseismic input based on the geodetic inversion with a single peak beneath FUKU, such as the model by Iinuma et al. (2012) (Figure 7-1b). Therefore, such models require to reproduce both the horizontal and vertical motion at FUKU by only the afterslip, leading to the assumption that strong afterslip in the shallow portion is necessary to explain the rapid subsidence observed at FUKU.

However, the subsidence at FUKU continued at almost a constant rate of about 4 cm/year, even after 2014 when the trench-ward movement had almost ceased. This result conflicts with models which try to explain both the trench-ward motion and the subsidence with shallow afterslip. To show this clearly, we examine the coupling of subsidence and trench-ward (ESE-ward) motion at FUKU caused by interplate afterslip. We calculated the Green's functions for elastic responses at FUKU from rectangular dislocations, specifically, the displacements at FUKU caused by a dislocation on each 5 km x 5 km subfault placed at intervals of 0.05° in latitude and longitude, in an elastic half-space medium (Okada, 1992). For simplification, strike, dip, and rake angles of subfault are fixed to 200°, 13°, and 90°, respectively. The depths of the subfaults are referenced to Nakajima and Hasegawa (2006). Figure 7-8 shows the Green's function of each subfault to the seafloor site, i.e., movements at FUKU. Almost all of the subfaults causing subsidence at FUKU (blue region in Figure 7-8b) simultaneously cause significant trench-ward motion (green region in Figure 7-8a). For this reason, a single afterslip cannot cause such persistent subsidence without significant trench-ward movement at FUKU and G17. Therefore, we should assume another input for the viscoelastic deformation rather than the geodetic inversion model to reproduce the persistent subsidence at FUKU.

Agata et al. (2019) used a coseismic slip model derived from an earthquake cycle simulation (Nakata et al., 2016), which incorporates an additional peak of coseismic rupture near the trench at 37 °N. Although the source model has not reproduced the coseismic seafloor uplift observed at FUKU (Sato et al., 2011), it can provide a practical example for the viscoelastic deformation pattern associated with the shallow coseismic slip. Their viscoelastic finite element model demonstrated sufficient subsidence at FUKU. According to the comparisons of the numerical examples of viscoelastic deformation to the coseismic slip distribution, as illustrated in Figure 6 of Sun and Wang (2015), the hinge line of horizontal deformation and the peak of viscoelastic subsidence were located above the downdip side of the major slip. For this reason, the coseismic slip near the trench caused the subsidence at FUKU in the model of Agata et al. (2019). The tsunami-derived coseismic slip distribution in the off-Fukushima

region (Satake et al., 2013) has two peaks in the along-dip direction (Figure 7-1b). Based on the postseismic model of Agata et al. (2019), the viscoelastic relaxation driven by the shallower coseismic slip can cause long-term subsidence at FUKU (red arrows in Figure 7-6b).

The discussion above suggests that the coseismic models that include constraints from tsunami observations (e.g., Yokota et al., 2011; Minson et al., 2014; Romano et al., 2014; Bletery et al., 2014; Melgar and Bock, 2015) should be adopted in the viscoelastic relaxation model to reasonably explain the spatiotemporal variation of seafloor deformation. In this case, both the viscoelastic relaxation and possible interseismic backslip are predicted to cause landward motion at G17 (red and yellow arrows in Figure 7-6b, respectively). However, it cannot be well detected because of the low accuracy of observations at G17. The data are consistent for both cases where G17 actually moves toward the land and where the landward motion is canceled or weakened by the remaining afterslip. Therefore, the data cannot constrain the degrees of contribution of viscoelastic response and afterslip to the slight trench-ward motion at FUKU in 2014–2017.

In any cases, we can consider that the trench-ward movements at FUKU and CHOS for the first 1–2 years were mainly caused by afterslip in the southern region (purple arrows in Figure 7-6b). Although we cannot constrain and estimate the spatial extent of the southern afterslip region because of the low spatial density of geodetic observation sites at that time, annual-scale afterslip was a dominant deformation source in the southern region except for the vertical component at FUKU. Recalling the tsunami-derived rupture distribution at 37 °N, for reproducing the trench-ward motion at FUKU, it might be reasonable to put the afterslip on the fault between the two peaks of the coseismic slip (Figure 7-1b) rather than putting strong afterslip patches only in far south of FUKU (< 37 °N) as considered in the forward slip model shown by Agata et al. (2019).

7.4.4 Co- and postseismic slip patterns

Considering that afterslip occurs on a fault with aseismic frictional properties, the assumed afterslip regions on the northern and southern sides of the main rupture are considered to have behaved as barriers to the rupture propagation. It is plausible that the shallow tsunamigenic slip in the off-Kamaishi and off-Fukushima areas (Satake et al., 2013) additionally loaded stress on the downdip side, helping to drive the afterslip. The northern afterslip occurred between the rupture zones of major earthquakes, i.e., the 1968 Tokachi-oki earthquake (M_w 8.3), the 1994 offshore Sanriku earthquake (M_w 7.7) (Nagai et al., 2001), the 1896 Meiji Sanriku tsunami earthquake (M_w 8.1) (Satake et al., 2017), and the 2011 Tohoku-

oki earthquake. The gap between the major earthquake ruptures is characterized by relatively low seismicity (Mochizuki et al., 2005), including repeating earthquakes (Uchida and Matsuzawa, 2013; Igarashi, 2020). Slow earthquake activity has been reported in this area (Nishikawa et al., 2019) as well. Although the northern and along-dip extensions of the afterslip zones cannot be resolved due to the absence of geodetic instruments, these features are consistent with the aseismic frictional properties. In the off-Fukushima region, co- and postseismic deformation sequences where the postseismic moment release due to the afterslip exceeded the coseismic moment of the mainshock were observed for the 2008 and 2010 Fukushima-ken-oki earthquakes (M_j 6.9 and M_j 6.7, respectively) (Suito et al., 2011). Although the spatial resolution for these sequences at that time, estimated only with terrestrial GNSS, is insufficient to compare with the afterslip region in the present study, it is possible that the proposed afterslip in the off-Fukushima region following the Tohoku-oki earthquake occurred in a region near the previous afterslip episodes.

The model proposed by Fukuda and Johnson (2021) seems reproduce the spatial distribution of afterslip inferred in the present study (Figure 7-1b). However, there remain deviations in the temporal evolution, especially in the persistent subsidence observed at FUKU. Although it must be difficult to thoroughly reproduce the observations, GNSS-A results suggest that long-term viscoelastic relaxation in the oceanic asthenosphere should have a larger contribution to the movement at FUKU. In addition, because the precisions of preseismic seafloor data are insufficient (as shown in Table 7-3a and Figure 7-1a), effects of the interplate coupling should also be evaluated simultaneously using the postseismic data.

7.5 Conclusions

Based on the GNSS-A observations and the above interpretations, the slip behaviors in the northern and southern areas can be summarized as follows. (1) Afterslip occurred in the northern and southern regions away from the main rupture at depths near the hypocenter, which is consistent with the shallower tsunamigenic slip inducing stress on the downdip aseismic sections of the subduction thrust. It is plausible that these aseismic afterslip regions stopped the north-south rupture propagation (e.g., Nakata et al., 2021). (2) By at least 2014, the afterslip in the off-Kamaishi, off-Fukushima, and off-Choshi regions had almost fully decayed, though there is less evidence for the off-Fukushima region due to the insufficiency of information for determining the viscoelastic deformation patterns. (3) Shallow tsunamigenic slip in the south resulted in subsequent viscoelastic deformation that caused persistent seafloor subsidence, which was captured by postseismic seafloor geodesy. Additionally, the GNSS-A results indicate that the long-term viscoelastic relaxation process is

continuing and is dominant in the off-Miyagi and off-Kamaishi regions. It also plays an important role in the off-Fukushima region, although its contribution cannot be well resolved. These long-term behaviors should be investigated by continuing and expanding seafloor geodetic observations.

Table 7-1. Summary of previously proposed postseismic deformation models (after Watanabe et al., 2021d).

Reference	Rheology model Coseismic input (source)	Afterslip model	Approx. period
Sun et al. (2014)	- Burgers model - Geodetic inversion (Iinuma+ 2012)	Modified from Ozawa et al. (2012) with trial-and-error	3 year
Sun & Wang (2015)	Same model as Sun et al. (2014)	Ad hoc shallow patches added to Sun et al. (2014)	3 year
Wang et al. (2018)	Same model as Sun et al. (2014)	Ad hoc afterslip patches added to Sun & Wang (2015)	5 year
Iinuma et al. (2016)	Same model as Sun et al. (2014)	Geodetic inversion after removing viscoelastic effect	0.7 year
Hu et al. (2016)	- Burgers model - Geodetic inversion (Iinuma+ 2012)	As viscoelastic shear zone with repeating earthquake constraints	2 year
Freed et al. (2017)	- Maxwell model/depth-dependent - Geodetic inversion (self-derived)	Geodetic inversion after removing viscoelastic effect	3 year
Agata et al. (2019)	- Power-law/thermally-activated - Earthquake simulation (Nakata+ 2016)	Forward calculation based on rate- & state-dependent friction	2.8 year
Fukuda & Johnson (2021)	- Burgers model - Geodetic inversion with simultaneous estimation of smoothing parameter	Bayesian inversion for the stress-driven viscoelastic relaxation and afterslip model	7 year

* Models with (1) referencing the seafloor geodetic data, (2) incorporating the afterslip models, (3) modeling the subducting cold slab, and (4) calculating the viscoelastic deformation in an area wider than the latitude range of 37–39 °N, are shown.

Table 7-2. Reference locations of GNSS-A sites (after Watanabe et al., 2021d).

Site	Longitude (°E)	Latitude (°N)
KAMN	143.363	38.886
KAMS	143.263	38.636
MYGI	142.917	38.083
MYGW	142.433	38.150
FUKU	142.083	37.167
CHOS	141.669	35.503
G08	143.643	38.720
G10	143.483	38.300
G12	143.533	38.020
G14	142.775	37.892
G17	142.717	36.900

Table 7-3. Displacements with respect to the Okhotsk plate from the fitted curves with 95% confidence intervals (after Watanabe et al., 2021d).

(a) Average velocity before 2011

Site	Displacement (cm/year)			Variance-covariance ((cm/year)²)			
	E-ward	N-ward	U-ward	V(E,E)	V(E,N)	V(N,N)	V(U,U)
KAMN	-3.5	0.4	0.1	0.40	0.12	0.67	2.61
KAMS	-2.4	-1.8	0.7	2.29	-1.01	1.71	2.10
MYGI	-4.1	2.4	-2.0	0.24	-0.03	0.50	0.93
MYGW	-4.5	1.2	-0.2	0.22	-0.19	0.23	2.06
FUKU	-1.8	-1.3	-2.0	0.30	0.17	1.15	3.15

(b) Three-year cumulative displacement from Apr. 2011 to Apr. 2014.

Site	Displacement (cm)			Variance-covariance (cm²)			
	E-ward	N-ward	U-ward	V(E,E)	V(E,N)	V(N,N)	V(U,U)
KAMN	-4.0	3.6	-21.5	4.76	3.98	-1.45	11.24
KAMS	-32.6	14.9	-16.1	18.22	12.28	-6.08	16.05
MYGI	-28.2	8.4	-21.4	5.35	4.99	0.46	7.34
MYGW	7.8	-14.8	-32.5	2.73	3.11	0.57	7.29
FUKU	60.4	-41.9	-42.1	3.56	5.00	-1.59	8.34
CHOS	59.8	-26.1	5.3	7.60	24.06	3.73	27.44

(**c**) Three-year cumulative displacement from Apr. 2014 to Apr. 2017.

Site	Displacement (cm)			Variance-covariance (cm²)			
	E-ward	N-ward	U-ward	V(E,E)	V(E,N)	V(N,N)	V(U,U)
KAMN	-17.0	4.4	-5.6	0.78	0.65	-0.24	1.84
KAMS	-22.0	6.8	-7.0	2.56	1.73	-0.86	2.26
MYGI	-20.1	7.6	-10.6	1.22	1.14	0.11	1.68
MYGW	-3.3	-2.2	-8.6	0.61	0.70	0.13	1.63
FUKU	5.7	-6.8	-15.5	0.61	0.86	-0.27	1.44
CHOS	1.5	-1.0	0.3	0.61	1.92	0.30	2.19
G08	-25.5	10.5	-3.7	10.39	6.56	-5.44	15.66
G10	-28.0	13.2	-4.9	6.41	19.65	-1.75	17.88
G12	-38.7	17.1	-7.0	10.36	14.54	-2.31	14.64
G14	-21.2	7.4	-12.2	1.58	1.96	-0.94	3.55
G17	6.7	-10.4	-0.5	23.65	9.54	2.44	57.68

(**d**) Three-year cumulative displacement from Apr. 2017 to Apr. 2020.

Site	Displacement (cm)			Variance-covariance (cm²)			
	E-ward	N-ward	U-ward	V(E,E)	V(E,N)	V(N,N)	V(U,U)
KAMN	-20.5	5.3	-3.7	1.61	1.35	-0.49	3.80
KAMS	-22.3	8.1	-6.5	4.78	3.22	-1.59	4.21
MYGI	-20.7	7.4	-8.8	2.49	2.32	0.21	3.42
MYGW	-7.2	-0.4	-6.1	1.24	1.42	0.26	3.32
FUKU	-0.1	-1.1	-12.4	1.20	1.70	-0.54	2.82
CHOS	-2.2	2.0	-2.0	1.00	3.15	0.49	3.60
G08	-18.5	10.8	4.0	15.90	10.03	-8.33	23.96
G10	-26.0	17.5	0.5	13.18	40.40	-3.59	36.77
G12	-28.4	19.3	6.2	19.49	27.35	-4.34	27.54
G14	-18.2	7.7	-6.1	2.45	3.02	-1.46	5.49
G17	-3.6	-4.2	15.4	46.94	18.92	4.84	114.47

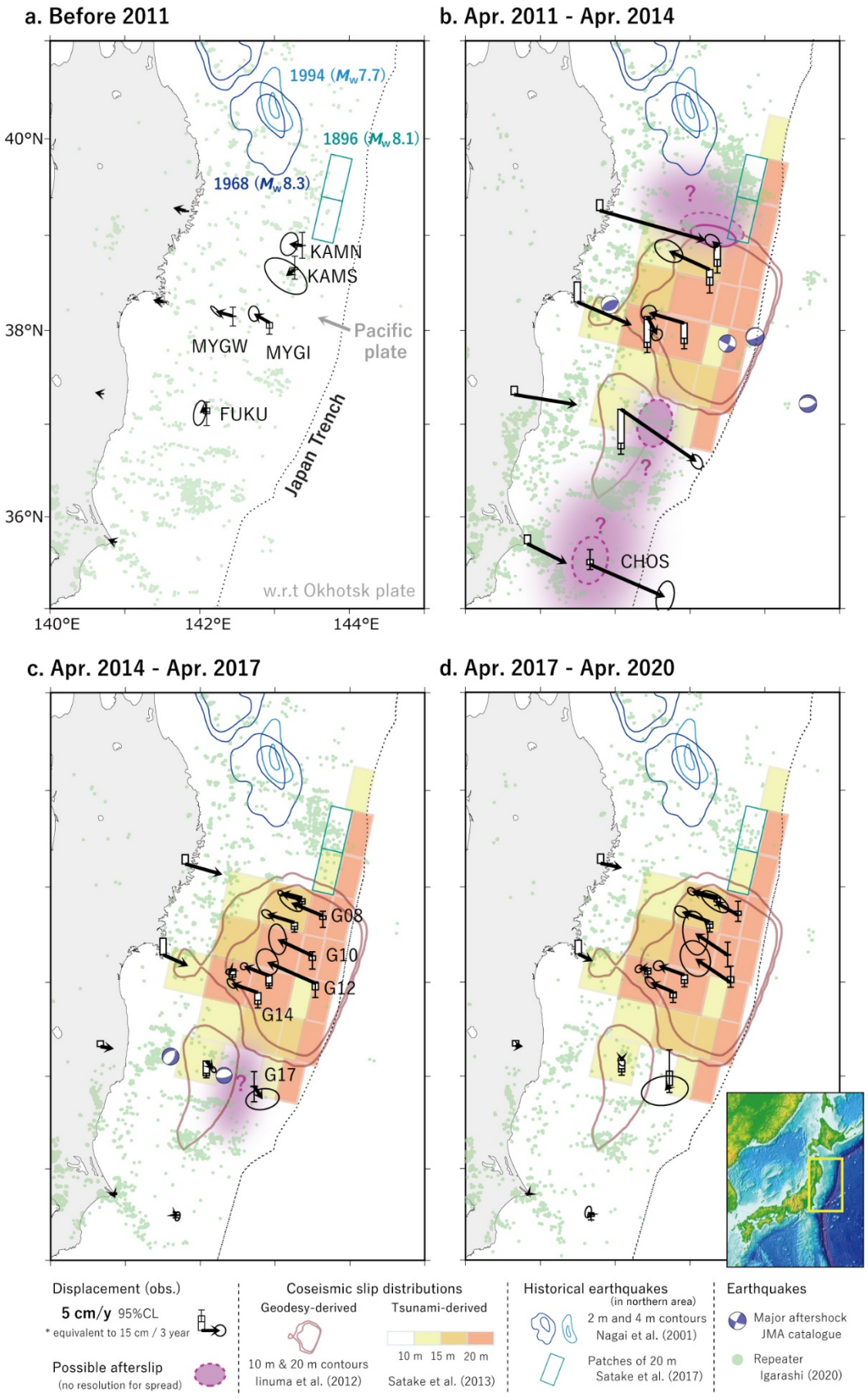
a. Before 2011
b. Apr. 2011 - Apr. 2014
c. Apr. 2014 - Apr. 2017
d. Apr. 2017 - Apr. 2020
1994 (Mw7.7)
1896 (Mw8.1)
1968 (Mw8.3)
KAMN
KAMS
MYGW
MYGI
FUKU
Pacific plate
Japan Trench
w.r.t Okhotsk plate
CHOS
G08
G10
G12
G14
G17
40°N
38°N
36°N
140°E
142°E
144°E
Displacement (obs.)
5 cm/y 95%CL
* equivalent to 15 cm / 3 year
Possible afterslip
(no resolution for spread)
Coseismic slip distributions
Geodesy-derived
10 m & 20 m contours
Iinuma et al. (2012)
Tsunami-derived
10 m 15 m 20 m
Satake et al. (2013)
Historical earthquakes
(in northern area)
2 m and 4 m contours
Nagai et al. (2001)
Patches of 20 m
Satake et al. (2017)
Earthquakes
Major aftershock
JMA catalogue
Repeater
Igarashi (2020)

Figure 7-1. Seafloor motion derived from GNSS-A observations. Average horizontal and vertical velocities for (a) pre-seismic period, and three-year cumulative displacements for (b) 2011–2014, (c) 2014–2017, and (d) 2017–2020 are indicated as black arrows and open rectangles, respectively. Selected terrestrial GNSS velocities or cumulative displacements were extracted from the F3 solution of the GEONET sites (Nakagawa et al., 2009). Onshore velocities during 2007–2011 are shown in (a). Purple patches indicate possible afterslip regions, but there is little or no resolution for their spatial spread. Brown contours and colored tiles indicate geodetically derived (Iinuma et al., 2012) and tsunami-derived (Satake et al., 2013) coseismic slip distributions of the 2011 Tohoku-oki earthquake, respectively. Green circles denote repeating earthquakes that occurred in each period (Igarashi, 2020). CMT solutions for the use of displacement correction are shown in each panel. Navy and blue lines indicate 2-m and 4-m slip contours of historical earthquakes in the northern area (Nagai et al., 2001). Green rectangles indicate patches with a slip of 20 m for the 1896 tsunami earthquake (Satake et al., 2017). The figure is adapted from Watanabe et al. (2021d).

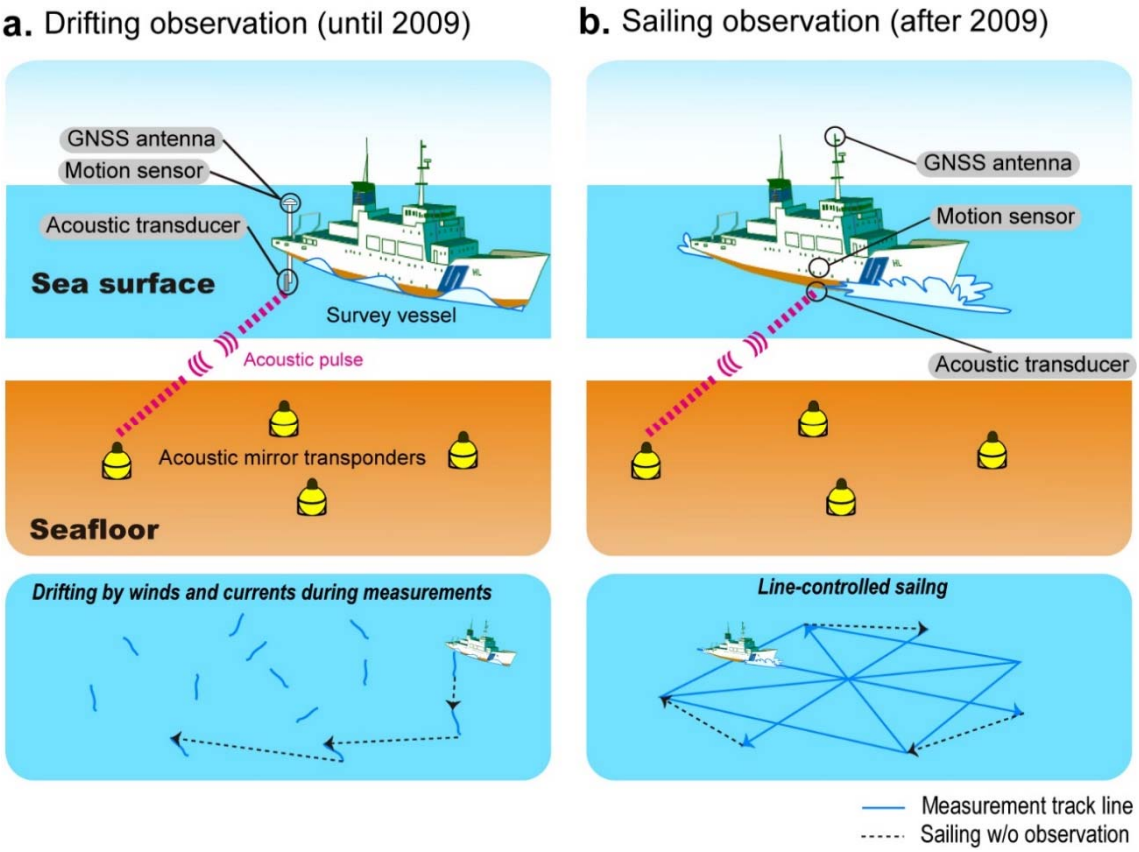

Figure 7-2. Schematic diagrams of the GNSS-A observation. Observation configurations for (a) drifting and (b) sailing systems are shown. The figure is adapted from Watanabe et al. (2021d).

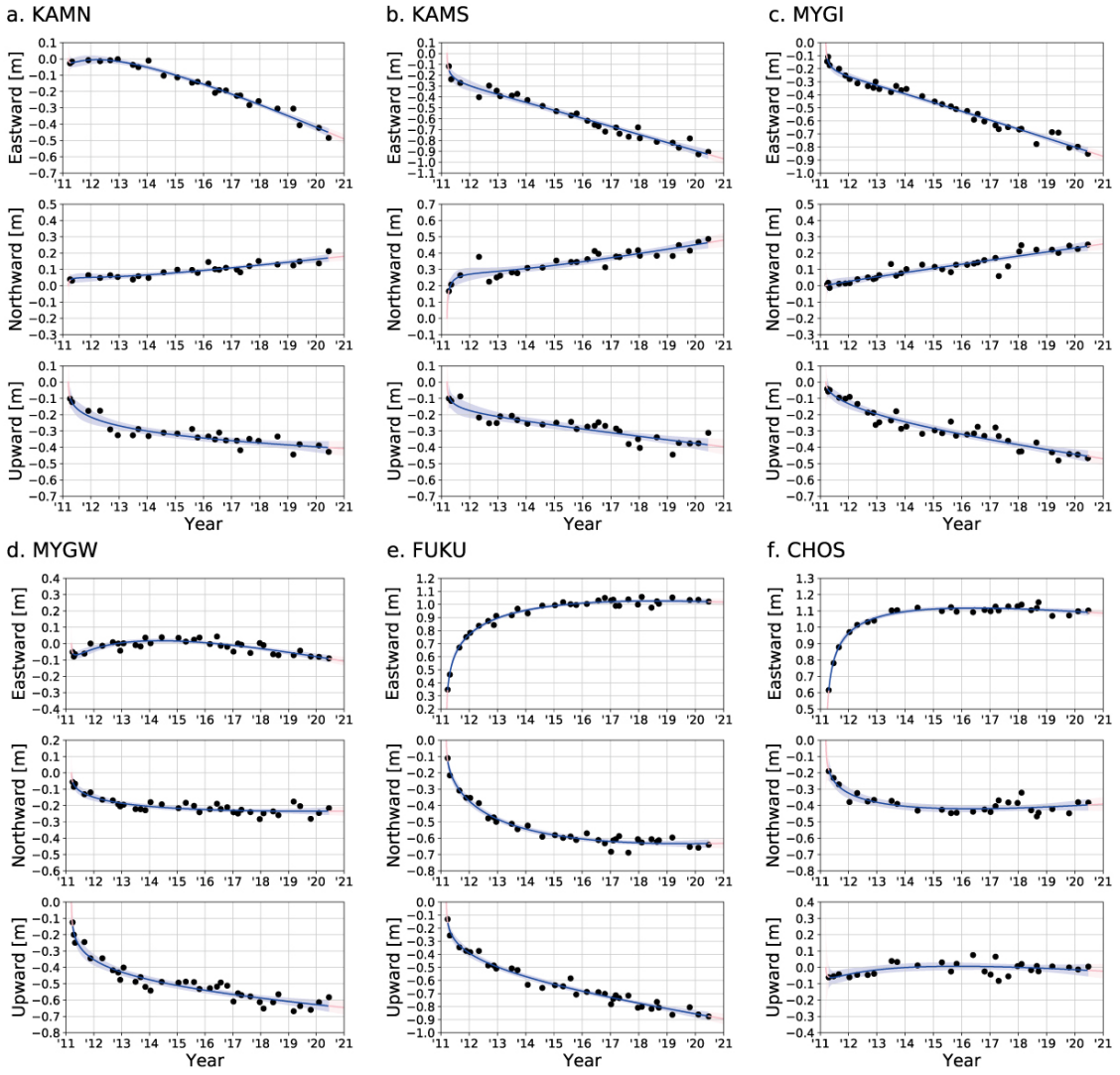

Figure 7-3. Time series of postseismic seafloor displacement. Displacements with respect to the Okhotsk plate of NNR-MORVEL56 model (Argus et al., 2011) are shown (black circles). Fitted logarithmic curves are shown as the solid lines. The 95% confidence intervals for curve fittings are shown as shaded areas. Results provided by Honsho et al. (2019) for (g)–(k) are indicated as brown squares. The figure is adapted from Watanabe et al. (2021d).

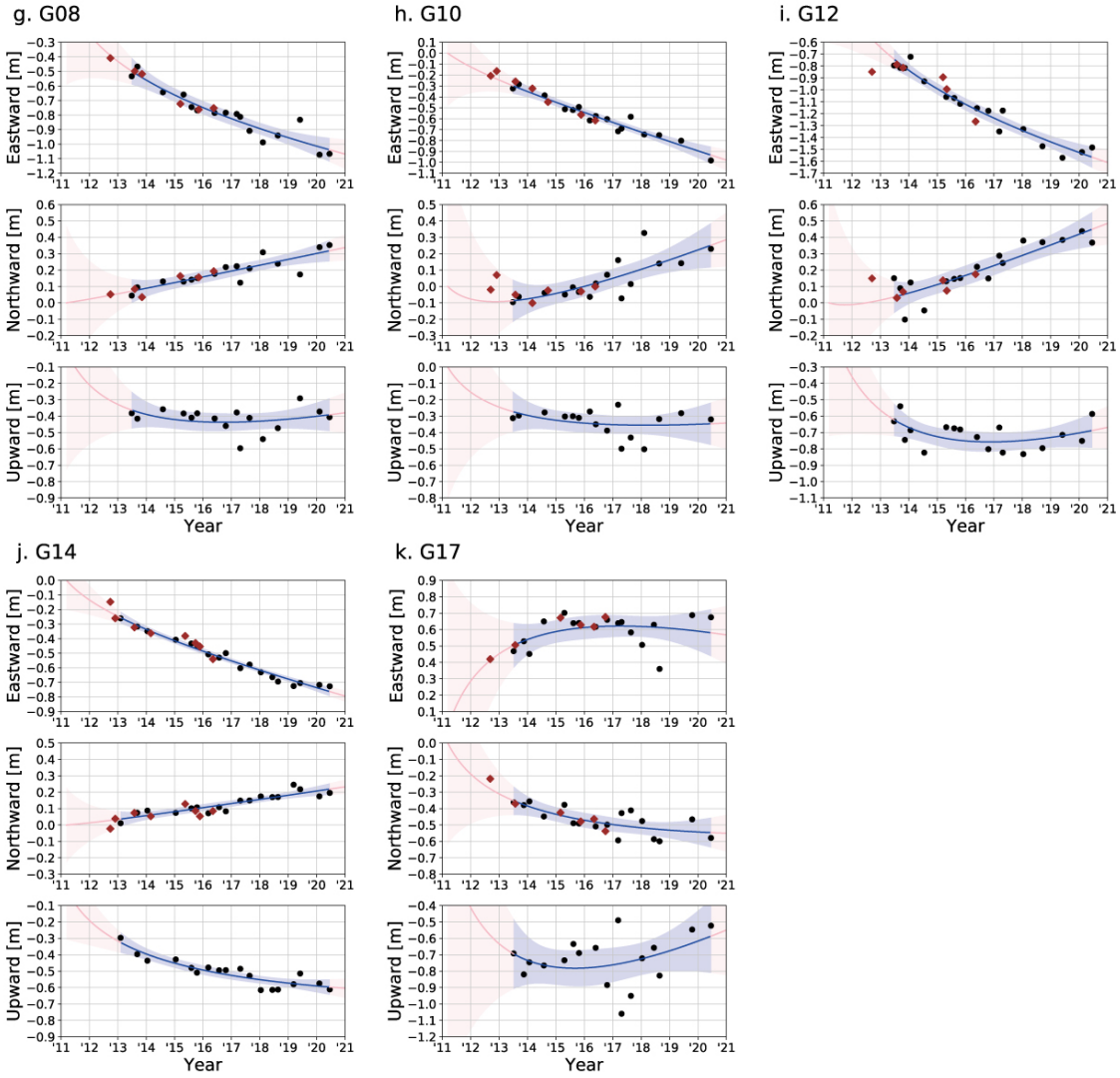

Figure 7-3. Time series of postseismic seafloor displacement (continued).

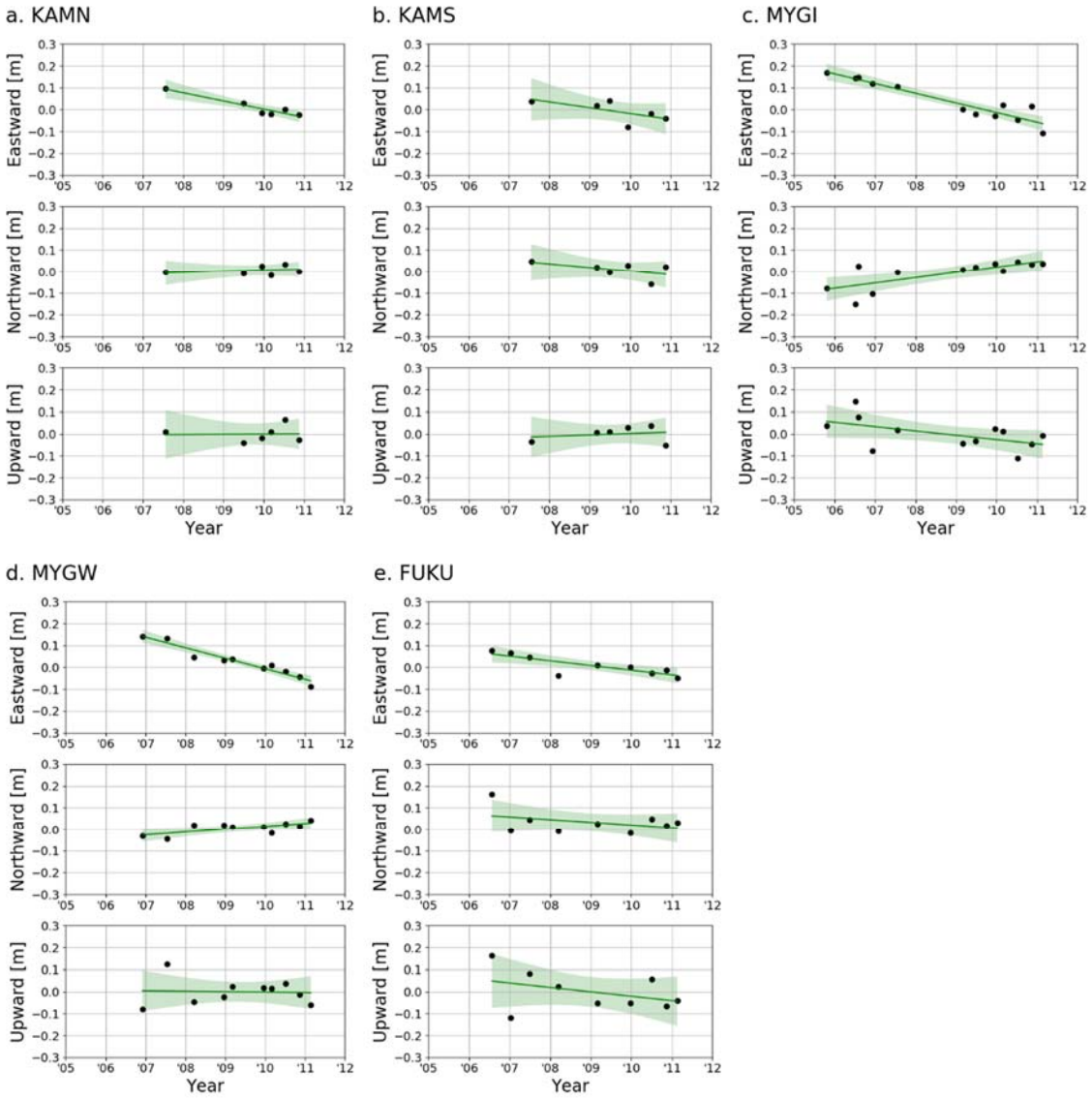

Figure 7-4. Time series of preseismic seafloor displacement. Displacements with respect to the Okhotsk plate of the NNR-MORVEL56 model (Argus et al., 2011) are shown (black circles). Average velocities and their 95% confidence intervals are shown as solid lines and shaded areas, respectively. The figure is adapted from Watanabe et al. (2021d).

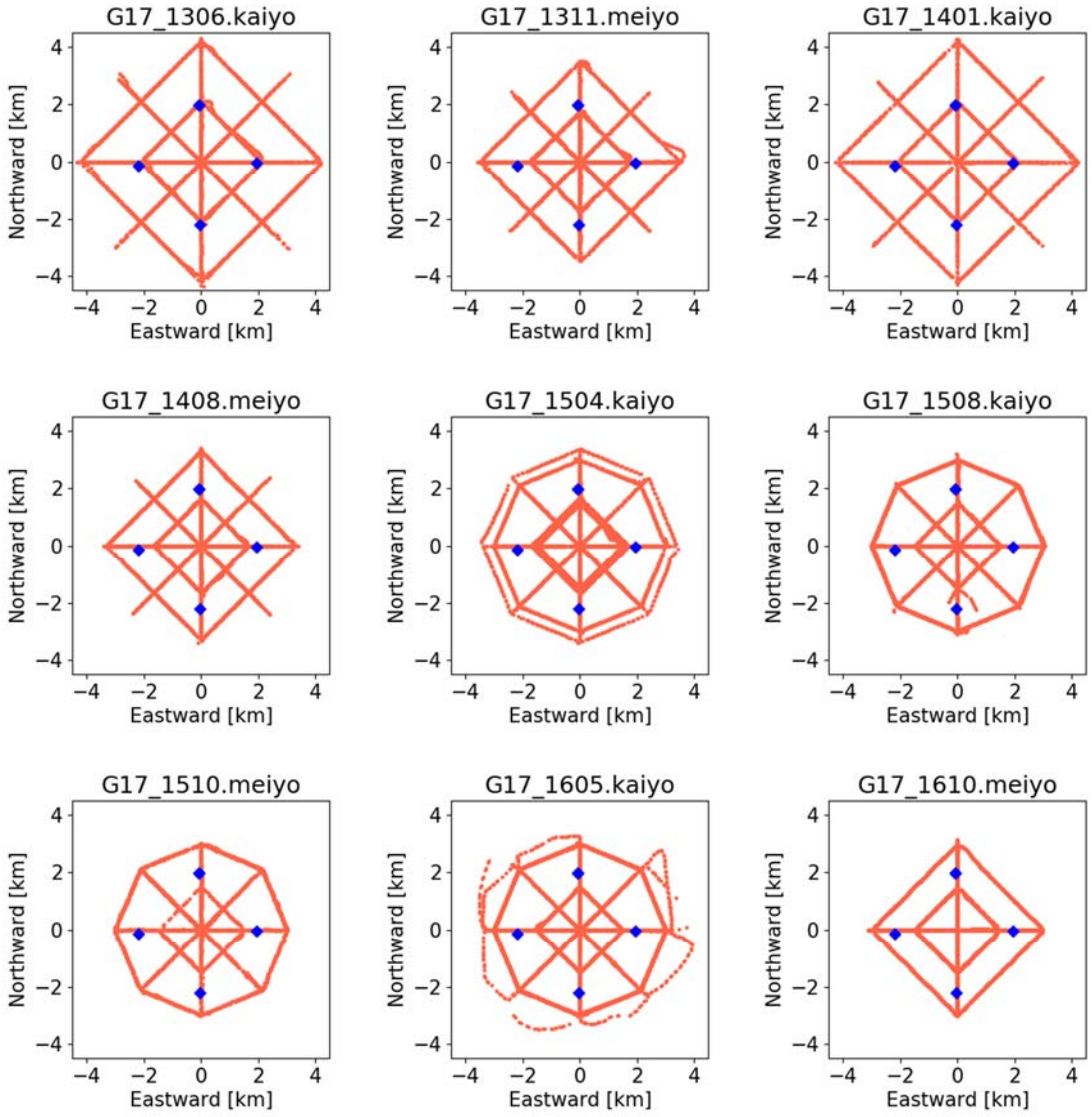

Figure 7-5. Track lines at G17. Orange dots and blue squares indicate the positions of the surface transducer for each acoustic data and the seafloor transponders, respectively. Titles on each panel shows the 4-digit year-month and the name of the used vessel. The figure is adapted from Watanabe et al. (2021d).

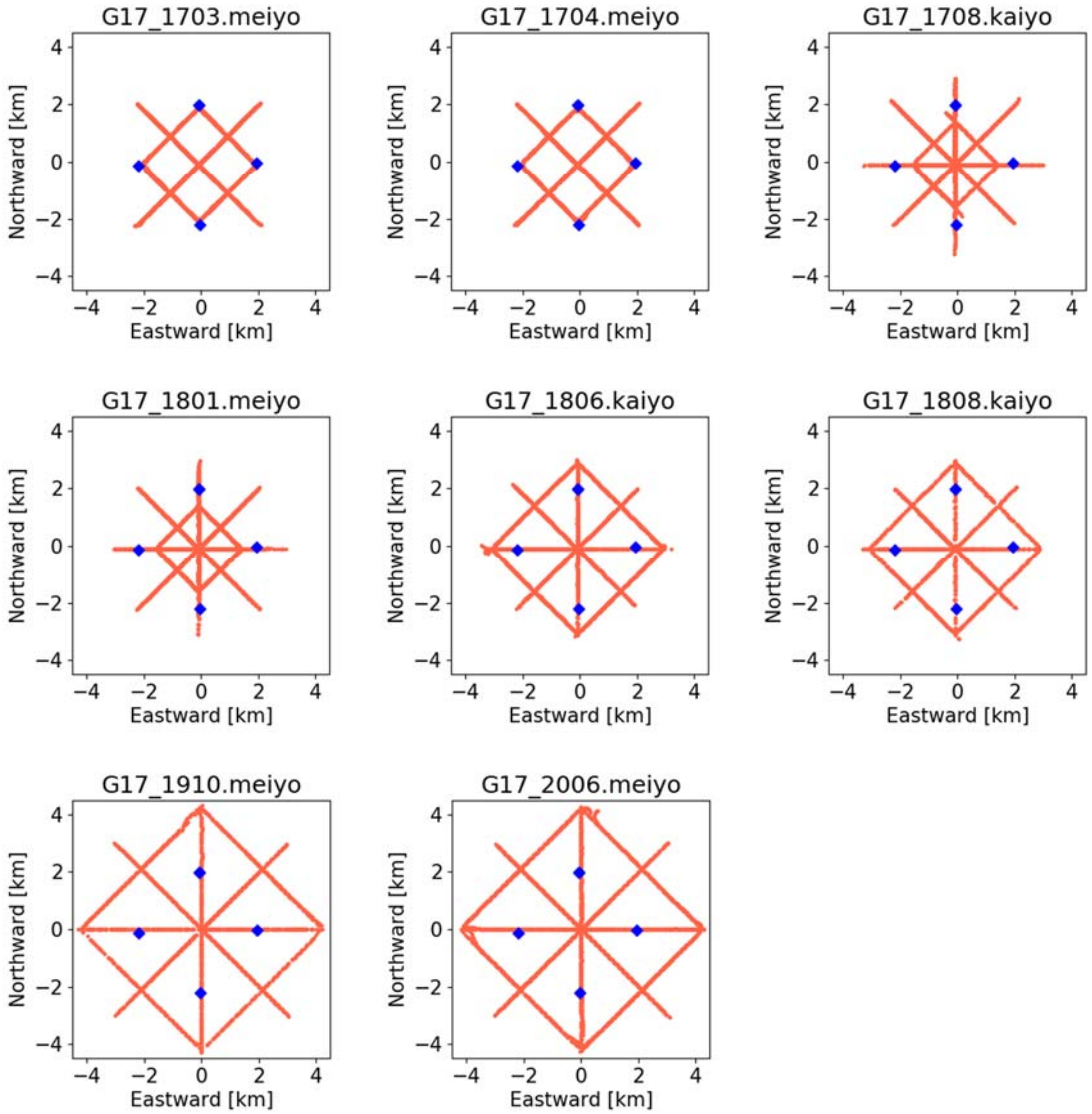

Figure 7-5. Track lines at G17 (continued).

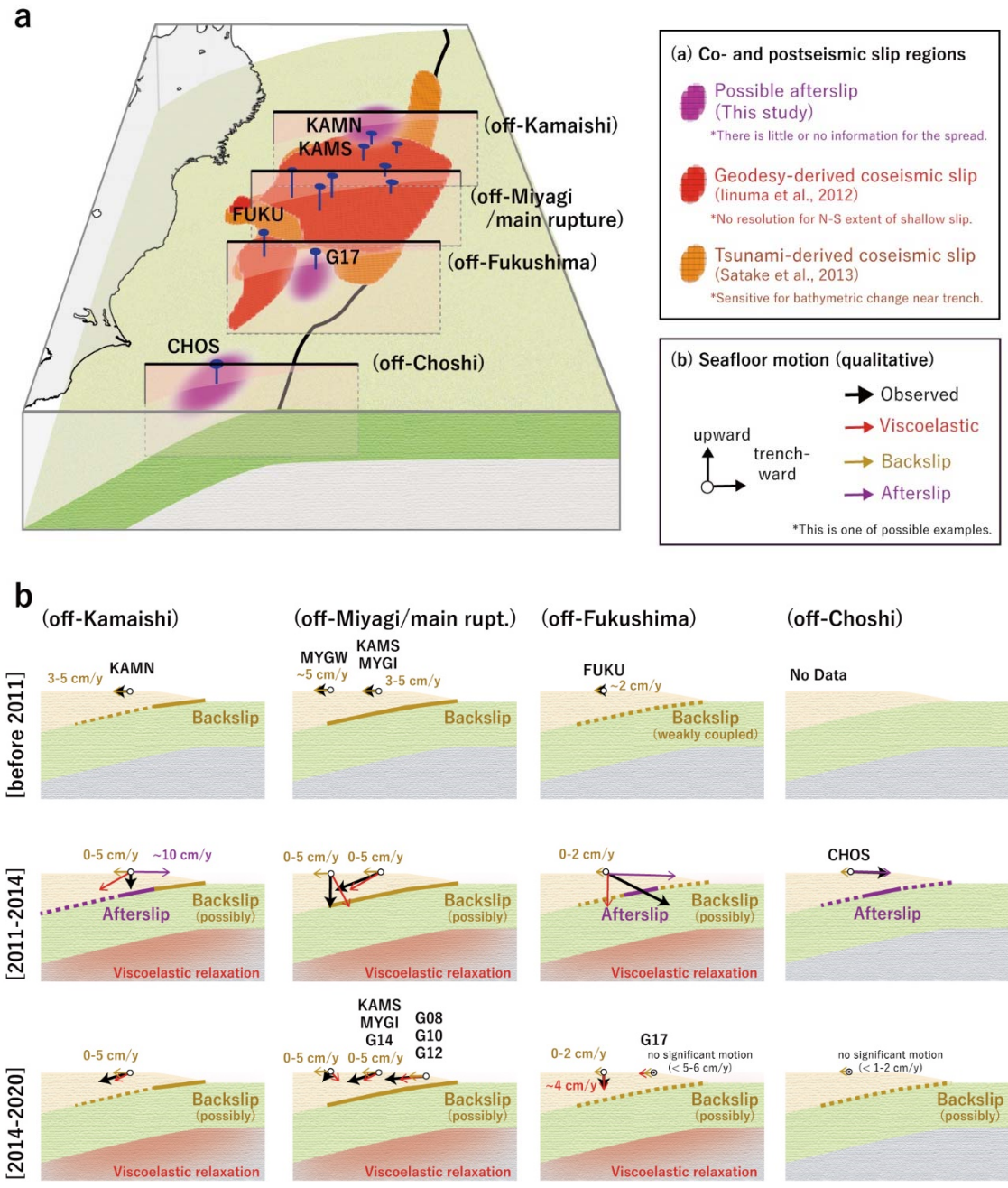
a
KAMN
KAMS
(off-Kamaishi)
FUKU
(off-Miyagi
/main rupture)
G17
(off-Fukushima)
CHOS
(off-Choshi)
(a) Co- and postseismic slip regions
Possible afterslip
(This study)
*There is little or no information for the spread.
Geodesy-derived coseismic slip
(Iinuma et al., 2012)
*No resolution for N-S extent of shallow slip.
Tsunami-derived coseismic slip
(Satake et al., 2013)
*Sensitive for bathymetric change near trench.
(b) Seafloor motion (qualitative)
upward
trench-
ward
Observed
Viscoelastic
Backslip
Afterslip
*This is one of possible examples.
b
(off-Kamaishi)
(off-Miyagi/main rupt.)
(off-Fukushima)
(off-Choshi)
[before 2011]
[2011-2014]
[2014-2020]
3-5 cm/y
KAMN
MYGW
~5 cm/y
KAMS
MYGI
3-5 cm/y
FUKU
~2 cm/y
No Data
Backslip
Backslip
(weakly coupled)
0-5 cm/y
~10 cm/y
0-5 cm/y
0-5 cm/y
0-2 cm/y
CHOS
Afterslip
Backslip
(possibly)
Viscoelastic relaxation
KAMS
MYGI
G14
G08
G10
G12
G17
0-2 cm/y
no significant motion
(< 5-6 cm/y)
~4 cm/y
no significant motion
(< 1-2 cm/y)

Figure 7-6. Schematic diagram of deformation sources beneath the seafloor. (a) Slips on the plate interface. Purple, red, and orange regions indicate possible afterslip region and geodetically derived (Iinuma et al., 2012) and tsunami-derived (Satake et al., 2013) coseismic slip areas of the 2011 Tohoku-oki earthquake, respectively. Blue circles and bars indicate the locations of GNSS-A sites and their projections to the plate interface, respectively. Black rectangles show the locations for cross sections illustrated in subsequent panels. Note that little or no information for the spread of afterslip regions can be added by the present GNSS-A data. (b) Cross sections for each region with one of possible qualitative explanations for the contributions of each deformation source to the motion at GNSS-A sites. Black, red, purple, and yellow arrows indicate the observed motion and components due to viscoelastic relaxation, afterslip, and interplate coupling, respectively. The figure is adapted from Watanabe et al. (2021d).

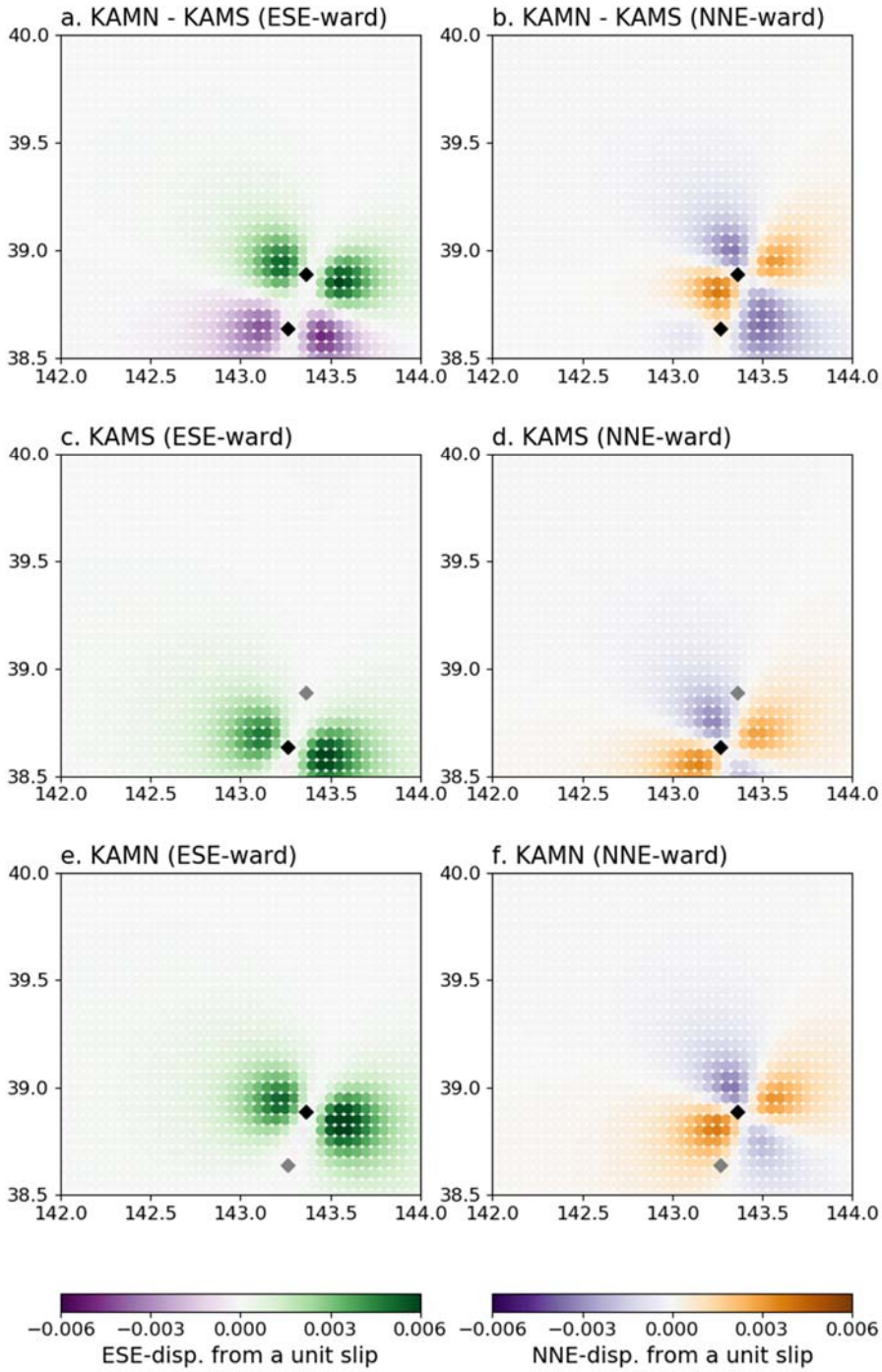

Figure 7-7. Green's functions for elastic responses at (a)–(b) KAMN relative to KAMS, (c)–(d) KAMN, and (e)–(f) KAMS, from each subfault. Strike, dip, and rake angles of the subfaults are fixed to 195°, 13°, and 90°, respectively. Black and gray squares indicate the locations of GNSS-A sites (KAMN and KAMS) used for the calculation and not used for the calculation in each panel, respectively. The figure is adapted from Watanabe et al. (2021d).

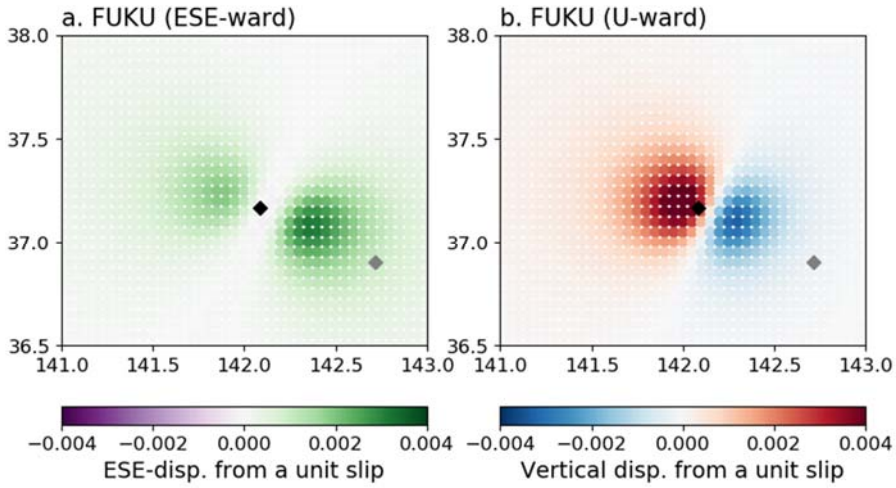

Figure 7-8. Green's functions for elastic responses at FUKU from each subfault. Strike, dip, and rake angles of the subfaults are fixed to 200°, 13°, and 90°, respectively. Black and gray squares indicate the locations of FUKU and G17, respectively. The figure is adapted from Watanabe et al. (2021d).

Chapter 8

Summary and conclusions

Since the very first attempt for realizing the GNSS-A observation concept in 1980s to 1990s, many researchers and engineers had made persistent efforts for the centimeter-scale seafloor positioning. In 2000s, the basics of this technique had established in several research institutes in the United States and Japan. The author reconstructed the GNSS-A methodology including the development of more generalized observation equation, where the sound speed estimation models proposed in earlier studies are incorporated, and the derivation of its solution using the empirical Bayes approach (Chapter 2). The author also applied the method of Precise Point Positioning for the positioning of surface platform (Chapter 3). Based on the derived analytical procedures, an open source analysis software "GARPOS" was developed and published (Chapter 4). This will open the door to the era of "open" GNSS-A, where the researchers, including undergraduate/graduate students, easily join in any type of seafloor geodetic research field such as observational, analytical and applicational researches.

The advantages of "open" GNSS-A analogize with the recent improvement of GNSS technique. The higher availability of data and analysis software for GNSS would be one of the major reasons of the rapid development. Any researchers who are interested in GNSS analysis can be easily obtain the observation data in the world written with the common format, i.e., RINEX, and use the sophisticated standard analysis software such as Bernese, GIPSY, and RTKLIB. Such open data and software help the researchers to stand on the shoulders of giants. Within the open GNSS community, the new applications of GNSS observation have been developed, e.g., the GNSS meteorology, TEC (total electron content) measurements, and GNSS reflectometry.

The newly developed and distributed GNSS-A software "GARPOS" and its standardized I/O format can be the first choice for the researchers interested in seafloor geodesy to join the GNSS-A community. Entry of many researchers definitely promotes the growth of the GNSS-A research field. The proposed sound speed perturbation model is simple but has large

extensivity, such as in case for constructing multiple surface platform GNSS-A. This will lead to further GNSS-A application to the sub-kilometer scale oceanography.

The primary purpose of the GNSS-A seafloor positioning operated by the Japan Coast Guard is geodetic application to the investigations of subduction zone earthquakes. Almost all part of source regions of megathrust earthquakes is located beneath the ocean, where no global geodetic measurement can be performed without GNSS-A technique. Only the global seafloor geodesy can resolve the net convergence rate, coupling ratio, and micro-tectonic features along the trenches and troughs, as discussed in Chapter 5. The GNSS-A site installed on the northernmost part of the Philippine Sea plate between the Sagami Trough and the Izu island arc obviously supported that the forearc moves differently from the central part of the plate. The GNSS-A sites in the Sagami Bay showed the different movement from the Izu microplate and indicated that the block boundary, where an M 6.7 earthquake occurred, is partly coupled.

The accurate determination of interplate coupling in the shallower portion of the seismogenic zone by widely-deployed seafloor GNSS-A observation network enables us to evaluate the risk of seismogenesis and tsunamigenesis. In Chapter 6, the author developed two simplified scenarios by which the importance of plate boundary geometry is highlighted. The results showed that the geometry should be finely resolved to estimate the tsunami initiation as well as coastal subsidence for the assessment of the tsunami hazard. Additionally, the study showed how the postseismic crustal deformation of the relatively large earthquakes would affect the quantitative estimation of the slip deficit on the plate interface. For providing more realistic scenarios, plate coupling model based on the concept of mechanical coupling (e.g., Herman et al., 2018) should be taken into account. In the Nankai Trough, some researchers are investigating to construct the mechanical coupling map (e.g., Noda et al., 2021; Kimura et al., 2020). Furthermore, the GNSS-A observation has an additional advantage in detecting the multi-annual scale variation of seafloor crustal deformation in the global geodetic reference frame compared to the other geophysical instruments deployed on the seafloor (e.g., Yokota and Ishikawa, 2020).

As mentioned above, the GNSS-A also has an advantage to detect long-term (annual scale) transitional crustal deformation, such as the postseismic deformation of huge earthquake, as shown in Chapter 7. With the first 3 years of observation, the author clearly showed the evidence for the dominance of viscoelastic relaxation process in the postseismic deformation in the main rupture zone (Watanabe et al., 2014). The author and colleagues have continued to perform the GNSS-A observations repeatedly for almost 10 years, and detected the

temporal evolution of seafloor movements. These results shed light on not only the spatial distribution of relaxation processes but also the coseismic slip distribution. By considering the temporal evolutions of horizontal and vertical movements region simultaneously, the author pointed out that the coseismic slip had reached near the trench off-Fukushima, which cannot be resolved by coseismic geodetic data. Furthermore, this study also provided valuable information on the decay time of offshore afterslip occurred on the north and south areas of main rupture, and the persistence of viscoelastic effect in the source region.

For the seismogeodetic applications in the future, observation frequency should be improved to provide at least weekly seafloor positions, as discussed by Yokota et al. (2021). To make these realized, unmanned or autonomous surface transponder platform, such as moored buoy (e.g., Imano et al., 2019; Kinugasa et al., 2020; Tadokoro et al., 2020), solar- and wave-powered sailing buoy (e.g., Chadwell, 2016; Iinuma et al., 2021), and unmanned aerial vehicle, should be developed and introduced. Furthermore, the unmanned platform is necessary for the implementation of the real-time GNSS-A observation system, which enables the urgent GNSS-A operation after earthquakes or relevant events. To practically contribute to the governmental decisions for the disaster response to the Nankai Trough earthquakes, one should minimize the latency for the collection and production of the GNSS-A data. In such cases, standardized data format and open source software with generalized sound speed model developed in this study (Chapters 2–4) are expected to work remarkably. Along with the other geophysical instruments, the seafloor geodetic data, whose reliability had been proofed by the recent results (for example, as shown in Chapters 5–7), can detect offshore crustal activities, rupture propagation, stress loading, and early postseismic deformation.

Although almost all current GNSS-A sites are located only in the subduction zone where large earthquakes are expected to occur, the GNSS-A technique has the potential to extend the space geodetic network into the ocean hemisphere. Such the “global geodetic” applications would help the researchers to detect geodetically the present movements of the oceanic plate, whose kinematics derived from geomagnetic surveys might have uncertainty. The “open GNSS-A” strategy will open the door to the “global” geodesy for remaining 70% of our planet.

Acknowledgments

I thank many staff members from the Hydrographic and Oceanographic Department, Japan Coast Guard, including the crew of the survey vessels Takuyo, Shoyo, Meiyo, and Kaiyo for their support in GNSS-A observations and technological developments. I especially thank the active senior staff members from the Geodesy and Geophysics Office, Hydrographic and Oceanographic Department, Japan Coast Guard, for their devoted maintenance and management of the equipment. In the Japan Coast Guard, many staffs allowed and helped the author to perform the research activities during the busy regular works. I appreciate all the experiences during the in situ observation cruises, seminars and meetings with researchers in other institutes, and research visit, which were realized by many efforts of the relevant staffs.

I wish to express special gratitude to

Dr. Masayuki Fujita, Dr. Mariko Sato, Mr. Tadashi Ishikawa, and Mr. Naoto Ujihara of the Japan Coast Guard, for their guidance and coaching as senior colleagues,

Associate Professor Yusuke Yokota of the University of Tokyo, and Mr. Yuto Nakamura, Mr. Toru Uchida, and Mr. Yuhei Akiyama of the Japan Coast Guard, for their continuous support as peer colleagues,

Professor Akira Asada, and Dr. Masashi Mochizuki (now at NIED; the National Research Institute for Earth Science and Disaster Resilience) of the University Tokyo, and Dr. Tetsuichiro Yabuki, Mr. Shin-ichi Toyama, Professor Yoshihiro Matsumoto, and Mr. Hiroaki Saito of the Japan Coast Guard, for their contributions to the launch and development of JCG's GNSS-A,

Dr. Arata Sengoku (now at Aero Asahi Corp.), Dr. Azusa Nishizawa (now at NIED), and Dr. Yukihiro Kato of the Japan Coast Guard, for their support as the supervisors at the JCG,

Dr. Hiromi Fujimoto of NIED, Professor Ryota Hino, Professor Motoyuki Kido, Associate Professor Yusaku Ohta, Assistant Professor Fumiaki Tomita and Assistant Professor Chie Honsho of Tohoku University, Dr. Takeshi Iinuma of the Japan Agency for Marine Earth Science and Technology (JAMSTEC), and Associate Professor Ryoya

Ikuta of Shizuoka University, for the constructive discussion for the improvement of GNSS-A technique and applications,

Dr. Yehuda Bock, Dr. C. David Chadwell, Assistant Professor Diego Melgar (the University of Oregon), Professor Jianghui Geng (Wuhan University), Dr. Peng Fang, Dr. Dara E. Goldberg (now at the U.S. Geological Survey) and other staffs in the Institute of Geophysics and Planetary Physics, for their supports and discussions especially during the author's 1-year visit at the Scripps Institution of Oceanography, University of California, San Diego, under the support of the Ministry of Education, Culture, Sports, Science and Technology in Japan, which led to the studies in Chapters 3 and 6,

Professor Yasuko Takei, and Associate Professor Takehiko Hiraga of Earthquake Research Institute, for their supports and guidance as supervisors for the author's Master's Degree course at the University of Tokyo,

Associate Professor Akito Tsutsumi of Kyoto University, for the guidance and encouragement as a supervisor for the author's Bachelor's Degree program,

Professor Hiroki Kamata, and Professor Katsuya Kaneko (now at Kobe University) of Kyoto University, for their interesting lectures, seminars, and practices for the early stage of the author's Bachelor's Degree program which encouraged the author to choose the division of Earth science,

All the reviewers and editors for the author's peer-reviewed articles, for their valuable comments to improve each manuscript substantially,

and,

Associate Professor Keiichi Tadokoro of Nagoya University, for the support for the submission of this doctoral thesis, and for the constructive discussions for the GNSS-A data, methodology and results, as well as the writing of the manuscript.

Data acquisition and availability

Data acquisition

The ship-borne GNSS data for Chapter 3 were collected by the Hydrographic and Oceanographic Department of Japan Coast Guard during their GPS-A campaign observations.

The GNSS data of the SIO buoy and its PPP solution using GIPSY for Chapter 3 were provided by C. D. Chadwell of the Scripps Institution of Oceanography.

The GNSS-A data at TU sites used in Chapter 7, i.e., G08, G10, G12, G14 and G17, were collected under the collaborative observation with Tohoku University. In-situ observations were performed by the survey vessels operated by the Japan Coast Guard.

Data availability

The GNSS-A data for Chapter 7 is available at Zenodo (Watanabe et al., 2021a; b). The dataset generated in Chapter 7 this study is available at Zenodo (Watanabe et al., 2021c).

The terrestrial GNSS data (1 Hz) and its daily positions for the differential positioning used in this study were provided by the Geospatial Information Authority of Japan.

The 50-450 m bathymetry data and the 30 arcsecond topography data for Chapter 6 are provided by Japan Coast Guard and published as the GEBCO_2014 Grid, version 20150318, available at https://www.gebco.net, respectively.

The CAMP standard geometry data of the Philippine Sea plate for Chapter 6 is provided by C. Hashimoto. The depths of the upper interface of the subducting Philippine Sea plate for Chapter 6 and Pacific plate for Chapter 7 were obtained from the website created by F. Hirose (https://www.mri-jma.go.jp/Dep/sei/fhirose/plate/en.PlateData.html).

The contours for some earthquakes for Chapter 7 were obtained from the website created by N. Uchida (https://www.aob.gp.tohoku.ac.jp/~uchida/page_3_asp-e.html).

The CMT solutions for Chapter 7 provided by the Japan Meteorological Agency are available at https://www.data.jma.go.jp/svd/eqev/data/bulletin/index_e.html.

Software availability

The GNSS-A analysis software "GARPOS v1.0.0" is available at Zenodo (Watanabe et al., 2021e).

The kinematic GNSS software IT (Interferometric Translocation; Colombo, 1998) was provided by O. L. Colombo of the NASA Goddard Space Flight Center.

The open source GNSS analysis software RTKLIB (Takasu, 2013) is developed and distributed by T. Takasu of the Tokyo University of Marine Science and Technology (available at http://www.rtklib.com/).

The GNSS data in Chapter 3 was processed using PANDA (Shi et al., 2008) in modified version at the Scripps Orbit and Permanent Array Center, with the support of D. E. Goldberg.

Software used in Chapter 6, i.e., LaGriT v3.2, Pylith v2.1.4, and GeoClaw v5.3.1, are available via internet at https://lagrit.lanl.gov, https://geodynamics.org/cig/software/pylith, and http://www.clawpack.org, respectively.

Some figures were prepared using Generic Mapping Tools (https://www.generic-mapping-tools.org).

References

Aagaard, B., M. Knepley, and C. Williams (2016) PyLith User Manual, Version 2.1.4., *Comput. Infrastruct. of Geodyn.*, Davis, Calif.

Agata, R., Barbot, S. D., Fujita, K., Hyodo, M., Iinuma, T., Nakata, R., Ichimura, T., and Hori, T. (2019) Rapid mantle flow with power-law creep explains deformation after the 2011 Tohoku mega-quake. *Nat. Commun.*, **10**, 1385. doi:10.1038/s41467-019-08984-7

Akaike, H. (1980) Likelihood and the Bayes procedure. In J. M. Bernardo, et al. (Eds.), *Bayesian Statistics* (pp. 143–166). Valencia, Spain: University Press.

Altamimi, Z., Collilieux, X., Legrand, J., Garay, B., and Boucher, C. (2007) ITRF2005: a new release of the International Terrestrial Reference Frame based on time series of station positions and Earth Orientation Parameters. *J. Geophys. Res.*, **112**, B09401. doi:10.1029/2007JB004949

Altamimi, Z., Métivier, L., Rebischung, P., Rouby, H., and Collilieux, X. (2017) ITRF2014 plate motion model. *Geophys. J. Int.*, **209**, 1906–1912. doi:10.1093/gji/ggx136

Altamimi, Z., Rebischung, P., Métivier, L., and Xavier, C. (2016) ITRF2014: A new release of the International Terrestrial Reference Frame modeling nonlinear station motions. *J. Geophys. Res. Solid Earth*, **121**, 6109–6131. doi:10.1002/2016JB013098

Ando, M. (1975) Source mechanism and tectonic significance of historical earthquakes along the Nankai Trough, Japan. *Tectonophysics*, **27**, 119–140. doi:10.1016/0040-1951(75)90102-X

Araki, E. D., Saffer, M., Kopf, A. J., Wallace, L. M., Kimura, T., Machida, Y., Ide, S., Davis, E., and IODP Exp. 365 shipboard scientists (2017) Recurring and triggered slow-slip events near the trench at the Nankai Trough subduction megathrust, *Science*, **356**, 1157–1160. doi:10.1126/science.aan3120

Argus, D. F., Gordon, R. G., and DeMets, C. (2011) Geologically current motion of 56 plates relative to the no-net-rotation reference frame. *Geochem. Geophys. Geosyst.*, **12**, Q11001. doi:10.1029/2011GC003751

Arisa, D., and Heki, K. (2016) Transient crustal movement in the northern Izu-Bonin arc starting in 2004: A large slow slip event or a slow back-arc rifting event?. *Tectonophysics*, **682**, 206–213. doi:10.1016/j.tecto.2016.05.029

Asada, A., and Yabuki, T. (2001) Centimeter-level positioning on the seafloor. *Proc. Jpn Acad. Ser. B*, **77**, 7–12. doi:10.2183/pjab.77.7

Baba, T., Tanioka, Y., Cummins, P. R., and Uhira, K. (2002) The slip distribution of the 1946 Nankai earthquake estimated from tsunami inversion using a new plate model. *Phys. Earth Planet. Inter.*, **132**, 59–73. doi:10.1016/S0031-9201(02)00044-4

Baba, K., Utada, H., Goto, T., Kasaya, T., Shimizu, H., and Tada, N. (2010) Electrical conductivity imaging of the Philippine Sea upper mantle using seafloor magnetotelluric data. *Phys. Earth Planet. Inter.*, **183**, 44–62. doi:10.1016/j.pepi.2010.09.010

Bai, L., Bergman, E. A., Engdahl, E. R., and Kawasaki, I. (2007) The 2004 earthquakes offshore of the Kii Peninsula, Japan: Hypocentral relocation, source process and tectonic implication. *Phys. Earth Planet. Int.*, **165**, 47–55. doi:10.1016/j.pepi.2007.07.007

Bertiger, W., Desai, S. D., Haines, B., Harvey, N., Moore, A. W., Owen, S., and Weiss, J. P. (2010) Single receiver phase ambiguity resolution with GPS data. *J. Geod.*, **84**, 327–337. doi:10.1007/s00190-010-0371-9

Bletery, Q., Sladen, A., Delouis, B., Vallée, M., Nocquet, J.-M., Rolland, L., and Jiang, J. (2014) A detailed source model for the Mw9.0 Tohoku-Oki earthquake reconciling geodesy, seismology, and tsunami records. *J. Geophys. Res. Solid Earth*, **119**, 7636–7653. doi:10.1002/2014JB011261

Bürgmann, R., and Chadwell, C. D. (2014) Seafloor geodesy. *Ann. Rev. Earth Planet. Sci.*, **42(1)**, 509–534. doi:10.1146/annurev-earth-060313-054953

Chadwell, C. D. (2016) Campaign-style GPS-Acoustic with wave gliders and permanent seafloor benchmarks. In *Proceedings of the Subduction Zone Observatory Workshop*, Boise Center, Boise, ID, Sep. 29 – Oct. 1 2016, Boise, ID.

Chadwell, C. D., and Spiess, F. N. (2008) Plate motion at the ridge-transform boundary of the south Cleft segment of the Juan de Fuca Ridge from GPS-Acoustic data. *J. Geophys. Res.*, **113**, B04415, doi:10.1029/2007JB004936

Chadwell, C. D., and Sweeney, A. D. (2010) Acoustic ray-trace equations for seafloor geodesy. *Marine Geodesy*, **33(2–3)**, 164–186. doi:10.1080/01490419.2010.492283

Chen, H.-Y., Ikuta, R., Lin, C.-H., Hsu, Y.-J., Kohmi, T., Wang, C.-C., Yu1, S.-B., Tu, Y., Tsujii, T., and Ando, M. (2018) Back-arc opening in the western end of the Okinawa Trough revealed from GNSS/Acoustic Measurements. *Geophys. Res. Lett.*, **45**, 137– 145, doi:10.1002/2017GL075724

Colombo, O. L. (1998) Long-distance kinematic GPS. In P. J. G. Teunissen, A. Kleusberg (Eds.), *GPS for Geodesy, 2nd Edition*. Springer, pp 537-567.

Cubas, N., Lapusta, N., Avouac, J.-P., and Perfettini, H. (2015) Numerical modeling of long-term earthquake sequences on the NE Japan megathrust: Comparison with observations and implications for fault friction. *Earth Planet. Sci. Lett.*, **419**, 187–198, doi:10.1016/j.epsl.2015.03.002

Dach, R., Schaer, S., Arnold, D., Prange, L., Sidorov, D., Stebler, P., Villiger, A., and Jäggi A. (2018) CODE final product series for the IGS. *Published by Astronomical Institute, University of Bern*. doi:10.7892/boris.75876.3

Dach, R., Schaer, S., Arnold, D., Prange, L., Sidorov, D., Stebler, P., Villiger, A., and Jäggi A. (2019) CODE rapid product series for the IGS. *Published by Astronomical Institute, University of Bern.* doi:10.7892/boris.75854.3

De Boor, C. (1978) *A Practical Guide to Splines*. Vol. 27, Springer-Verlag New York.

Del Grosso, V. A. (1974) New equation for the speed of sound in natural waters (with comparisons to other equations). *J. Acoust. Soc. Am.*, **56**, 1084-1091. doi:10.1121/1.1903388

DeMets, C., Gordon, R. G., and Argus, D. F. (2010) Geologically current plate motions. *Geophys. J. Int.*, **181**, 1–80. doi:10.1111/j.1365-246X.2009.04491.x

DeMets, C., Gordon, R. G., Argus, D. F., and Stein, S. (1994) Effect of recent revisions to the geomagnetic reversal time scale on estimates of current plate motions. *Geophys. Res. Lett.*, **21**, 2191–2194. doi:10.1029/94GL02118

Freed, A. M., Hashima, A., Becker, T. W., Okaya, D. A., Sato, H., and Hatanaka, Y. (2017) Resolving depth-dependent subduction zone viscosity and afterslip from postseismic

displacements following the 2011 Tohoku-Oki, Japan earthquake. *Earth Planet. Sci. Lett.*, **459**, 279–290. doi:10.1016/j.epsl.2016.11.040

Fujimoto, H. (2014) Seafloor geodetic approaches to subduction thrust earthquakes. *Monogr. Environ. Earth Planets*, **2**, 23 –63, doi:10.5047/meep.2014.00202.0023

Fujita, M. (2006) GPS/Acoustic seafloor geodetic observation —Progress by the Japan Coast Guard (review) — [in Japanese with English abstract], *Rep. Hydro. Ocean. Res.*, **42**, 1–14.

Fujita, M., Ishikawa, T., Mochizuki, M., Sato, M., Toyama, S, Katayama, M., Kawai, K., Matsumoto, Y., Yabuki, T., Asada, A. and Colombo, O. L. (2006) GPS/acoustic seafloor geodetic observation: method of data analysis and its application. *Earth Planets Space*, **58**, 265–275. doi:10.1186/BF03351923

Fujita, M., and Yabuki, T. (2003) A Way of Accuracy Estimation of K-GPS Results in the Seafloor Geodetic Measurement [in Japanese with English figure captions]. *Tech. Bull. on Hydrogr. Oceanogr.*, **21**, 62–66.

Fujiwara, S., Tobita, M., and Ozawa, S. (2021) Spatiotemporal Functional Modeling of Postseismic Deformation After the 2011 Tohoku-Oki Earthquake. *Res. Sq.*, doi:10.21203/rs.3.rs-423959/v1

Fujiwara, T., Kodaira, S., No, T., Kaiho, Y., Takahashi, N., and Kaneda, Y. (2011) The 2011 Tohoku-Oki earthquake: displacement reaching the trench axis. *Science*, **334**, doi:1240. 10.1126/science.1211554

Fukahata, Y. and Wright, T. J. (2008) A non-linear geodetic data inversion using ABIC for slip distribution of a fault with an unknown dip angle. *Geophys. J. Int.*, **173**, 353–364, doi:10.1111/j.1365-246X.2007.03713.x

Fukuda, J., and Johnson, K. M. (2021) Bayesian inversion for a stress-driven model of afterslip and viscoelastic relaxation: Method and application to postseismic deformation following the 2011 MW 9.0 Tohoku-Oki earthquake. *J. Geophys. Res. Solid Earth*, **126**, e2020JB021620. doi:10.1029/2020JB021620

Gagnon, K., Chadwell, C. D., and Norabuena, E. (2005) Measuring the onset of locking in the Peru-Chile trench with GPS and acoustic measurements. *Nature*, **434**(7030), 205–208, doi:10.1038/nature03412

Ge, M., Gendt, G., Rothacher, M., Shi, C., and Liu, J. (2008) Resolution of GPS carrier-phase ambiguities in precise point positioning (PPP) with daily observations. *J. Geod.*, **82**, 389–399. doi:10.1007/s00190-007-0187-4

Geng J., Bock, Y., Melgar, D., Crowell, B. W., and Haase, J. S. (2013) A new seismogeodetic approach applied to GPS and accelerometer observations of the 2012 Brawley seismic swarm: Implications for earthquake early warning. *Geochem. Geophys. Geosyst.*, **14**, 2124–2142. doi:10.1002/ggge.20144

Geng, J., Teferle, F. N., Meng, X., and Dodson, A. H. (2010) Kinematic precise point positioning at remote marine platforms. *GPS Solut.*, **14**, 343–350. doi:10.1007/s10291-009-0157-9

Geng, J., Teferle, F. N., Shi, C., Meng, X., Dodson, A. H., and Liu, J. (2009) Ambiguity resolution in precise point positioning with hourly data. *GPS Solut.*, **13**, 263–270. doi:10.1007/s10291-009-0119-2

Geographical Survey Institute (2005) Crustal Movements in the Chubu and Kinki Districts [in Japanese with English figure captions]. *Rep. Coord. Com. Earthq. Pred.*, **73**, 426–463.

Guo, F., Zhang, X., Li, X., and Cai, S. (2010) Impact of sampling rate of IGS satellite clock on precise point positioning. *Geo-spat. Inf. Sci.*, **13**, 150–156. doi:10.1007/s11806-010-0226-9

Hashimoto, C., Fukui, K., and Matsu'ura M. (2004) 3-D modelling of plate interfaces and numerical simulation of long-term crustal deformation in and around Japan. *Pure Appl. Geophys.*, **161**, 2053–2068, doi:10.1007/s00024-004-2548-8.

Herman, M. W., Furlong, K. P., and Govers, R. (2018) The accumulation of slip deficit in subduction zones in the absence of mechanical coupling: Implications for the behavior of megathrust earthquakes. *J. Geophys. Res. Solid Earth*, **123**, 8260 – 8278. doi:10.1029/2018JB016336

Hirose, F., Nakajima, J., and Hasegawa. A. (2008) Three-dimensional seismic velocity structure and configuration of the Philippine Sea slab in southwestern Japan estimated by double-difference tomography. *J. Geophys. Res.*, **113**, B09315, doi:10.1029/2007JB005274.

Honsho, C., and Kido, M. (2017) Comprehensive analysis of traveltime data collected through

GPS - acoustic observation of seafloor crustal movements. *J. Geophys. Res. Solid Earth*, **122**, 8583–8599, doi:10.1002/2017JB014733

Honsho, C., Kido, M., Tomita, F., and Uchida, N. (2019) Offshore postseismic deformation of the 2011 Tohoku earthquake revisited: Application of an improved GPS-acoustic positioning method considering horizontal gradient of sound speed structure. *J. Geophys. Res. Solid Earth*, **124**, doi:10.1029/2018JB017135

Hovem, J. M. (2013) Ray Trace Modeling of Underwater Sound Propagation. In M. G. Beghi (Ed.), *Modeling and Measurement Methods for Acoustic Waves and for Acoustic Microdevices*, IntechOpen, doi:10.5772/55935

Hu, Y., Bürgmann, R., Banerjee, P., Feng, L., Hill, E. M., Ito, T., Tabei, T., and Wang, K. (2016) Asthenosphere rheology inferred from observations of the 2012 Indian Ocean earthquake. *Nature*, **538**, 368–372, doi:10.1038/nature19787

IERS Conventions (2010) Gérard Petit and Brian Luzum (Eds.). *IERS Technical Note*, **36**, Frankfurt am Main: Verlag des Bundesamts für Kartographie und Geodäsie, 2010. 179 pp. ISBN 3-89888-989-6

Igarashi, T. (2020) Catalog of small repeating earthquakes for the Japanese Islands. *Earth Planet. Space*, **72**, 73. doi:10.1186/s40623-020-01205-2

Iinuma, T., Hino, R., Kido, M., Inazu, D., Osada, Y., Ito, Y., Ohzono, M., Tsushima, H., Suzuki, S., Fujimoto, H., and Miura, S. (2012) Coseismic slip distribution of the 2011 off the Pacific Coast of Tohoku Earthquake (M9.0) refined by means of seafloor geodetic data. *J. Geophys Res*, **117**, B07409. doi:10.1029/2012JB009186

Iinuma, T., Hino, R., Kido, M., Ohta, Y., and Miura, S. (2015) Interplate coupling in and around the rupture area of the 2011 Tohoku earthquake (M9.0) before Its occurrence based on terrestrial and seafloor geodetic observations. *Int. Assn. Geodesy Symp.*, **143**, doi:10.1007/1345_2015_48

Iinuma, T., Hino, R., Uchida, N., Nakamura, W., Kido, M., Osada, Y., and Miura, S. (2016) Seafloor observations indicate spatial separation of coseismic and postseismic slips in the 2011 Tohoku earthquake. *Nat. Commun.*, **7**, 13506. doi:10.1038/ncomms13506

Iinuma, T., Kido, M., Ohta, Y., Fukuda, T., Tomita, F., and Ueki, I. (2021) GNSS-Acoustic Observations of Seafloor Crustal Deformation Using a Wave Glider. *Front. Earth Sci.*, **9**,

600946. doi:10.3389/feart.2021.600946

Ikuta, R., Tadokoro, K., Ando, M., Okuda, T., Sugimoto, S., Takatani, K., Yada, K., and Besana, G. M. (2008) A new GPS-acoustic method for measuring ocean floor crustal deformation: Application to the Nankai Trough. *J. Geophys. Res.*, **113**, B02401. doi:10.1029/2006JB004875

Imano, M., Kido, M., Honsho, C., Ohta, Y., Takahashi, N., Fukuda, T., Ochi, H., and Hino, R. (2019) Assessment of directional accuracy of GNSS-Acoustic measurement using a slackly moored buoy. *Prog. Earth Planet. Sci.*, **6**, 56. doi:10.1186/s40645-019-0302-1

International GNSS Service (a) GNSS Final Combined Orbit Solution Product, Greenbelt, MD, USA: NASA Crustal Dynamics Data Information System (CDDIS). doi:10.5067/gnss/gnss_igsorb_001

International GNSS Service (b) GNSS Final Combined Satellite and Receiver Clock Solution (30 second) Product, Greenbelt, MD, USA: NASA Crustal Dynamics Data Information System (CDDIS). doi:10.5067/GNSS/gnss_igsclk30_001

Ishikawa, T., Yokota, Y., Watanabe, S., and Nakamura, Y. (2020) History of on-board equipment improvement for GNSS-A observation with focus on observation frequency. *Front. Earth Sci.*, **8**, 150. doi;10.3389/feart.2020.00150

Jensen, F. B., Kuperman, W. A., Porter, M. B., and Schmidt, H. (2011) *Computational Ocean Acoustics*, **97**. New York, NY: Springer New York, ISBN:978-1-4419-8677-1

Kawai, K., Fujita, M., Ishikawa, T., Matsumoto, Y., and Mochizuki, M. (2006) Accuracy evaluation of the long baseline KGPS [in Japanese with English figure captions]. *Tech. Bull. on Hydrogr. Oceanogr.*, **24**, 80–88.

Kawakatsu, H., Kumar, P., Takei, Y., Shinohara, M., Kanazawa, T., Araki, E., and Suyehiro, K. (2009) Seismic evidence for sharp lithosphere-asthenosphere boundaries of oceanic plates. *Science*, **324**, 499–502. doi:10.1126/science.1169499

Kawamura, K., Ogawa, Y., Anma, R., Yokoyama, S., Kawakami, S., Dilek, Y., Moore, G. F., Hirano, S., Yamaguchi, A., Sasaki, T., and YK05-08 Leg 29 and YK06-02 Shipboard Scientific Parties (2009) Structural architecture and active deformation of the Nankai Accretionary Prism, Japan: Submersible survey results from the Tenryu Submarine Canyon. *Geol. Soc. Am. Bull.*, **121**, 1629–1646. doi:10.1130/B26219.1

Kido, M., Fujimoto, H., Hino, R., Ohta, Y., Osada, Y., Iinuma, T., Azuma, R., Wada, I., Miura, S., Suzuki, S., Tomita, F., and Imano, M. (2015) Progress in the project for development of GPS/Acoustic technique over the last 4 years. In M. Hashimoto (ed.) *International Symposium on Geodesy for Earthquake and Natural Hazards (GENAH), (Springer, 2015)*, pp. 3–10. doi:10.1007/1345_2015_127

Kido, M., Fujimoto, H., Miura, S., Osada, Y., Tsuka, K., and Tabei, T. (2006) Seafloor displacement at Kumano-nada caused by the 2004 off Kii Peninsula earthquake, detected through repeated GPS/Acoustic surveys. *Earth Planets Space*, **58**, 911–915. doi:10.1186/BF03351996

Kido, M., Osada, Y., and Fujimoto, H. (2008) Temporal variation of sound speed in ocean: A comparison between GPS/acoustic and in situ measurements. *Earth Planet. Space*, **60(3)**, 229–234, doi:10.1186/BF03352785

Kido, M., Osada, Y., Fujimoto, H., Hino, R., and Ito, Y. (2011) Trench-normal variation in observed seafloor displacements associated with the 2011 Tohoku-Oki earthquake. *Geophys. Res. Lett.*, **38**, L24303. doi:10.1029/2011GL050057

Kimura, H., Tadokoro, K., Ito, T., and Sasajima, R. (2020) Mechanical locking distributions along the Nankai Trough in SW Japan estimated by onshore and seafloor geodetic observation data. *AGU Fall Meeting 2020*.

Kinugasa, N., Tadokoro, K., Kato, T., and Terada, Y. (2020) Estimation of temporal and spatial variation of sound speed in ocean from GNSS-A measurements for observation using moored buoy. *Prog. Earth Planet. Sci.*, **7**, 21. doi:10.1186/s40645-020-00331-5

Lay, T. (2018) A review of the rupture characteristics of the 2011 Tohoku-oki Mw 9.1 earthquake. *Tectonophysics*, **733**, 4–36. doi:10.1016/j.tecto.2017.09.022

LeVeque, R. J. (2002) Finite Volume Methods for Hyperbolic Problems, vol. 31, *Cambridge Univ. Press*, Cambridge, U. K.

Lin, W., Byrne, T. B., Kinoshita, M., McNeill, L. C., Chang, C., Lewis, J. C., Yamamoto, Y., Saffer, D. M. , Moore, J. C., Wu, H.-Y., Tsuji, T., Yamada, Y., Conin, M., Saito, S., Ito, T., Tobin, H. J., Kimura, G., Kanagawa, K., Ashi, J., Underwood, M. B., and Kanamatsu, T. (2016) Distribution of stress state in the Nankai subduction zone, southwest Japan and a comparison with Japan Trench. *Tectonophysics*, **692**, 120–130,

doi:10.1016/j.tecto.2015.05.008

Loveless, J. P., and Meade, B. J. (2010) Geodetic imaging of plate motions, slip rates, and partitioning of deformation in Japan. *J. Geophys. Res.*, **115**, B02410, doi:10.1029/2008JB006248

Matsumoto, Y., Fujita, M., and Ishikawa, T. (2008) Development of multi-epoch method for determining seafloor station position [in Japanese]. *Rep. Hydrogr. Oceanogr. Res.*, **26**, 16–22.

Matsu'ura, M., Noda, A., and Fukahata, Y. (2007) Geodetic data inversion based on Bayesian formulation with direct and indirect prior information, *Geophys. J. Int.*, **171(3)**, 1342–1351. doi:10.1111/j.1365-246X.2007.03578.x

Melgar, D., and Bock, Y. (2013) Near-field tsunami models with rapid earthquake source inversions from land- and ocean-based observations: The potential for forecast and warning. *J. Geophys. Res. Solid Earth*, **118**, 5939–5955, doi:10.1002/2013JB010506

Melgar D., and Bock, Y. (2015) Kinematic earthquake source inversion and tsunami runup prediction with regional geophysical data. *J. Geophys. Res.*, **120**, 3324–3349. doi:10.1002/2014JB011832

Melgar, D., Bock, Y., Sanchez, D., and Crowell, B. W. (2013) On robust and reliable automated baseline corrections for strong motion seismology. *J. Geophys. Res. Solid Earth*, **118**, 1177–1187, doi:10.1002/jgrb.50135

Minson, S. E., Simons, M., Beck, J. L., Ortega, F., Jiang, J., Owen, S. E., Moore, A. W., Inbal, A., and Sladen, A. (2014) Bayesian inversion for finite fault earthquake source models – II: the 2011 great Tohoku-oki, Japan earthquake. *Geophys. J. Int.*, **198**, 922–940. doi:10.1093/gji/ggu170

Miyazawa, Y., Zhang, R., Guo, X., Tamura, H., Ambe, D., Lee, J.-S., Okuno, A., Yoshinari, H., Setou, T., and Komatsu, K. (2009) Water mass variability in the western North Pacific detected in a 15-year eddy resolving ocean reanalysis. *J. Oceanogr.*, **65**, 737–756. doi:10.1007/s10872-009-0063-3

Mochizuki, K., Nakamura, M., Kasahara, J., Hino, R., Nishino, M., Kuwano, A., Nakamura, Y., Yamada, T., Shinohara, M., Sato, T., Moghaddam, P. P., and Kanazawa, T. (2005) Intense PP reflection beneath the aseismic forearc slope of the Japan Trench subduction

zone and its implication of aseismic slip subduction. *J. Geophys. Res.*, **110**, B01302. doi: 10.1029/2003JB002892

Moore, G. F., Bangs, N. L., Taira, A., Kuramoto, S., Pangborn, E., and Tobin, H. J. (2007) Three-dimensional splay fault geometry and implications for tsunami generation. *Science*, **318**, 1128–1131, doi:10.1126/science.1147195

Nagai, R., Kikuchi, M., and Yamanaka, Y. (2001) Comparative study on the source processes of recurrent large earthquakes in Sanriku-oki Region: The 1968 Tokachi-oki earthquake and the 1994 Sanriku-oki earthquake. *Zisin(2)*, **54**, 267–280. doi:10.4294/zisin1948.54.2_267

Nagaya, Y. (1995) Basic study on a sea floor strain measurement using acoustic techniques [in Japanese with English abstracts]. *Rep. Hydro. Res.*, **31**, 67–76.

Nakagawa, H., Toyofuku, T., Kotani, K., Miyahara, B., Iwashita, C., Kawamoto, S., Hatanaka, Y., Munekane, H., Ishimoto, M., Yutsudo, T., Ishikura, N., and Sugawara, Y. (2009) Development and validation of GEONET new analysis strategy (Version 4) (in Japanese). *J. Geographical. Survey. Inst.*, **118**, 1–8.

Nakajima, J., and Hasegawa, A. (2006) Anomalous low-velocity zone and linear alignment of seismicity along it in the subducted Pacific slab beneath Kanto, Japan: Reactivation of subducted fracture zone?. *Geophys. Res. Lett.*, **33**, L16309. doi:10.1029/2006GL026773

Nakajima, J., and Hasegawa, A. (2007) Subduction of the Philippine Sea plate beneath southwestern Japan: Slab geometry and its relationship to arc magmatism. *J. Geophys. Res.*, **112**, B08306, doi:10.1029/2006JB004770

Nakata, R., Hori, T., Hyodo, M., and Ariyoshi, K. (2016) Possible scenarios for occurrence of M ~ 7 interplate earthquakes prior to and following the 2011 Tohoku-Oki earthquake based on numerical simulation. *Sci. Rep.*, **6**, 25704. doi:10.1038/srep25704

Nakata, R., Hori, T., Miura, S., and Hino, R. (2021) Presence of interplate channel layer controls of slip during and after the 2011 Tohoku-Oki earthquake through the frictional characteristics. *Sci. Rep.*, **11**, 6480. doi:10.1038/s41598-021-86020-9

Nakamura, Y., Yokota, Y., Ishikawa, T., and Watanabe, S. (2021) Optimal transponder array and survey line configurations for GNSS-A observation evaluated by numerical simulation. *Front. Earth Sci.*, **9**, 600993. doi:10.3389/feart.2021.600993

Nishikawa, T., Matsuzawa, T., Ohta, K., Uchida, N., Nishimura, T., and Ide, S. (2019) The slow earthquake spectrum in the Japan Trench illuminated by the S-net seafloor observatories. *Science*, **365**, 808–813. doi:10.1126/science.aax5618

Nishimura, T. (2011) Back-arc spreading of the northern Izu-Ogasawara (Bonin) Islands arc clarified by GPS data. *Tectonophysics*, **512**, 60–67. doi:10.1016/j.tecto.2011.09.022

Nishimura, T., Ozawa, S., Murakami, M., Sagiya, T., Tada, T., Kaidzu, M., and Ukawa, M. (2001) Crustal deformation caused by magma migration in the northern Izu Islands, Japan. *Geophys. Res. Lett.*, **28**, 3745–3748. doi:10.1029/2001GL013051

Nishimura, T., Sagiya, T., and Stein, R. S. (2007) Crustal block kinematics and seismic potential of the northernmost Philippine Sea plate and Izu microplate, central Japan, inferred from GPS and leveling data. *J. Geophys. Res.*, **112**, B05414. doi:10.1029/2005JB004102

No, T., Takahashi, N., Miura, S., Yamashita, M., Kido, Y., and Kodaira, S. (2014) Deformation of the Manazuru Knoll in Sagami Bay, central Japan, associated with subduction of the Philippine Sea plate. *Earth Planets Space*, **66**, 109. doi:10.1186/1880-5981-66-109

Nocquet, J. -M., Jarrin, P., Vallée, M., Mothes, P. A., Grandin, R., Rolandone, F., Delouis, B., Yepes, H., Font, Y., Fuentes, D., Régnier, M., Laurendeau, A., Cisneros, D., Hernandez, S., Sladen, A., Singaucho, J. -C., Mora, H., Gomez, J., Montes, L., and Charvis, P. (2016) Supercycle at the Ecuadorian subduction zone revealed after the 2016 Pedernales earthquake. *Nat. Geo.*, **10**, 145–152, doi:10.1038/ngeo2864

Noda, A., Saito, T., Fukuyama, E., and Urata, Y. (2021) Energy-based scenarios for great thrust-type earthquakes in the Nankai trough subduction zone, southwest Japan, using an interseismic slip-deficit model. *J. Geophys. Res. Solid Earth*, **126**, e2020JB020417. doi:10.1029/2020JB020417

Obana, K., Katao, H., and Ando, M. (2000) Seafloor positioning system with GPS-acoustic link for crustal dynamics observation—a preliminary result from experiments in the sea—. *Earth Planets Space*, **52**, 415–423. doi:10.1186/BF03352253

Ochi, T., and Kato, T. (2013) Depth extent of the long-term slow slip event in the Tokai district, central Japan: A new insight. *J. Geophys. Res. Solid Earth*, **118**, 4847–4860,

doi:10.1002/jgrb.50355

Ohta, Y., Sagiya, T., and Kimata, F. (2006) Assessment of long-term stability of the PPP kinematic GPS [in Japanese with English abstract and captions]. *J. Geod. Soc. Japan*, **52**, 309–318, doi:10.11366/sokuchi1954.52.309

Okada, Y. (1992) Internal deformation due to shear and tensile faults in a half-space. *Bull. Seism. Soc. Am.*, **82(2)**, 1018–1040.

Osada, Y., Fujimoto, H., Miura, S., Sweeney, A., Kanazawa, T., Nakao, S., Sakai, S., Hildebrand, J. A., and Chadwell, C. D. (2003) Estimation and correction for the effect of sound velocity variation on GPS/Acoustic seafloor positioning: An experiment off Hawaii Island, *Earth Planets Space*, **55**, e17–e20. doi:10.1186/BF03352464

Ozawa, S. (2014) Shortening of recurrence interval of Boso slow slip events in Japan. *Geophys. Res. Lett.*, **41**, 2762–2768. doi:10.1002/2014GL060072

Ozawa, S., Nishimura, T., Munekane, H., Suito, H., Kobayashi, T., Tobita, M., and Imakiire, T. (2012) Preceding, coseismic, and postseismic slips of the 2011 Tohoku earthquake, Japan. *J. Geophys. Res.*, **117**, B07404. doi:10.1029/2011JB009120

Park, S.-C., and Mori, J. (2005) The 2004 sequence of triggered earthquakes off the Kii peninsula, Japan. *Earth Planets Space*, **57**, 315–320. doi:10.1186/BF03352569

Romano, F., Trasatti, E., Lorito, S., Piromallo, C., Piatanesi, A., Ito, Y., Zhao, D., Hirata, K., Lanucara, P., and Cocco, M. (2014) Structural control on the Tohoku earthquake rupture process investigated by 3D FEM, tsunami and geodetic data. *Sci. Rep.*, **4**, 5631. doi:10.1038/srep05631

Sagiya, T. (1999) Interplate coupling in the Tokai District, Central Japan, deduced from continuous GPS data. *Geophys. Res. Lett.*, **26**, 2315–2318. doi:10.1029/1999GL900511

Sagiya, T., and Thatcher, W. (1999) Coseismic slip resolution along a plate boundary megathrust: The Nankai Trough, southwest Japan, *J. Geophys. Res.*, **104**(B1), 1111–1129. doi:10.1029/98JB02644

Saito, T., Satake, K., and Furumura, T. (2010a) Tsunami waveform inversion including dispersive waves: the 2004 earthquake off Kii Peninsula, Japan. *J. Geophys. Res.*, **115**, B06303. doi:10.1029/2009JB006884

Saito, H., Seki, Y., Umehara, N., Asakura, T., and Sato, M. (2010b) Effectiveness of rapid orbit in KGPS analysis of seafloor geodetic observation [in Japanese with English abstract]. *Rep. Hydro. Ocean. Res.*, **46**, 32–38.

Sakic, P., Ballu, V., Crawford, W. C., and Wöppelmann, G. (2018) Acoustic Ray Tracing Comparisons in the Context of Geodetic Precise off-shore Positioning Experiments. *Marine Geodesy*, **41:4**, 315–330. doi:10.1080/01490419.2018.1438322

Satake, K., Fujii, Y., Harada, T., and Namegaya, Y. (2013) Time and space distribution of coseismic slip of the 2011 Tohoku earthquake as inferred from tsunami waveform data. *Bull. Seismol. Soc. Am.*, **103**, 1473–1492. doi:10.1785/0120120122

Satake, K., Fujii, Y., and Yamaki, S. (2017) Different depths of near-trench slips of the 1896 Sanriku and 2011 Tohoku earthquakes. *Geosci. Lett.*, **4**, 33. doi:10.1186/s40562-017-0099-y

Sato, M., and Fujita, M. (2012) Progress in GPS/acoustic seafloor geodetic observation [in Japanese with English abstract]. *Rep. Hydro. Ocean. Res.*, **48**, 26–40.

Sato, M., Fujita, M., Matsumoto, Y., Ishikawa, T., Saito, H., Mochizuki, M., and Asada, A. (2013a) Interplate coupling off northeastern Japan before the 2011 Tohoku-oki earthquake, inferred from seafloor geodetic data. *J. Geophys. Res. Solid Earth*, **118**, 1–10. doi:10.1002/jgrb.50275

Sato, M., Fujita, M., Matsumoto, Y., Saito, H., Ishikawa, T., and Asakura, T. (2013b) Improvement of GPS/acoustic seafloor positioning precision through controlling the ship's track line. *J. Geod.*, **118**, 1–10. doi:10.1007/s00190-013-0649-9

Sato, M., Ishikawa, T., Ujihara, N., Yoshida, S., Fujita, M., Mochizuki, M., and Asada, A. (2011) Displacement above the hypocenter of the 2011 Tohoku-oki earthquake. *Science*, **332**, 1395. doi:10.1126/science.1207401

Savage, J. C. (1983) A dislocation model of strain accumulation and release at a subduction zone. *J. Geophys. Res.*, **88**, 4984–4996. doi:10.1029/JB088iB06p04984

Seno, T., Stein, S., and Gripp, A. E. (1993) A model for the motion of the Philippine Sea plate consistent with NUVEL-1A and geological data. *J. Geophys. Res.*, **98**, 17941–17948. doi:10.1029/93JB00782

Sella, G. F., Dixon, T. H., and Mao, A. (2002) REVEL: A model for recent plate velocities from space geodesy. *J. Geophys. Res.*, **107**(B4), 2081. doi:10.1029/2000JB000033

Shi, C., Zhao, Q., Geng, J., Lou, Y., Ge, M., and Liu, J. (2008) Recent development of PANDA software in GNSS data processing. in *Proc. soc. photograph. instr. engineers*, **7285**, 72851S. doi:10.1117/12.816261

Sibson, R. H. (1973) Interaction between temperature and pore-fluid pressure during earthquake faulting and a mechanism for partial or total stress relief. *Nature*, **243**, 66–68. doi:10.1038/physci243066a0

Simons, M., Minson, S. E., Sladen, A., Ortega, F., Jiang, J., Owen, S. E., Meng, L., Ampuero, J.-P., Wei, S., Chu, R., Helmberger, D. V., Kanamori, H., Hetland, E., Moore, A. W., and Webb, F. H. (2011) The 2011 magnitude 9.0 Tohoku-Oki earthquake: Mosaicking the megathrust from seconds to centuries. *Science*, **332**, 1421–1425. doi:10.1126/science.1206731

Spiess, F. N. (1980) Acoustic techniques for Marine Geodesy, *Marine Geodesy*, **4:1**, 13-27, doi:10.1080/15210608009379369

Spiess, F. N., Chadwell, C. D., Hildebrand, J. A., Young, L. E., Purcell, G. H. Jr., and Dragert, H. (1998) Precise GPS/acoustic positioning of seafloor reference points for tectonic studies. *Phys. Earth Planet. Inter.*, **108**(2), 101–112, doi:10.1016/S00319201(98)00089-2

Suito, H. (2017) Viscoelastic relaxation caused by the 2004 off the Kii Peninsula earthquake [in Japanese with English abstract and figure captions]. *Zisin*, **70**, 135–145. doi:10.4294/zisin.2016-11

Suito, H., Nishimura, T., Tobita, M., Imakiire, T., and Ozawa, S. (2011) Interplate fault slip along the Japan Trench before the occurrence of the 2011 off the Pacific coast of Tohoku Earthquake as inferred from GPS data. *Earth Planet. Space*, **63**, 615–619. doi:10.5047/eps.2011.06.053

Suito, H., and Ozawa, S. (2009) Transient crustal deformation in the Tokai District - the Tokai slow slip event and postseismic deformation caused by the 2004 off Southeast Kii Peninsula earthquake [in Japanese with English abstract and figure captions]. *Zisin*, **61**, 113–135. doi:10.4294/zisin.61.113

Sun, T., and Wang, K. (2015) Viscoelastic relaxation following subduction earthquakes and its effects on afterslip determination. *J. Geophys. Res.*, **120**, 1329–1344. doi:10.1002/2014JB011707

Sun, T., Wang, K., Fujiwara, T., Kodaira, S., and He, J. (2017) Large fault slip peaking at trench in the 2011 Tohoku-oki earthquake. *Nat. Commun.*, **8**, 14044. doi:10.1038/ncomms14044

Sun, T., Wang, K., Iinuma, T., Hino, R., He, J., Fujimoto, H., Kido, M., Osada, Y., Miura, S., Ohta, Y., and Hu, Y. (2014) Prevalence of viscoelastic relaxation after the 2011 Tohoku-oki earthquake. *Nature*, **514**, 84–87. doi:10.1038/nature13778

Suzuki, K., Nakano, M., Takahashi, N., Hori, T., Kamiya, S., Araki, E., Nakata, R., and Kaneda, Y. (2016) Synchronous changes in the seismicity rate and ocean-bottom hydrostatic pressures along the Nankai trough: A possible slow slip event detected by the Dense Oceanfloor Network system for Earthquakes and Tsunamis (DONET). *Tectonophysics*, **680**, 90–98. doi.org/10.1016/j.tecto.2016.05.012

Tadokoro, K., Ando, M., Ikuta, R., Okuda, T., Besana, G. M., Sugimoto, S., and Kuno, M. (2006) Observation of coseismic seafloor crustal deformation due to M7 class offshore earthquakes. *Geophys. Res. Lett.*, **33**, L23306. doi:10.1029/2006GL026742

Tadokoro, K., Ikuta, R., Watanabe, T., Ando, M., Okuda, T., Nagai, S., Yasuda, K., and Sakata, T. (2012) Interseismic seafloor crustal deformation immediately above the source region of anticipated megathrust earthquake along the Nankai Trough, Japan. *Geophys. Res. Lett.*, **39**, L10306. doi:10.1029/2012GL051696

Tadokoro K, Kinugasa N, Kato T, Terada Y and Matsuhiro K (2020) A marine-buoy-mounted system for continuous and real-time measurement of seafloor crustal deformation. Front. Earth Sci. 8:123. doi: 10.3389/feart.2020.00123

Takasu, T. (2013), RTKLIB Ver. 2.4.2: An Open Source Program Package for GNSS Positioning, http://www.rtklib.com/

Takei, Y., and Holtzman, B. K. (2009) Viscous constitutive relations of solid-liquid composites in terms of grain boundary contiguity: 1. Grain boundary diffusion control model. *J. Geophys. Res.*, **114**, B06205. doi:10.1029/2008JB005850

Takeo, M. (1988) Rupture process of the 1980 Izu-Hanto-Toho-Oki earthquake deduced

from strong motion seismograms. *Bull. Seism. Soc. Am.*, **78**(3), 1074–1091.

Tanioka, Y., and Satake, K. (1996) Fault parameters of the 1896 Sanriku tsunami earthquake estimated from tsunami numerical modeling. *Geophys. Res. Lett.*, **23**, 1549–1552. doi:10.1029/96GL01479

Tarantola, A., and Valette, B. (1982) Generalized nonlinear inverse problems solved using the least squares criterion. *Rev. Geophys.*, **20**(2), 219–232. doi:10.1029/RG020i002p00219

Taylor, B., Klaus, A., Moore, G. F., Murakami, F., and Okamura, Y. (1991) Structural development of the Sumisu Rift, Izu-Bonin Arc. *J. Geophys. Res.*, **96**(B10), 16113–16129. doi:10.1029/91JB01900

Tobita, M. (2016) Combined logarithmic and exponential function model for fitting postseismic GNSS time series after 2011 Tohoku-Oki earthquake. *Earth Planet. Space*, **68**, 41. doi:10.1186/s40623-016-0422-4

Tomita, F., Iinuma, T., Ohta, Y., Hino, R., Kido, M., and Uchida, N. (2020) Improvement on spatial resolution of a coseismic slip distribution using postseismic geodetic data through a viscoelastic inversion. *Earth Planets Space*, **72**, 84. doi:10.1186/s40623-020-01207-0

Tomita, F., Kido, M., Honsho, C., and Matsui, R. (2019). Development of a kinematic GNSS-Acoustic positioning method based on a state-space model. *Earth Planets Space*, **71**, 102. doi:10.1186/s40623-019-1082-y

Tomita, F., Kido, M., Osada, Y., Hino, R., Ohta, Y., and Iinuma, T. (2015) First measurement of the displacement rate of the Pacific Plate near the Japan Trench after the 2011 Tohoku‐Oki earthquake using GPS/acoustic technique. *Geophys. Res. Lett.*, **42**, 8391–8397. doi:10.1002/2015GL065746

Tomita, F., Kido, M., Ohta, Y., Iinuma, T., and Hino, R. (2017) Along-trench variation in seafloor displacements after the 2011 Tohoku earthquake. *Sci. Adv.*, **3**(7), e1700113. doi:10.1126/sciadv.1700113

Uchida, N., and Bürgmann, R. (2021) A decade of lessons learned from the 2011 Tohoku-Oki earthquake. *Rev. Geophys.*, **59**, e2020RG000713. doi:10.1029/2020RG000713

Uchida, N., and Matsuzawa, T. (2013) Pre- and postseismic slow slip surrounding the 2011

Tohoku-oki earthquake rupture. *Earth Planet. Sci. Lett.*, **374**, 81–91. doi:10.1016/j.epsl.2013.05.021

Wang, K., Hu, Y., and He, J. (2012) Deformation cycles of subduction earthquake in a viscoelastic Earth. *Nature*, **484**, 327–332. doi:10.1038/nature11032

Wang, K., Sun, T., Brown, L., Hino, R., Tomita, F., Kido, M., Iinuma, T., Kodaira, S., and Fujiwara, T. (2018) Learning from crustal deformation associated with M9 2011 Tohoku-oki earthquake. *Geosphere*, **14**, 552–571. doi:10.1130/GES01531.1

Wang, K., and Tréhu, A. M. (2016) Some outstanding issues in the study of great megathrust earthquakes - The Cascadia example. *J. Geodyn.*, **98**, 1–18. doi:10.1016/j.jog.2016.03.010.

Watanabe, S. (2021) Decadal progress and results of the GNSS-A seafloor geodetic observation from 2011 to 2020 [in Japanese with English abstract]. *Rep. Hydro. Ocean. Res.*, **59**, 95–114.

Watanabe, S., Bock, Y., Chadwell, C. D., Fang, P., and Geng, J. (2017) Long-term stability of the kinematic precise point positioning for the sea surface observation unit compared with the baseline analysis. *Rep. Hydro. Ocean. Res.*, **54**, 38–73.

Watanabe, S., Bock, Y., Melgar, D., and Tadokoro, K. (2018) Tsunami scenarios based on interseismic models along the Nankai trough, Japan, from seafloor and onshore geodesy. *J. Geophys. Res. Solid Earth*, **123**, 2448–2461. doi:10.1002/2017JB014799

Watanabe, S., Ishikawa, T., Nakamura, Y., and Yokota, Y. (2021a). GNSS-A data obtained at the sites along the Japan Trench before the 2011 Tohoku-oki earthquake (Version 1.0.0). *Zenodo*, doi:10.5281/zenodo.4528990

Watanabe, S., Ishikawa, T., Nakamura, Y., and Yokota, Y. (2021b). GNSS-A data obtained at the sites along the Japan Trench from March 2011 to June 2020 (Version 1.0.0). *Zenodo*, doi:10.5281/zenodo.4529008

Watanabe, S., Ishikawa, T., Nakamura, Y., and Yokota, Y. (2021c). Time series of seafloor displacement at GNSS-A sites along the Japan Trench: from March 2011 to June 2020 and before the 2011 Tohoku-oki earthquake (Version 1.0.0). *Zenodo*, doi:10.5281/zenodo.4628550

Watanabe, S., Ishikawa, T., Nakamura, Y., and Yokota, Y. (2021d) Co- and postseismic slip behaviors extracted from decadal seafloor geodesy after the 2011 Tohoku-oki earthquake. *Earth Planets Space*, **73**, 162. doi:10.1186/s40623-021-01487-0

Watanabe, S., Ishikawa, T., and Yokota, Y. (2015) Non-volcanic crustal movements of the northernmost Philippine Sea plate detected by the GPS-acoustic seafloor positioning. *Earth Planets Space*, **67**, 184. doi:10.1186/s40623-015-0352-6

Watanabe, S., Ishikawa, T., Yokota, Y., and Nakamura, Y. (2020a) GARPOS v0.1.0: Analysis tool for GNSS-Acoustic seafloor positioning (Version 0.1.0). *Zenodo*. doi:10.5281/zenodo.3992688

Watanabe, S., Ishikawa, T., Yokota, Y., and Nakamura, Y. (2020b) GNSS-A data obtained at the sites "TOS2" and "MYGI" in 2011-2019. *Zenodo*. doi:10.5281/zenodo.3993912

Watanabe, S., Ishikawa, T., Yokota, Y., and Nakamura, Y. (2020c) GARPOS: Analysis Software for the GNSS-A seafloor positioning with simultaneous estimation of sound speed structure. *Front. Earth Sci.,* **8**, 597532. doi:10.3389/feart.2020.597532

Watanabe, S., Ishikawa, T., Yokota, Y., and Nakamura, Y. (2021e). GARPOS: Analysis tool for GNSS-Acoustic seafloor positioning (Version 1.0.0). Zenodo. doi:10.5281/zenodo.4522027

Watanabe, S., Yokota, Y., and Ishikawa, T. (2020d) Stability Test to Validate the GNSS-A Seafloor Positioning with Kinematic Precise Point Positioning [in Japanese with English abstract and captions]. *J. Geod. Soc. Japan*, **66**, 1–7, doi:10.11366/sokuchi.66.1

Watanabe, S., Sato, M., Fujita, M., Ishikawa, T., Yokota, Y., Ujihara, N., and Asada, A. (2014) Evidence of viscoelastic deformation following the 2011 Tohoku-oki earthquake revealed from seafloor geodetic observation. *Geophys. Res. Lett.*, **41**, 5789–5796. doi:10.1002/2014GL061134

Watanabe, S., and Uchida, T. (2016) Stable structures of temperature and salinity validated by the repeated measurements in the few-miles square regions off Japan coast in the western Pacific [in Japanese with English abstract]. *Rep. Hydro. Ocean. Res.*, **53**, 57–81.

Yagi, Y. (2004) On the earthquakes that occurred southeast off Kii peninsula on September 5, 2004 [in Japanese]. http://iisee.kenken.go.jp/staff/yagi/eq/Japan20040905/Japan20040905_1-j.html

Yamagiwa, S., Miyazaki, S., Hirahara, K., and Fukahata, Y. (2015) Afterslip and viscoelastic relaxation following the 2011 Tohoku-oki earthquake (Mw9.0) inferred from inland GPS and seafloor GPS/Acoustic data. *Geophys. Res. Lett.*, **42**, 66–73. doi:10.1002/2014GL061735

Yamanaka, Y. (2004) Reanalysis of the main shock of SE of Kii peninsula earthquake of September 5 [in Japanese]. http://wwweic.eri.u-tokyo.ac.jp/sanchu/SeismoNote/2004/EIC153.html

Yamanaka, Y., and Kikuchi, M. (2004) Asperity map along the subduction zone in northeastern Japan inferred from regional seismic data. *J. Geophys. Res.*, **109**, B07307. doi:10.1029/2003JB002683

Yamauchi, H., and Takei, Y. (2016) Polycrystal anelasticity at near-solidus temperatures. *J. Geophys. Res. Solid Earth*, **121**, 7790–7820. doi:10.1002/2016JB013316

Yasuda, I. (2003) Hydrographic Structure and Variability in the Kuroshio-Oyashio Transition Area. *J. Oceanogr.*, **59**, 389–402, doi:10.1023/A:1025580313836

Yasuda, K., Tadokoro, K., Ikuta, R., Watanabe, T., Nagai, S., Okuda, T., Fujii, C., and Sayanagi, K. (2014) Interplate locking condition derived from seafloor geodetic data at the northernmost part of the Suruga Trough, Japan. *Geophys. Res. Lett.*, **41**, 5806–5812. doi:10.1002/2014GL060945

Yasuda, K., Tadokoro, K., Taniguchi, S., Kimura, H., and Matsuhiro, K. (2017) Interplate locking condition derived from seafloor geodetic observation in the shallowest subduction segment at the Central Nankai Trough, Japan. *Geophys. Res. Lett.*, **44**, 3572–3579, doi;10.1002/2017GL072918

Yokota, Y., Ishikawa, T., Sato, M., Watanabe, S., Saito, H., Ujihara, N., Matsumoto, Y., Toyama, S., Fujita, M., Yabuki, T., Mochizuki, M., and Asada, A. (2015) Heterogeneous interplate coupling along the Nankai Trough, Japan, detected by GPS-acoustic seafloor geodetic observation. *Prog. Earth. Planet. Sci.*, **2**, 10. doi:10.1186/s40645-015-0040-y

Yokota, Y., and Ishikawa, T. (2019) Gradient field of undersea sound speed structure extracted from the GNSS-A oceanography: GNSS-A as a sensor for detecting sound speed gradient. *SN Appl. Sci.*, **1**, 693. doi:10.1007/s42452-019-0699-6

Yokota, Y. and Ishikawa, T. (2020) Shallow slow slip events along the Nankai Trough detected

by GNSS-A, *Sci. Adv.*, **6**(3), eaay5786. doi:10.1126/sciadv.aay5786

Yokota, Y., Ishikawa, T., and Watanabe, S. (2018) Seafloor crustal deformation data along the subduction zones around Japan obtained by GNSS-A observations. *Sci. Data*, **5**, 180182. doi:10.1038/sdata.2018.182

Yokota, Y., Ishikawa, T., and Watanabe, S. (2019) Gradient field of undersea sound speed structure extracted from the GNSS-A oceanography. *Mar. Geophys. Res.*, **40**(4), 493–504. doi:10.1007/s11001-018-9362-7

Yokota, Y., Ishikawa, T., Watanabe, S., and Nakamura, Y. (2021) Crustal deformation detection capability associated with a fault slip on the interplate boundary in the GNSS-A Seafloor Geodetic Observation Array (SGO-A), provided by Japan Coast Guard. *Res. Sq.*, doi:10.21203/rs.3.rs-783404/v1

Yokota, Y., Ishikawa, T., Watanabe, S., Tashiro, T., and Asada, A. (2016) Seafloor geodetic constraints on interplate coupling of the Nankai Trough megathrust zone. *Nature*, **534**, 374–377, doi:10.1038/nature17632

Yokota, Y., Koketsu, K., Fujii, Y., Satake, K., Sakai, S., Shinohara, M., and Kanazawa, T. (2011) Joint inversion of strong motion, teleseismic, geodetic, and tsunami datasets for the rupture process of the 2011 Tohoku earthquake. *Geophys. Res. Lett.*, **38**, L00G21. doi:10.1029/2011GL050098

Zumberge, J. F., Heflin, M. B., Jefferson, D. C., Watkins, M. M., and Webb, F. H. (1997) Precise point positioning for the efficient and robust analysis of GPS data from large networks, *J. Geophys. Res.*, **102**(B3), 5005–5017. doi:10.1029/96JB03860